DEFECTS IN CALCIUM FLUORIDE GENERATED BY 157 NM LASER AND LOW-ENERGY ELECTRONS

By

LOREN PAUL CRAMER

A dissertation submitted in partial fulfillment of
the requirements for the degree of

DOCTOR OF PHILOSOPHY IN MATERIALS SCIENCE

WASHINGTON STATE UNIVERSITY
Materials Science

DECEMBER 2004

To the Faculty of Washington State university:

The members of the Committee appointed to examine the dissertation of Loren Paul Cramer find it satisfactory and recommend that it be accepted.

_____
Chair

_____

_____

_____

ACKNOWLEDGEMENT

I want to thank the Washington State University Surface Dynamics Group for their effort and support in assisting with this research. I also want to thank the Materials Science (staff and faculty), Physics Department (staff and faculty), and the Technical Services personnel for all their help in my endeavors at Washington State University. And I want to make a very special thanks to my family for their support and patience.

DEFECTS IN CALCIUM FLUORIDE GENERATED BY 157 NM LASER

AND LOW-ENERGY ELECTRONS

Abstract

by Loren Paul Cramer, Ph.D.
Washington State University
December 2004

Chair: J. Thomas Dickinson

Single crystal calcium fluoride (CaF_2) is a material currently being used in vacuum ultraviolet optical components. Unfortunately, all metal halides have a tendency to form defects under energetic particle and laser irradiation, and these defects can degrade material properties. Here we examine the consequences of exposing CaF_2 to 157 nm excimer laser radiation and low energy electrons.

Material characterization of CaF_2 is investigated by various approaches including; laser material interactions, electron material interactions, combinations of laser and electron material interactions, chemical etching of laser and electron treated samples, luminescence dependence on surface modifications, and thermal effects. Since CaF_2 is a promising material for a vast array of applications, such as optical components and a dielectric median for semiconductor applications, it was necessary to investigate the defects. Defect formation can degrade the material properties desired in CaF_2 for various applications.

Electrons and 157 nm laser irradiation is shown to generate metallic nanoparticles (calcium colloids), which change the localized electronic structure resulting in a change in absorption. The metallic nanoparticles absorb light in the visible region (~500-600 nm) resulting in a purple coloration in the exposed areas. The metallic nanoparticles

affect the perfect crystal by more than just small particle absorption (Mie); they also induce stress in the nearby lattice, thereby changing the absorption.

Defects will form in materials that are exposed to intense energetic particles and photon irradiation. By understanding the methods that can cause the degradation it may be possible to either manufacture materials that are more resistant or construct devices that will not exceed the damage thresholds which result in metallic nanoparticle formation.

TABLE OF CONTENTS

Laser interactions with embedded Ca metal nanoparticles in single crystal CaF_2

L. P. Cramer, B. Schubert, P. Petite, S. C. Langford, and J. T. Dickinson
Materials Science Program and Physics Department, Washington State University, Pullman, WA 99164-2814

Single crystal calcium fluoride (CaF_2) is an important optical material for use in the vacuum ultra-violet spectrum. However, prolonged exposure to energetic radiation can color the material, initially with F-centers and, ultimately, with Ca metal nanoparticles. We examine the ability of laser conditioning treatments at wavelengths ranging from the near IR to the deep UV to remove these defects. Treatments at 157, 532 and 1064 nm can significantly reduce the visible absorption due to these nanoparticles. In contrast, irradiation at 248 nm has little effect at fluences below the damage threshold for the CaF_2 employed in this work. We present evidence that the effect of laser irradiation on transmission recovery is principally a thermal process with a bleaching time on the order of 50 ns relative to the laser pulse. We attribute the wavelength dependence of the bleaching process to size dependence of Mie absorption of the metallic nanoparticles. The consequences of these observations with regard to laser conditioning processes in bulk optical materials are discussed.

Introduction

Defect production is a major impediment to the reliability of optical materials at high laser intensities—especially at UV wavelengths. These defects may be produced during prolonged service, as in the darkening of fused silica optical components at 248 and 193 nm.[1,2] In other cases, defects may be produced during crystal growth or manufacture, as in the case of large KDP crystals produced by rapid growth for the National Ignition Facility.[3,4] When damage is caused by absorption at defect aggregates, it is possible that thermal or laser conditioning treatments can allow the aggregated material to reform to the crystal lattice and improve the material quality prior to exposure to damaging laser intensities.[3,4] The mechanism driving the optical improvement is uncertain, but might lead to the development of procedures to ensure the serviceability of optical components and material.[5]

Metal aggregate defects are readily produced in a number of materials by energetic radiation. In single-crystal CaF_2 (fluorite), metallic nanoparticles, often called (calcium) colloids in the literature, are readily produced by relatively low energy electrons (2 keV) at modest doses (< 5 mC/cm^2).[6] These nanoparticles form quasi-organized arrays of ~20 nm particles near the surface.[7] The characteristic absorption of these particles near 600 nm can be analyzed in terms of Mie theory to determine the approximate nanoparticle density and size distribution.[8] These nanoparticles serve as well-characterized aggregates for the study of laser conditioning treatments. We have recently completed a study showing that at relatively low fluences (~1 J/cm^2) we are able to generate metallic nanoparticles in CaF_2 via two photon absorption at 157 nm.[9]

Metallic nanoparticles formation induced by thermal annealing of irradiated single crystal alkali halides are a well-known phenomenon. Thermal annealing of irradiated crystals has also been shown to create nanoparticles in CaF_2 crystals.[10] For temperatures below 300 K the nanoparticle (colloid) band does not change with

temperature; however, above 300 K the mean particle radius begins to increase[6] resulting in increased absorption, and above 430 K the absorption due to nanoparticle formation is reduced.[11]

In this work, we present the consequences of exposing electron-irradiated CaF_2 (densely colored) to laser light at four laser wavelengths (1064, 532, 248, and 157 nm) spanning the near infrared to the vacuum ultraviolet, with a view toward reducing the density and size of the nanoparticles produced by electron irradiation. We compare the beaching efficacy of each of these wavelengths and present evidence that the bleaching mechanism is localized heating of the nanoparticles by the incident radiation.

Experiment

Vacuum ultraviolet grade single crystal CaF_2 was obtained from Korth Kristalle GmbH in the form of cylindrical rods, 1 cm in diameter. Two-millimeter thick slices were cleaved in air along the (111) plane. The samples were mounted on a vacuum-compatible, 3-D translation stage and positioned directly in front of an electron gun in vacuum (~$1x10^{-7}$ Pa) for electron irradiation. The electron gun delivered 100 μA of 2 keV electrons on a 3 x 4 mm^2 area. After irradiation, the sample was removed from vacuum and mounted in a Perkin Elmer Lambda 900 spectrophotometer for characterization. Absorption was measured at wavelengths from 200 to 1200 nm.

Experimental setups for monitoring absorption changes due to exposure at 532 nm and 157 nm can be seen in Figs. 1a and 1b, respectfully. In the case of 532 nm, the laser itself (doubled Nd:YAG, provided by a Continuum Surelite II laser with a pulse width of 7 ns) serves as the probe of transmission changes since it is always near the peak of the absorption spectrum (see below); one photodiode measures a signal proportional to the incident intensity, and the second measures a signal proportional to the transmitted

intensity. Radiation at 157 nm (F_2 excimer) was provided by a Lambda Physik LPF202 laser with a pulse width of 20 ns. Figure 1b shows the setup for 157 nm. Because of poor transmission of 157 nm light through air, bleaching at 157 nm was performed in vacuum (< 1 x 10^{-7} Pa). A sealed tube purged with dry N_2 was utilized to transmit the light from the laser to the vacuum chamber.

Using optics similar to Fig. 1b, bleaching in air was attempted at the other wavelengths. For 248 nm light, a Lambda Physik LEXtra 200 laser (KrF) was used with a pulse width of 30 ns. A Continuum Surelite II Nd:YAG laser provided the 1064 and 532 nm (doubled) light with a pulse with of 7 ns. The probe laser was a CW doubled Nd:YAG, providing transmission measurements at 532 nm. Photodiodes and electronics with response times of ~1 ns were used to monitor the change in transmission. A LeCroy LC334AL 500 MHz digital oscilloscope was used to record the results.

Results

Absorption spectra of electron irradiated CaF_2 are shown in Fig. 2 for four electron doses: The most absorbing spectra illustrated was dosed with 72 mC/cm^2, and shows a slight red shift due to particle size growth. Lower exposure shows less absorption for the electron doses of 60, 25, and 6 mC/cm^2. Even the lowest dose shows some change in absorption near 560 nm consistent with colloid growth in CaF_2. The electron-induced absorption consists of a broad metallic nanoparticle band centered near 560 nm, a shoulder due to isolated fluorine vacancies (F-centers) just below 400 nm, and increased absorption into the UV similar to previous experiments on CaF_2 coloration due to electron irradiation.[12,13]

Starting with a sample that has received electron beam exposure (greater than 100 mC/cm^2), we observe significant reduction in the absorption due to nanoparticles (peaking near 560 nm) by exposure to a few pulses of 50 mJ/cm^2 532 nm radiation, as

shown in Fig. 3. Prolonged 532 nm exposure (1000 pulses) at this fluence would reduce the absorption to approximately 95% of the original peak height but would not eliminate the absorption peak entirely.

At higher laser fluences (100 mJ/cm^2), prolonged exposure reduced the nanoparticle absorption to even lower levels (100 pulses again reduced the absorption to approximately 95% of the original peak height). Unfortunately, at 100 mJ/cm^2 or above, the sample surface was roughened significantly. Typical surface damage from exposure to 100 pulses at 100 mJ/cm^2 is illustrated in the SEM image of the edge of the electron-irradiated area (left side of image) in Fig. 4. Both portions of this image were exposed to the 532 nm bleaching laser. The surface pits could not be entirely avoided even with laser fluences as low as 20 mJ/cm^2.

By measuring the transmission of the 532 nm CW beam while the sample was exposed to electron or laser beams we could follow the formation and bleaching process. Figure 5 shows the 532 nm transmission during electron-irradiation and subsequent bleaching at 157 nm (20 Hz, 10 mJ/cm^2). The total electron dose over 10 minutes was 400 mC/cm^2. The plotted quantity is the ratio of the intensity of the transmitted light to incident probe beam (see Fig. 1b). The initial value of 93% is the transmission of the uncolored sample including reflection losses. The apparent failure of the bleaching process to completely restore transmission is in part due to the large size of the probe beam spot. The area of the 532 nm probe beam on the sample (~0.1 cm^2) was significantly larger than the area of the focused 157 nm beam (~0.04 cm^2). Thus the probe sampled a significant area outside the colored region. Nevertheless, the kinetics of the bleaching process is clear. About 10 minutes (12,000 pulses @10 mJ/cm^2) are required to saturate the recovery. Actual measurements of the recovery using absorption spectra taken after removal of a similarly exposed sample, shows a return to ~ 95 % of original transmission.

The bleaching produced by exposure to 157 nm pulses can be readily seen

visually. Optical images of bleached regions produced by a variety of exposures at 157 nm appear in Fig. 6. The two darkened nearly elliptical spots were formed by electron-irradiation and appear purple to the eye. The several lighter areas within the purple spots were regions bleached at 157 nm. As seen, the treatments (typically 1000 pulses at 20 Hz at 100 mJ/cm^2) produce considerably clearer material.

Similar results were obtained at 532 and 1064 nm. In general, bleaching was fastest at 532 nm, with slower bleaching at 1064 and 157 nm. Significantly, prolonged exposure to 248 nm radiation at the highest practical fluences (avoiding optical damage) had no significant effect on the nanoparticle absorption peak. A summary of the changes in absorption at 532 nm of pre-darkened samples by prolonged exposure to the four laser wavelengths are shown in Fig. 7 (the relevant laser parameters are given in the Figure Caption).

Photo-induced bleaching of point defects is often due to the photoelectronic transfer of charge carriers from one defect to another (e.g., attaching or removing an electron). For extended metal nanoparticles, photoelectronic bleaching seems highly unlikely. A thermal process is more reasonable. To provide evidence for such a mechanism we used time resolved luminescence obtained during a single bleaching pulse. Figure 8 shows the resulting VIS-Near IR spectrum detected through a silica fiber immediately after the first pulse of 1064 nm laser (30 mJ/cm^2) on a darkened crystal. The measurements involved gating a CCD detector so that spectra acquisition began a few nanoseconds after the laser pulse and continued for the following 1 μs. The spectrum is uncorrected for the grating response, the CCD sensitivity, and the fiber optics transmission. We then took spectra of a black body source (tungsten filament) and adjusted the filament temperature until the resulting spectrum matched the laser induced spectrum from the darkened sample. An optical pyrometer was used to measure the filament temperature. The dashed curve in Fig. 8 is the spectrum of the filament associated with a filament at 2700 K. The small peak near 600 nm in the laser induced

spectrum is due to a calcium emission line, indicating the presence of a very weak plasma at the sample surface. We conclude that we are generating black body radiation with a laser pulse and the nanoparticles are reaching temperatures of 2700 K.

Figure 9 shows the bleaching (rise in transmission) of electron irradiated CaF_2 with single pulses of 1064 nm for three different fluences. The insert shows the rise time in the transmission signal to be ~25 ns, which is longer than both the laser pulse (7 ns) and detector/electronics time constant (1 ns). With increasing laser fluence, the electron-irradiated material shows a greater change in transmission. Irradiation with 532 nm with lower fluences (about 5 times less than that of 1064 nm) resulted in similar changes in transmission.

Figure 10 shows the relative change in absorption spectrum with a single pulse of 1064 nm laser light. Curve (a) is the electron irradiated sample; Curves (b) through (d) show a single pulse of 1064 nm with fluences of 275, 400 and 550 mJ/cm^2 respectfully; For comparison, curve (e) is the absorption spectrum of the original sample before it was electron irradiated. Higher fluences (than the multiple shot experiment seen in Fig. 3) were used to better illustrate the bleaching event.

Discussion

The electron-induced coloration in Fig. 2 is consistent with the formation of F-centers and subsequent F-center aggregation to form metallic nanoparticles (calcium colloids).[8,12,13] Huisinga et al. analyzed the absorption spectrum of CaF_2 exposed to 180 mC/cm^2 of 2.5 keV electrons and found an average nanoparticle diameter of 22 nm,[8] which is consistent with the distribution of sizes we see with our long electron doses samples.

Nanoparticle formation in CaF_2 has been studied by several groups.[7,13,14] Electron irradiation of CaF_2 produces stable nanoparticles at room temperature.[15] Transmission

electron microscopy (TEM) of the resulting nanoparticles reveals a quasi-organized arrangement in the bulk.[7,16] We have made initial TEM images of electron-irradiated CaF_2 (dose: 100 mC/cm^2) which indicate that there is a distinct lattice in the formed nanoparticles that retains some measure of order with the original calcium fluoride lattice. The irradiated material under TEM exhibits an interference pattern between the metal particle lattice and the surrounding CaF_2 lattice. The size and somewhat regular distributions of the observed nanoparticles are in agreement with those found in literature with an average particle diameter of about 20 nm. The results from the TEM study supports the nanoparticle size discussed here; a detailed study of the changes induced by the additional nanoparticle lattice will be discussed in forthcoming publication.[17]

Time resolution shows that the majority of the bleaching occurs with a few nanoseconds (~50) of the laser pulse. Figure 9 shows the relative change in transmission for 532 nm probe beam with a single pulse of 1064 nm. The bleaching event is relatively hot (~2700 K) and has a short duration as seen by both the change in transmission and the spectrum seen during bleaching (see Fig. 8).

In terms of nanoparticle formation it is significant that the volume per calcium atom/ion in calcium metal and calcium fluoride are fairly well matched—with the calcium metal atoms requiring some 6% more volume. The resulting compressive stress on the nanoparticles is sufficient to modify their optical properties somewhat, but not enough to cause significant departures from a spherical shape. Little, if any, calcium diffusion is expected during nanoparticle formation. The formation of metallic calcium in electron-irradiated CaF_2 is accompanied by the formation of fluorine-rich defects, including H- and I-centers. (The H-center is equivalent to an F_2^- ion occupying a fluorine lattice site, while the I-center is an F_2^- ion at an interstitial site). Some fluorine may occupy interstitial sites as neutral atoms or molecules.[18] In any case, little fluorine is lost from the lattice. Bleaching presumably involves the in-diffusion of interstitial fluorine (H-centers), which can accept electrons, thereby ionizing calcium to Ca^{2+}. The volume

decrease accompanying $Ca^{\circ} \rightarrow Ca^{2+} + 2e^{-}$ provides room for the incoming fluorine. These electrons provide the negative charge to produce F^{-}, reestablishing the fluorite lattice. Thus, bleaching does not require fluorine vacancy formation in electron-irradiated material, as excess fluorine is available for recombination with metallic calcium. The absence of F-center absorption features in bleached, electron-irradiated material suggests that this recombination and accompanying charge exchange dominates over F-center creation.

Three of the tested wavelengths were effective in bleaching the particles (157 nm, 532 nm and 1024 nm), while one, an intermediate wavelength (248 nm), was ineffective. This puzzling behavior is primarily due to an unusual optical property of the alkaline earth metals. Unlike most metals, calcium displays two bulk (and two surface) plasmons.[19,20] Plasmons play an important role in the absorption of metallic nanoparticles. The existence of two plasmons allows for the possibility of two strong absorptions, separated by a wavelength region with little absorption.

The wavelength-dependence of absorption for small particles is readily calculated from the dielectric properties of the calcium/calcium fluoride system. Comparing our absorption spectra with those of Huisinga et al.[8] suggests that the nanoparticle diameter in our work is approximately 22 nm (11 nm radius). For particles much smaller than the laser wavelength, absorption dominates over scattering. This condition is well satisfied by particles with radius a = 10 nm irradiated at wavelengths longer than 100 nm. Thus all the energy lost from the incident beam can be attributed to absorbed (as opposed to scattered) light.[21,22] For a nanoparticle of volume V and complex dielectric constant $\varepsilon = \varepsilon_r + i\varepsilon_i$, embedded in a transparent media of (real) dielectric constant ε_m and exposed to radiation at wavelength λ and fluence (energy per unit area) F, the total energy ΔH absorbed by the nanoparticle is given by:[21]

$$\Delta H = \left(\frac{6\pi V F}{\lambda}\right)\left(\frac{\varepsilon_i \varepsilon_m}{(\varepsilon_r + 2\varepsilon_m)^2 + \varepsilon_i^2}\right) \quad (1)$$

The dielectric properties of calcium metal have been fairly well studied. Unfortunately, these properties are significantly altered by the small size of the nanoparticles,[21] and the presence of significant tensile stresses.[23]

Orera and Alcacá have formulated an estimate of the effect of nanoparticle size and pressure on the dielectric constants of calcium metal in similar nanoparticles in terms of the nearly free electron model. Although the electrons in calcium are strongly affected by factors neglected in the nearly free electron model, the model captures most of the physics responsible for the difference between calcium in nanoparticle particles and in the bulk.[24]

In the nearly free electron description, the dielectric constant of a bulk metal can be expressed as:[24]

$$\varepsilon_r(E) = \varepsilon_0 - \frac{E_p^2}{E^2 + E_0^2} \quad (2)$$

$$\varepsilon_i(E) = \frac{E_p^2 E_0}{E(E^2 + E_0^2)} \quad (3)$$

where E is the photon energy, ε_0 describes the contribution of ion core polarizability to the real part of the dielectric constant, and E_P is the plasmon energy. We note that the use of a free-electron plasmon energy is potentially ambiguous in an anomalous metal like calcium. Calcium has two bulk plasmons. Following Orera, we employ the energy of the low energy plasmon. The constant E_0 describes the effect of the dielectric relaxation time.

The principal effect of confining electrons in the small volume of the nanoparticle

is to increase the relaxation time τ, the time between electron scattering events. In the nearly free electron model, the relaxation time is related to the bulk conductivity and the thermal electron mass. In pure calcium metal at room temperature, the mean relaxation time is $\tau_{bulk} \approx 4.2 \times 10^{-14}$ s. The corresponding energy ($E_0 = \hbar\omega = \hbar/\tau$) is 0.016 eV—significantly smaller than the photon energies employed in this work. However, for sufficiently small particles, collisions with the surface will reduce the relaxation time. The mean time between scattering events at particle surfaces equals the electron (Fermi) velocity divided by the particle radius ($\tau_{surface} = a/v_F$). From Matthiessen's rule, the net scattering frequency is the sum of the bulk and the nanoparticle surface scattering frequencies. For nanoparticles,[24]

$$E_0^{colloid} = E_0^{bulk} + \frac{\hbar v_F}{a} \tag{4}$$

Stress also alters the dielectric properties of the nanoparticles. The volume per calcium atom is the metal is about 6% greater than the volume per calcium ion in calcium fluoride. Thus the calcium nanoparticles experience significant compression stresses, on the order of 800 MPa. Orera and Alcacá estimate that this stress lowers the plasma frequency of the calcium particles by 10%. The change in ε_r and ε_i due to surface scattering and pressure effects can be estimated subtracting the bulk values from Eqs. (2) and (3) with E_0 and E_P for calcium metal from the nanoparticle values formed by using the corrected values of E_0 and E_P in these same equations. In the limit of small (bulk) E_0, the resulting corrections become:

$$\Delta\varepsilon_r = \frac{0.188 * E_P^2}{E^2} \tag{5}$$

$$\Delta\varepsilon_i = \frac{E_P^2}{E^3}\left[-0.188E_0 + 0.812\frac{\hbar v_F}{a}\right] \quad (6)$$

These corrections were added to literature values for the dielectric constants for calcium metal, and the corrected values were employed in Eq. (1) to estimate the energy absorbed per particle as a function of energy and wavelength. Due to the difficulty of finding a reliable set of dielectric constants for calcium over the entire photon energy range employed, we have used values derived from reflection measurements by Nilsson and Forssell at photon energies greater than 3 eV,[20] and values derived from ellipsometric measurements by Mathewson and Meyers at lower photon energies.[25]

The energy absorbed per nanoparticle, per unit volume, per unit fluence, as a function of wavelength for particles of radius a = 10 nm, is plotted as dots and squares in Fig. 11. The absorbed energy shows two peaks, corresponding to the two distinct plasmons in metallic calcium.[20] Both peaks are significantly shifted from the energies observed in bulk calcium due to nanoparticle size and pressure effects. The position of the low energy peak at 540 nm is consistent with the position of the nanoparticle peak in our absorption spectra (Fig. 2), and would account for strong nanoparticle heating at 532 nm. A second, smaller peak appears at 140 nm (beyond the range of our UV-VIS absorption spectrometer), and would account for at least part of the increase in UV absorption in darkened samples. To our knowledge, the association between UV absorption and nanoparticle production in CaF_2 has not been previously made. This absorption would also account for significant nanoparticle heating at 157 nm. The estimates of Fig. 11 suggest that a particle of radius 10 nm ($V = 4.2 \times 10^{-24}$ m^3) exposed to a fluence of 100 J/m^2 would absorb about 6×10^{-15} J at 157 nm, 2×10^{-15} J at 248 nm, 23×10^{-15} J at 532 nm, and 0.25×10^{-15} J at 1064 nm.

Absorption estimates for the visible and near infrared regions are also shown in Fig. 11 for particles with radii of 5 nm and 2 nm. As the particle size decreases, the 540

nm peak broadens while maintaining (approximately) constant area. At wavelengths near 540 nm, the absorbed energy per unit volume is significantly lower for the smaller particles, but there is a range of wavelengths on both sides of the central peak where the smaller particles absorb more energy per unit volume than the larger particles. For instance, the estimated absorption per unit volume at 1064 nm increases 80% as the particle size decreases from 10 nm to 2 nm. As discussed below, this increase is a potential problem during laser conditioning operations.

The absorption predicted by Mie theory is sufficient to produce significant heating. Assuming that the nanoparticles are spherical and heated uniformly throughout their volume, and that the thermal behavior can be approximated by room temperature values appropriate to CaF_2, the temperature change at the surface of the nanoparticle is given by:[26]

$$\Delta T = \frac{\alpha A \Delta t}{kV}\left[2erfc(0) + 2erfc\left(\frac{a}{\sqrt{\alpha \Delta t}}\right) - \frac{4\sqrt{\alpha \Delta t}}{a} i^3 erfc(0) + \frac{4\sqrt{\alpha \Delta t}}{a} i^3 erfc\left(\frac{a}{\sqrt{\alpha \Delta t}}\right)\right] \quad (7)$$

where A is the power (energy per unit time—assumed to be constant during a laser pulse of duration Δt) delivered to a particle of radius a = 10 nm and volume V. The quantity ($A \Delta t / V$) corresponds to the product of the laser fluence and the absorbed energy per unit volume per unit fluence from Fig. 11. The *erfc* is the complementary error function, and the $i^3 erfc$ is the result of three successive integrations of the *erfc*. The $i^3 erfc$ function is defined and tabulated in Carslaw and Jaeger.[27] The room temperature thermal diffusivity and conductivity of CaF_2 are $\alpha = 3.6 \times 10^{-6}$ m^2/s and $k = 9.7$ W m^{-1} K^{-1}, respectively. On the time scale of the laser pulses used in this work, the scale length for heating ($d = (\alpha \Delta t)^{1/2}$) ranges from 180 to 330 nm—an order of magnitude larger than the particle radius. Thus the assumption that the contrasting thermal properties of the nanoparticle can be

neglected is largely justified.

Applying these constants to a single embedded nanoparticle, the peak nanoparticle temperature change for the Nd:YAG laser for 50 J/m^2, 7 ns pulses that we calculate is 3200 K at 532 nm. Similarly, the temperature change for 100 J/m^2, 20 ns excimer pulses would be about 1600 K at 157 nm and 450 K at 248 nm. The temperatures at 532 and 157 nm are high enough to support a thermal mechanism for nanoparticle removal; the temperature change at 248 nm is sufficiently low that annealing with nanosecond pulses at this wavelength does not occur. Orera et al. report a temperature of 430 K for the destruction for the nanoparticles[24] with prolonged exposure to a 150 W Xe lamp, which is a similar temperature to the calculated 248 nm temperature; however, the transient nature of the 30 ns excimer laser pulse may by why we do not see annealing.

The estimates of Fig. 11 are not reliable at infrared wavelengths (due to the range of the constants used).[20,25] The emission spectrum of Fig. 8 acquired at 1064 nm is the best evidence we can present that thermal annealing is possible at this wavelength. The spectrum corresponds to blackbody radiation at an effective temperature of about 2700 K. Infrared absorption measurements in metallic calcium at this wavelength correspond to an absorption depth of about 15 nm.[28,29] Neglecting thermal conduction, exposing a 20 nm thick layer of calcium to 20 mJ/cm^2 of 1064 nm light would raise its temperature by roughly 3000 K, consistent with the data of Fig. 8. We therefore conclude that the observed nanoparticle bleaching due to laser treatments at the three wavelengths (157, 532, and 1064 nm) are thermal in nature; the loss of color is due to of both removal and size reduction of the initial nanoparticles, where the metal is returning to lattice CaF_2 through reactions with interstitial forms fluorine.

In a typical laser conditioning scenario, the sample displays a range of defect sizes and thus a range of particle temperatures. If the particle temperature increases with particle size, as expected at 532 nm, the larger particles will be heated most effectively.

As they shrink, the temperature change will drop and annealing will slow. To remove the smaller particles, the fluence must be raised. The fluence can be safely raised in this scenario as long as the size of the largest particles has been reduced to a safe value. Step-wise increases in fluence could in principle removal virtually all the nanoparticles while minimizing damage to the host material.

At 1064 nm, the majority (greater than 90%) of the bleaching was observed after the first laser pulse. This is likely a consequence of the particle size dependence on absorption. At wavelengths near 1000 nm, the insert in Fig. 11 suggests that small particles absorb more laser energy per unit volume than large particles. Therefore, any fluence sufficient to bleach the larger particles will produce a much large temperature change in the small particles. In this case, a significant number of particles have been heated to temperatures near 2700 K. This degree of heating is likely to evaporate the smallest particles. The remaining, larger particles are not so strongly heated by subsequent pulses, and yield little, if any detectable blackbody radiation.

Material damage should be much harder to avoid at wavelengths near 1064 nm, where absorption decreases with increasing particle size. As the largest particles shrink, they inevitably reach a size where they absorb strongly. Fluences sufficient to heat the large particles will overheat the small particles. This situation is inherently unstable and should be avoided to minimize damage of the host material. In some cases, the design wavelength for a set of optics may be unsuitable for laser conditioning and another, more suitable wavelength must be found. The choice of conditioning wavelength is often complicated by the lack of information on the specific defects affected by the conditioning process.

In principle, simple laser conditioning can restore colored CaF_2 optics to a usable degree of transparency as shown by the samples in Figs. 5 and 7. Due to the very high uniformity required for optical elements used in photolithography, it is unlikely that such treatments would be sufficient for high resolution lithographic applications. However,

CaF_2 in less demanding applications, including UV windows in high radiation environments (e.g., inertial fusion systems), may benefit from treatments to remediate radiation-induced defects. Doped CaF_2 is also a thermoluminescent material; the production of point defects by radiation with subsequent exposure to lasers is of considerable interest because it influences the performance of the material as a dosimeter or radiation counter when read with a laser.

Conclusion

Spectroscopic and single wavelength transmission techniques allow for the real-time monitoring of nanoparticle formation and decay during electron and photon exposure. To a large degree, these particles can be removed by carefully chosen laser exposures, although surface damage can be a problem. Black body emission measurements and Mie absorption calculations suggest that laser-induced nanoparticle heating is significant and are consistent with a photothermal bleaching mechanism. This heating drives recombination of metallic Ca with fluorine from interstitial sites. The volume changes accompanying the lose or gain of charge on the calcium in the production and shrinkage of nanoparticles are crucial in maintaining the surrounding lattice. Time resolution of transmitted 532 nm light indicates that the bleaching event is happening on the time scale of nanoseconds after the laser pulse. It is likely that similar, thermal processes break up defect aggregates in rapidly grown crystals of optical materials in the practice of employing lower fluence burn-in treatments before their first exposure to potentially damaging, high fluence radiation.[3,4] Although the optical properties of these aggregates are often poorly understood, they have important consequences as to the design of laser conditioning treatments such as in situ cleaning processes.

Our results to date do not show complete recovery of transmission. Further study

on the use of variable wavelengths, programmed cycles in laser fluences, all in conjunction with thermal treatments, possibly at lower temperatures than previously studied, could lead to successful restoration of colored CaF_2.

Acknowledgements

This work was supported the United States Department of Energy under Contract DE-FG03-98ER14864. We thank Dr. Grant Norton and Joel B. LeBret for useful discussions on the crystallography of the irradiated specimens used in this study. We also thank Roland Bennewitz and Michael Reichling for helpful discussions.

References

[1] D. R. Sempolinski, T. P. Seward, C. Smith, N. Borrelli, and C. Rosplock, J. Non-Cryst. Solids **203,** 69-77 (1996).

[2] R. Schenker, F. Piao, and W. G. Oldham, in *Optical Micrography IX*; *Vol. 2726*, edited by G. E. Fuller (SPIE—Society of Photo-Optical Instrumentation Engineers, Bellingham, Washington USA, 1996), p. 698-706.

[3] M. J. Runkel, J. J. DeYoreo, W. D. Sell, and D. Milam, in *Laser conditioning study of KDP on the optical sciences laser using large area beams*, Boulder, CO, 1998 (SPIE—The International Society for Optical Engineering), p. 51-63.

[4] M. C. Staggs, M. Yan, and M. J. Runkel, in *Laser raster conditioning of KDP and DKDP crystals using XeCl and Nd:YAG lasers*, Boulder, CO, 2001 (SPIE—The International Society for Optical Engineering), p. 400-407.

[5] H. Bercegol, in *What is laser conditioning: A review focused on dielectric multilayers*, Boulder, CO, 1999 (SPIE—The International Society for Optical Engineering), p. 421-426.

[6] R. Bennewitz, C. Günther, M. Reichling, E. Matthias, S. Vijayalakshmi, A. V. Barnes, and N. H. Tolk, Appl. Phys. Lett. **66,** 320-322 (1995).

[7] V. S. Teodorescu, L. C. Nistor, and J. V. Landuyt, in *Defects in Insulating Materials*, edited by G. E. Matthews and R. T. Williams (Trans Tech, Zeurich, Switzerland, 1997), p. 671-674.

[8] M. Huisinga, N. Bouchaala, R. Bennewitz, E. A. Kotomin, M. Reichling, V. N. Kuzovkov, and W. v. Niessen, Nuclear Instruments and Methods in Physics Research B **141,** 79-84 (1998).

[9] L. P. Cramer, S. C. Langford, and J. T. Dickinson, to be submitted (2004).

[10] V. M. Orera and E. Alcalá, Phys. Stat. Sol. **38,** 621-627 (1976).

[11] V. M. Orera and E. Alcalá, Solid State Communications **27,** 1109-1112 (1978).

[12] F. Beuneu and P. Vajda, Journal of Applied Physics **78,** 6989-6993 (1995).

[13] M. Reichling, Nuclear Instruments and Methods in Physics Research B **101,** 108-114 (1995).

[14] R. Bennewitz, D. Smith, M. Reichling, E. Matthias, N. Itoh, and R. M. Wilson, Nuclear Instruments and Methods in Physics Research B **101,** 118-121 (1995).

[15] B. G. Ravi and S. Ramasamy, International Journal of Modern Physics B **6,** 2809-2836 (1992).

[16] L. W. Hobbs, Journal De Physique **37,** 3-25 (1976).

[17] J. B. LeBret, L. P. Cramer, M. G. Norton, and J. T. Dickinson, Submitted to Journal of Applied Physics (2004).

[18] R. Bennewitz, M. Reichling, and E. Matthias, Surface Science **387,** 69-77 (1997).

[19] C. Kunz, Z. Phys. **196,** 311-331 (1966).

[20] P. O. Nilsson and G. Forssell, Phys. Rev. B **16,** 3352-3358 (1977).

[21] W. T. Doyle, Phys. Rev. **111,** 1067-1072 (1958).

[22] M. Born and E. Wolf, *Principles of Optics*, Fourth ed. (Pergamon, Oxford, 1970).

[23] V. M. Orera and E. Alcalá, Phys. Scripta **44,** 717-723 (1977).

[24] V. M. Orera and E. Alcalá, Solid State Communications **27,** 1109-1112 (1978).

[25] A. G. Mathewson and H. P. Meyers, Phys. Scripta **4,** 291-292 (1971).

[26] J. C. Jaeger, Aust. J. Sci. Res. A **5,** 1-9 (1952).

[27] H. S. Carslaw and J. C. Jaeger, *Conduction of Heat in Solids*, Second ed. (Oxford, London, 1959).
[28] R. Blanc and R. Rivoira, C. R. Acad. Sci. Paris II B **265,** 1044-1045 (1967).
[29] M. R. Potter and G. W. Green, J. Phys. F **5,** 1426-1432 (1975).

Figure Captions

Fig. 1 Diagram of apparatus for real-time monitoring of nanoparticle bleaching at (a) 532 nm in air, and (b) 157 nm in vacuum.

Fig. 2 Absorption spectra of cleaved CaF_2 as a function of electron dose. The increase absorption with increasing electron dose reflects increasing nanoparticle densities. The shift to the main nanoparticle absorption to longer wavelengths at the highest electron dose reflects an increase in nanoparticle diameter.

Fig. 3 Absorption spectra of electron-irradiated (100 mC/cm^2) CaF_2 subsequently exposed to 532 nm laser radiation (20 mJ/cm^2). As the number of pulses of 532 nm radiation increases, the absorption drops.

Fig. 4 SEM image of the edge of an electron irradiated spot. The left half of the picture is the area with both electron and 532 nm radiation. The right side only received 532 nm radiation.

Fig. 5 Change of transmission signal at 532 nm during electron-irradiation ($0 < t < 10$ min) and subsequent 157 nm irradiation. The area bleached by 157 nm radiation is significantly smaller than the 532-nm probe beam spot. Thus the transmission signal does not completely recover, even though the bleached area is quite transparent.

Fig. 6 Optical image of an electron-irradiated CaF_2 sample which has been electron irradiation and had several localized bleaching treatments with 157 nm. The dark ovals were produced by electron irradiation. The clear spots in ovals were

produced by various durations of 157 nm.

Fig. 7 Comparisons of the darkened and bleached absorption at 532 nm for prolonged exposure to four laser wavelengths. The parameters for these exposures were: 157 nm: 50000 pulses at 150 mJ/cm^2; 248 nm: 1000 pulses at 300 mJ/cm^2; 532 nm: 1000 pulses at 50 mJ/cm^2; 1064 nm: 1000 pulses at 200 mJ/cm^2.

Fig. 8 Emission spectra acquired accompanying the first laser pulse of a bleaching treatment at 1064 nm. Spectral acquisition began a few ns after the laser pulse and continued for 1 μs. The broad continuum emission is consistent with black body radiation at a source temperature of 2700 K.

Fig. 9 Observed change in transmission of 532 nm light with 1064 nm laser light for three fluences a) 550, b) 400 and c) 275 mJ/cm^2. The insert shows a rise time of roughly 25 ns for the 550 mJ/cm^2 pulse.

Fig. 10 Absorption spectrum for each of the fluences irradiated with 1064 nm laser light. The gap in the data is due to the switching of the grating and light source in the spectrometer during the scan.

Fig. 11 Absorption per unit volume per unit fluence (dots) predicted by Mie theory for metallic calcium particles of radius 10 nm embedded in a CaF_2 matrix. The optical constants for metallic calcium were taken from Ref. [20,25]. The lines indicate predictions for 5-mm (solid) and 2-mm (dashed) diameter particles. The insert shows the expanded view for the region near 1000 nm.

Figure 1(a)

Setup for 532 nm experiments

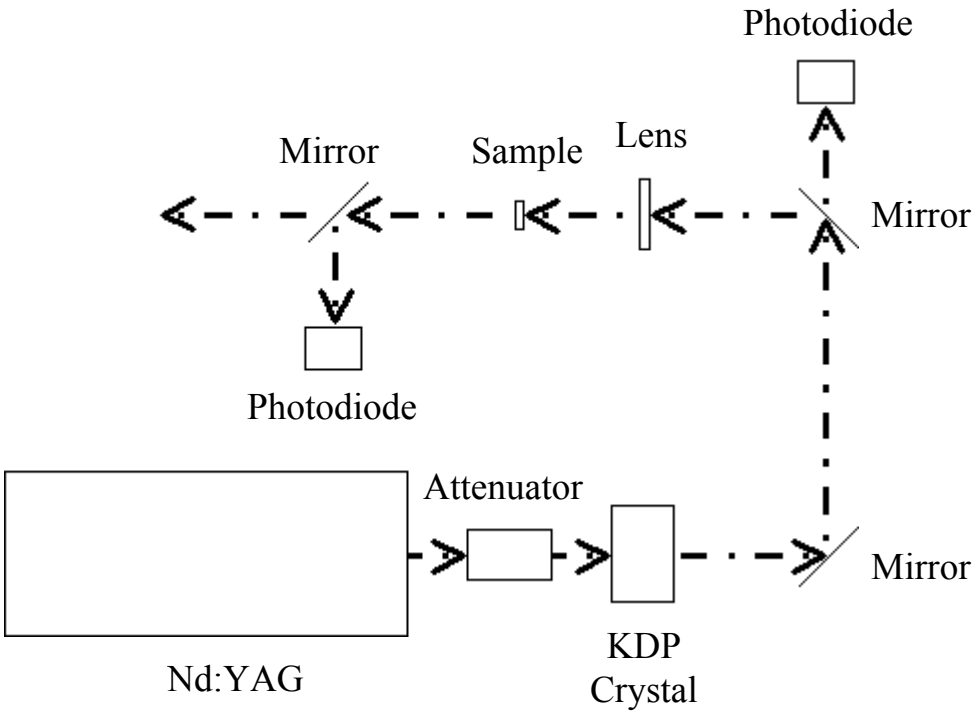

Figure 1(b)

Setup for 157 nm and electron treatments

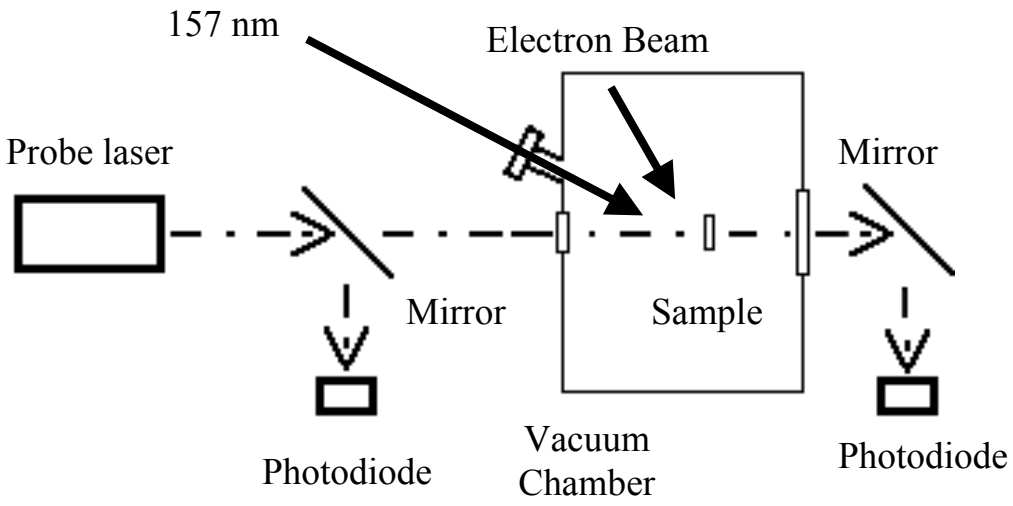

Figure 2

Spectrum of electron induced colloid growth in CaF_2

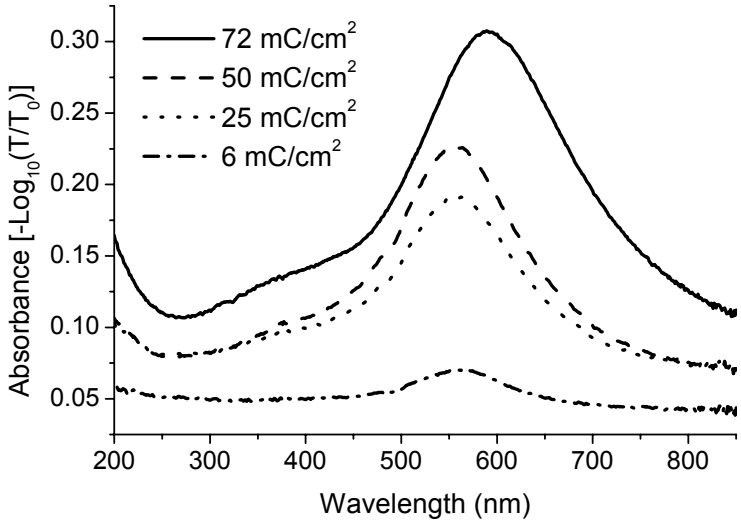

Figure 3

Effect of 532 nm laser light on electron irradiated CaF_2

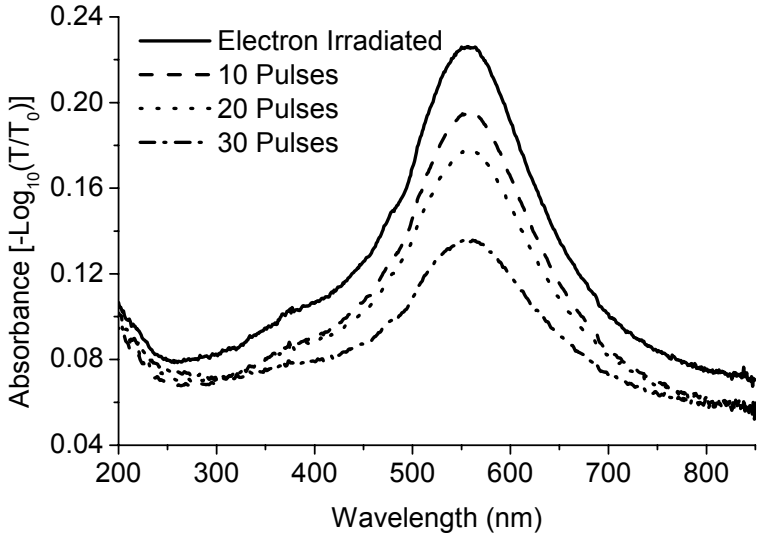

Figure 4

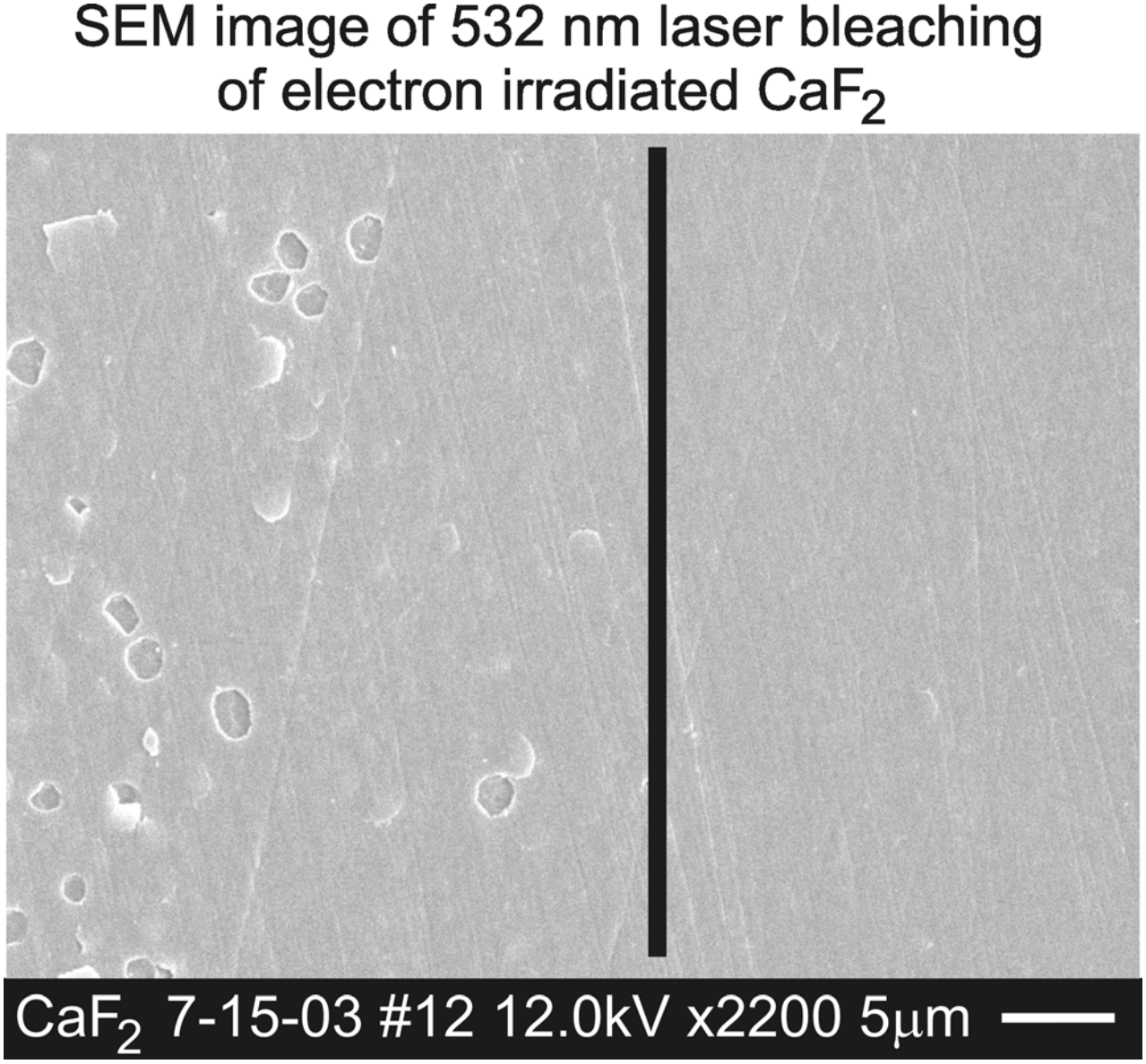
SEM image of 532 nm laser bleaching
of electron irradiated CaF_2
CaF_2 7-15-03 #12 12.0kV x2200 5μm

Figure 5

532 nm transmission with response to electron irradiation and 157 nm laser bleaching

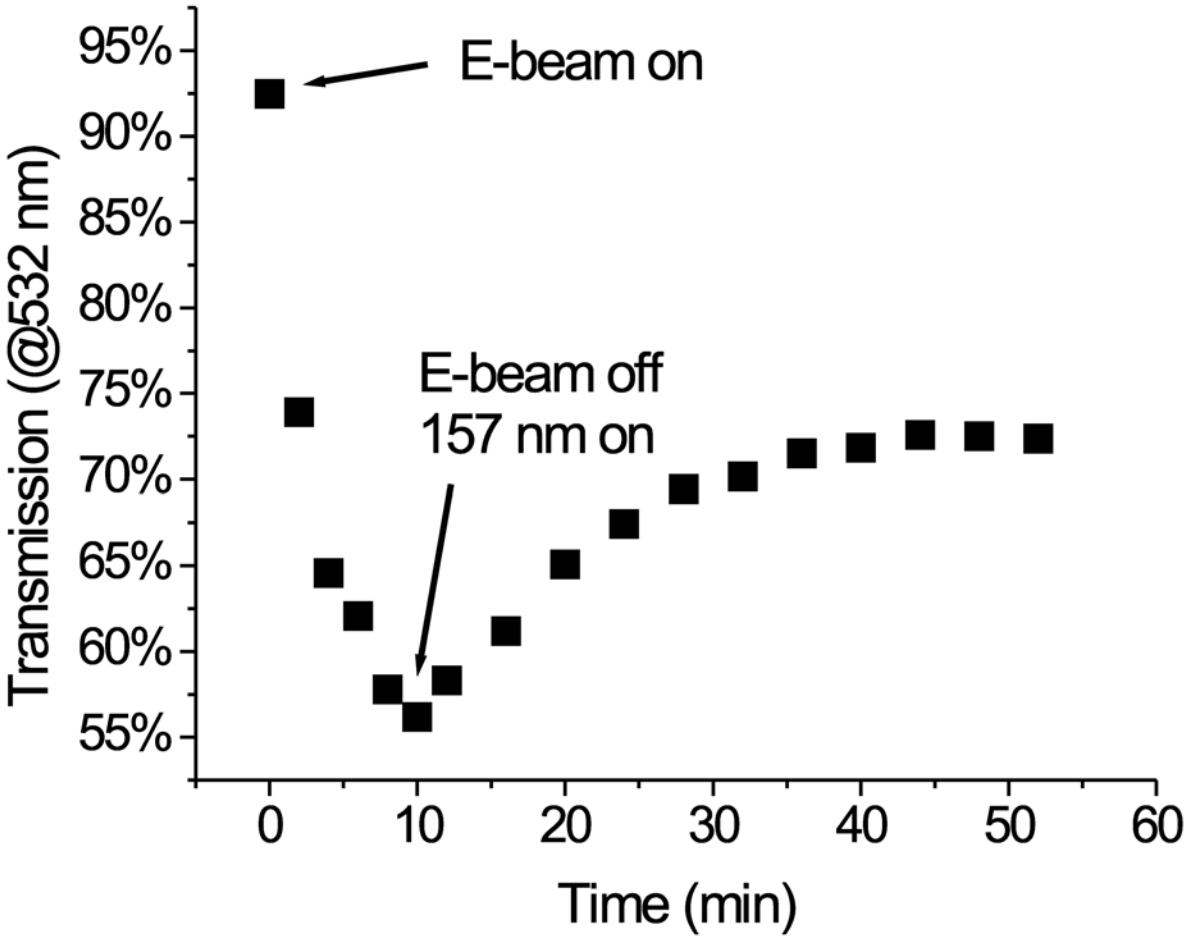

Figure 6

Colloids in CaF_2 partially bleached with 157 nm

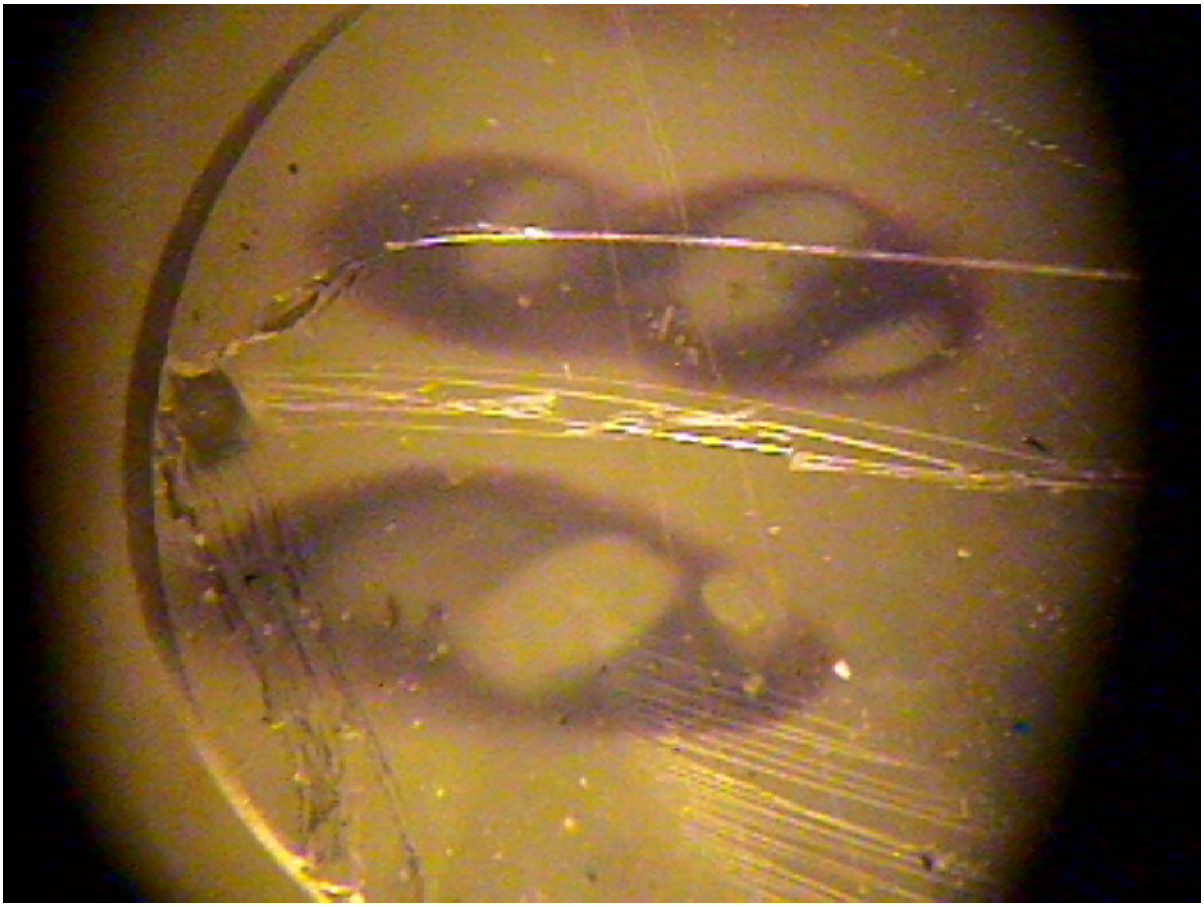

Figure 7

Comparison of absorption at 532 nm
before and after prolonged exposure
to four laser wavelengths

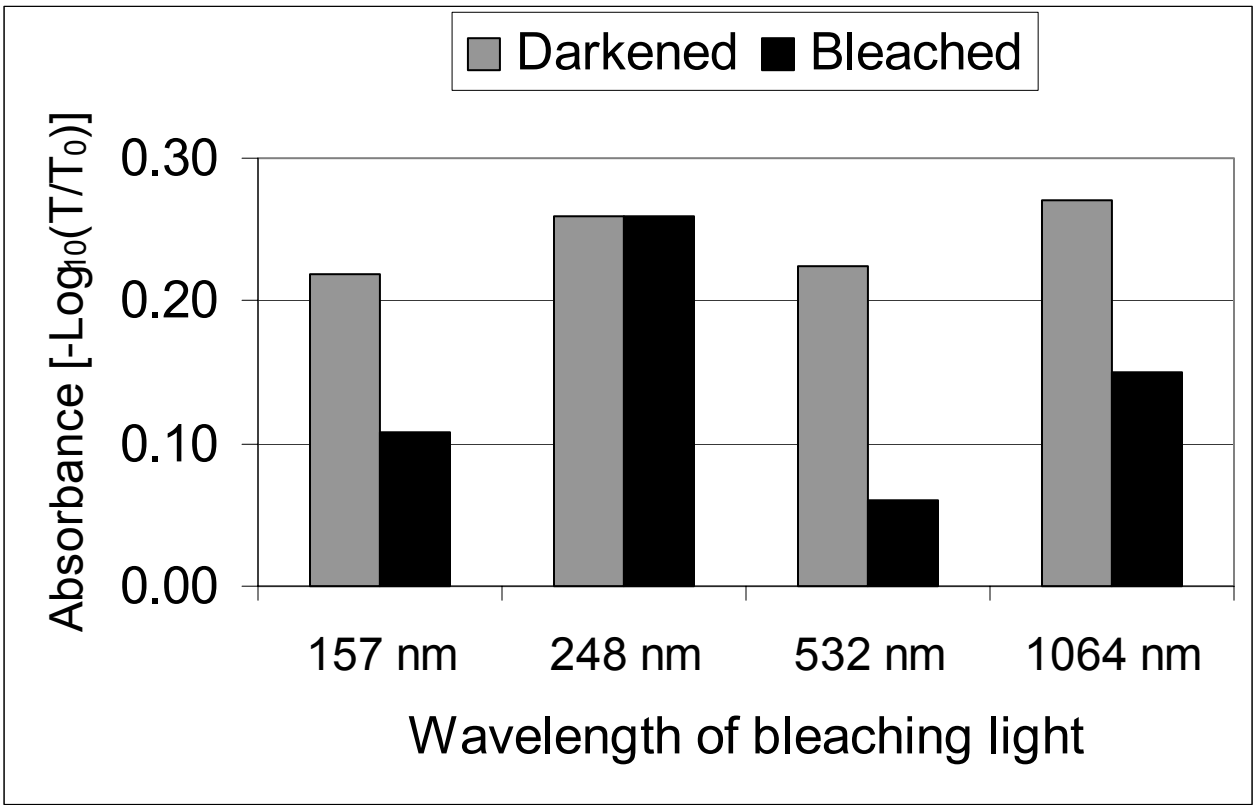

Figure 8

Emission spectra at 1064 nm

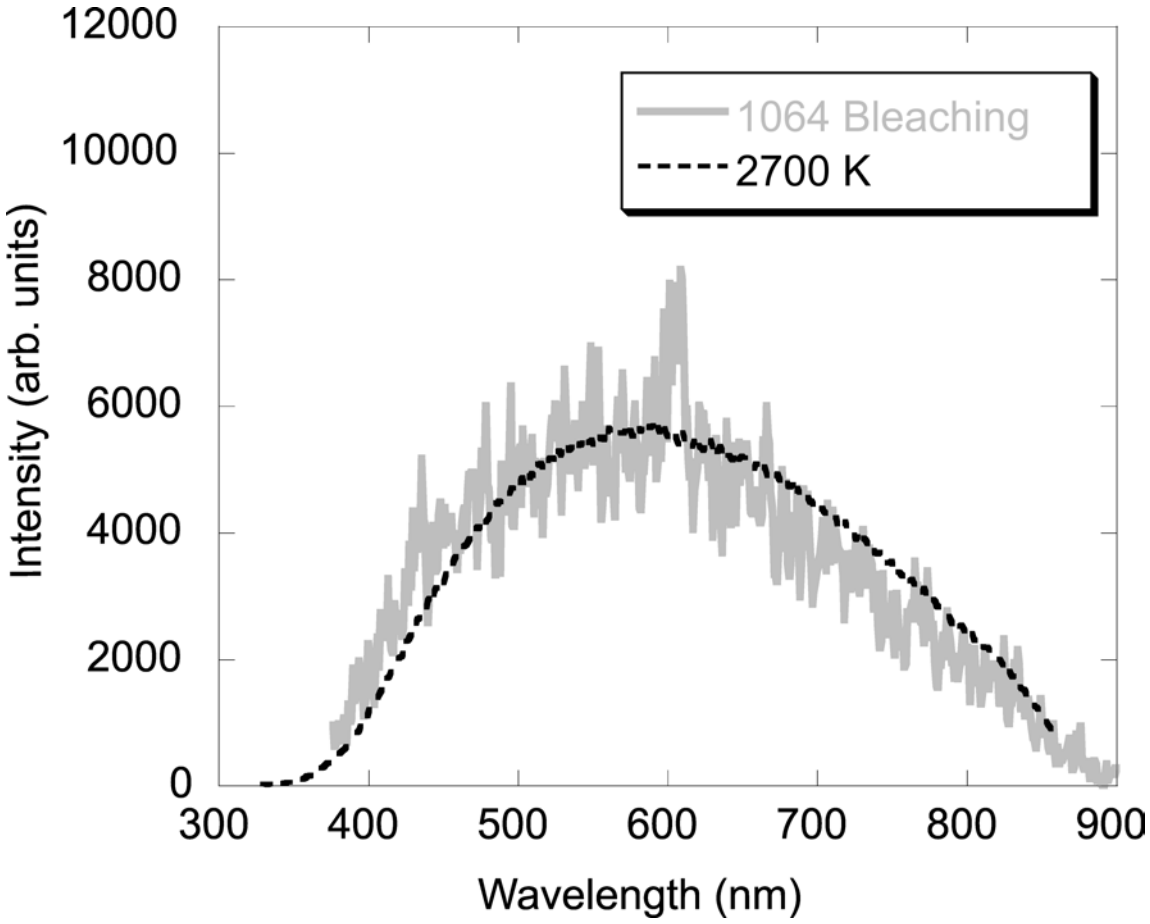

Figure 9

Change in transmission @532nm
with single pulse 1064 nm

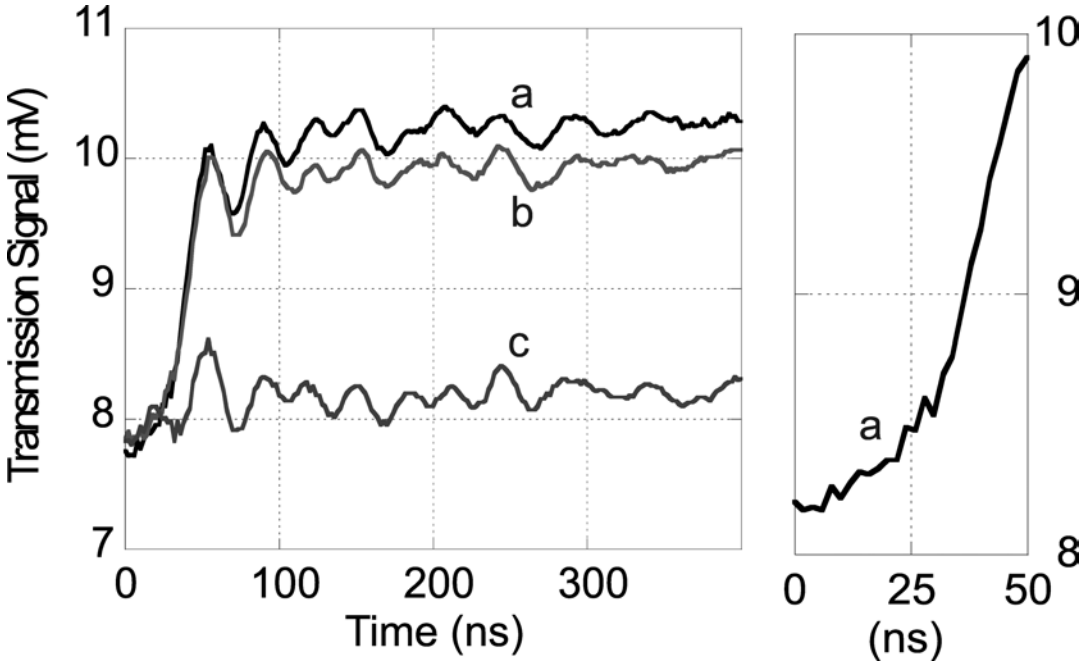

Figure 10

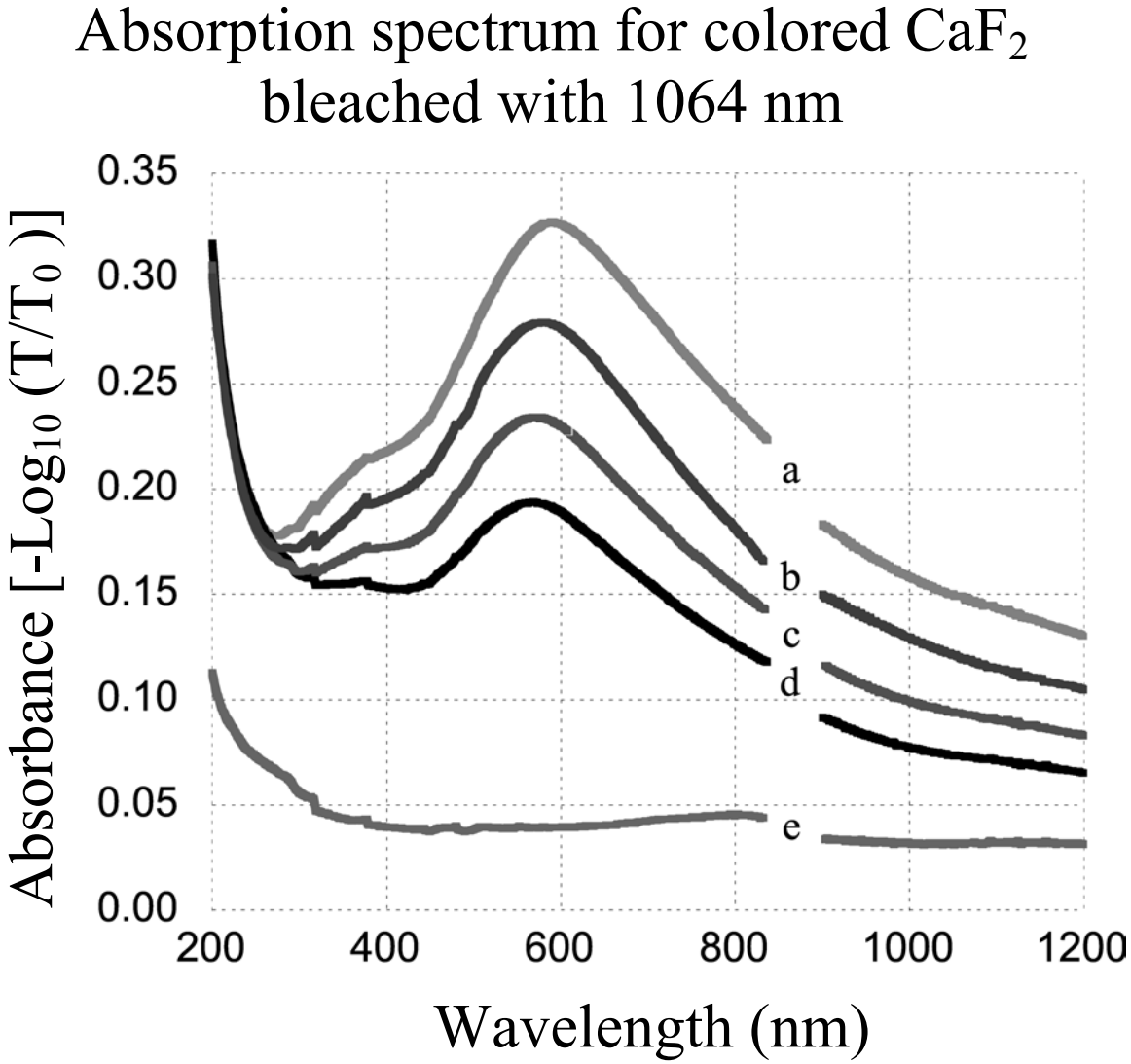
Absorption spectrum for colored CaF_2 bleached with 1064 nm
Absorbance [-Log10 (T/T0)]
0.35
0.30
0.25
0.20
0.15
0.10
0.05
0.00
200
400
600
800
1000
1200
Wavelength (nm)
a
b
c
d
e

Figure 11

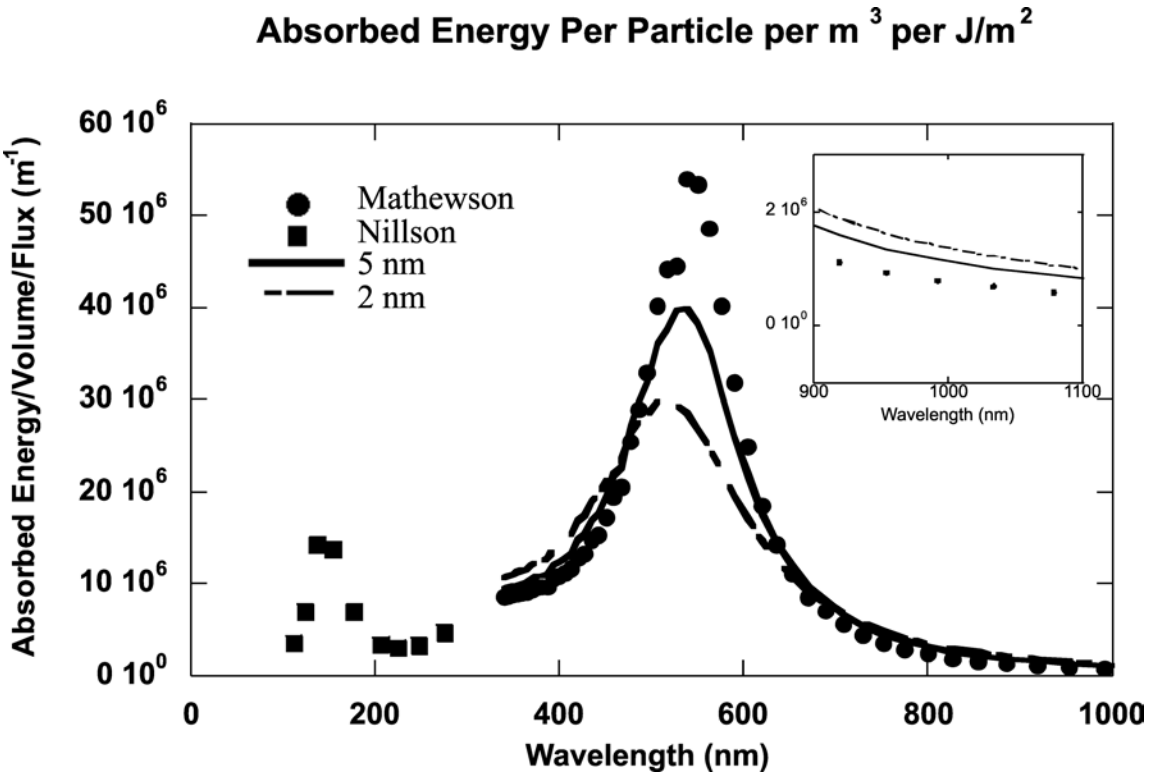
Absorbed Energy Per Particle per m 3 per J/m 2
Absorbed Energy/Volume/Flux (m-1)
60 10^6
50 10^6
40 10^6
30 10^6
20 10^6
10 10^6
0 10^0
0
200
400
600
800
1000
Wavelength (nm)
Mathewson
Nillson
5 nm
2 nm
2 10^6
0 10^0
900
1000
1100
Wavelength (nm)

Effect of surface treatments on STE luminescence in single crystal CaF_2

L. P. Cramer, T. D. Cumby, J. A. Leraas, S. C. Langford, and J. T. Dickinson*

Department of Physics and Materials Science Program, Washington State University, Pullman, WA 99164-2814

*Correspondence: email: jtd@wsu.edu; phone 509 335-4914; fax 509 335 7816

The self-trapped exciton (STE) is a fundamental excitation produced by relaxation of an electron-hole pair in a number of crystal lattices. We examine the luminescence derived from radiative decay of the STE in single crystal calcium fluoride (CaF_2). The initial excitation is produced by two-photon absorption accompanying excimer laser irradiation at 157 and 193 nm exposure. We show that the luminescence intensity is a strong function of surface treatments that produce or modify near-surface defects, including cleavage, electron irradiation, mechanical polishing, indentation, and heating.

Keywords: self trapped exciton, calcium fluoride, defects, dislocations, colloids

1. INTRODUCTION

CaF_2 with a nominal band gap of 11 eV[1,2] is currently in use as an optical refractory material for 193 nm photolithography and is a possible candidate for use at 157 nm. Defect generation in optical components is a concern for any high-powered laser applications. CaF_2 is known to degrade when exposed to prolonged excimer laser light, even though it is transparent to as low as 130 nm.[3] At sufficiently high laser intensities at both 193 nm (6.3 eV photons) and 157 nm (7.8 eV) the bandgap can be bridged by two-photon absorption. Two photon production of electron-hole pairs has been shown to generate point defects in CaF_2.[4,5] Thus defect production under prolonged vacuum-ultraviolet (VUV) exposure is a significant concern.[4,6,7]

Following production of electron-hole pairs, relaxation leads to the formation of self-trapped excitons (STEs) in CaF_2 (as well as BaF_2 and a number of alkali halides--the STE is often described as an electron associated with a V_K center). The STE can decay either by radiative decay (STE luminescence) or by non-radiative decay; the latter can be via lattice relaxations creating phonons (thus leading to heating of the crystal)[4,8] or alternatively, the creation of F- and H-centers.[9] The STE luminescence yields a broadband peak centered typically near 280 nm.

In this paper we report the influence of various surface treatments of crystalline CaF_2 on the STE photoluminescence excited via two-photon absorption with nanosecond pulses of excimer laser light. Tsujibayashi has shown that the STE luminescence intensity and spectrum is affected by pre-existing defects.[10] In this context, we find that cleaved samples typically display low densities of near-surface defects, while samples that have been polished, indented, scratched material as well as keV energy electron irradiation displays higher defect densities. Conversely, annealing treatments typically reduce the density of near-surface defects. In this study, the average intensity of the STE photoluminescence is used to compare the relative number of self-trapping sites created

by introducing defects with various surface treatments. Understanding the effects that defects have on generation of STE photoluminescence produced by 157 and 193 nm irradiation may be of use in the development of reliable, high quality optical materials for use in this important region of the spectrum.

2. EXPERIMENTAL DETAILS

Vacuum-ultraviolet grade CaF_2 was purchased from Korth Kristalle GmbH, cleaved in air along the (111) plane into 0.2 cm thick, 1-cm diameter disks, and mounted in vacuum. The schematic of our experimental set-up is shown in Fig. 1. Experiments were carried out at pressures less than 1×10^{-7} Pa. The sample mount allowed for precise positioning of each sample for electron or laser irradiation. Electron irradiation was performed with an Auger electron gun operated at a beam current of 100 μA focused to a roughly 3×5 mm^2 spot on the sample at 2 keV. In this work, the STE luminescence was excited with 157 nm radiation from a Lambda Physik LPF 200 excimer laser (F_2, 20-ns pulses) and with 193 nm radiation from a Lambda Physik Lextra 200 excimer laser (ArF, 30-ns pulses). Dry nitrogen was used between the 157 nm excimer laser and the vacuum system to avoid any interaction with oxygen or water.

Sample annealing was performed in vacuum with a resistive heater. The approximate sample temperature was determined with a chromel-alumel thermocouple spot-welded to the sample holder next to the sample. Voltage readings of the thermocouple were made every five minutes. After removing the samples from vacuum, defects were characterized by UV-VIS absorption in a Perkin Elmer Lambda 900 spectrophotometer.

Surface treatments prior to mounting in vacuum include “as is” (cleaved), polishing, indentation, scratching, and surface roughing. The reported spectra represent a survey (average of 10 sites) of the surface to provide an average result of the various

treatments. Normally, spot-to-spot variations in the acquired spectra were small. Polished samples were cut with a diamond saw or cleaved and polished with aluminum oxide abrasives and finished with 0.1 μm diamond paste. Polishing was performed in methanol rather than aqueous media to minimize oxide formation. Scratching and indentation were performed with a diamond scribe or a dry and thoroughly cleaned 0.8 mm steel ball.

A fused silica fiber optic was used to bring light from the specimen to the spectrometer. A Roper Scientific PI-Max Intensified CCD was used to image the spectra produced by a Model 82-479 Thermo Jarrel Ash Spectrometer with 300 lines/mm grating blazed at 400 nm. The intensifier was used with an exposure (gate-window) of 5 μs, which started immediately after the laser pulse. Typical spectra were averages over 1000 laser pulses acquired at a repetition rate of 20 Hz.

3. RESULTS

We first show the characteristics of the STE luminescence acquired on cleaved samples. Typical luminescence spectra excited at 157 and 193 nm both at 120 mJ/cm^2 on cleaved CaF_2 are shown in Fig. 2. Both spectra show peaks at 280 nm and are consistent with STE luminescence spectra reported elsewhere.[10,11] With 248 nm excitation (5 eV photons), no measurable STE luminescence was detected. As we raised the fluence at 248 nm, surface breakdown would occur before any STE luminescence was seen. For the 11 eV CaF_2 bandgap, STE production at 157 nm (7.8 eV) and 193 nm (6.3 eV) both require only two photons, versus three photons at 248 nm, thus inhibiting electron-hole pair production at 248 nm. Also, we note that STE photoluminescence from cleaved surfaces were typically narrower in spectral width and therefore were used for the base line for further mechanical treatments.

As verification that the initial electron-hole production induced by the pulses at

157 and 193 nm was via two-photon absorption, we examined the laser intensity dependence of the STE photoluminescence. A plot of the log of the luminescence intensity vs. the log of the laser intensity at 157 nm is shown in Fig. 4. The resulting slope of the linear portion of the curve is 1.8 ± 0.3, consistent with a two-photon absorption mechanism. A similar experiment at 193 nm yielded a slope of 2.2 ± 0.3, again consistent with a two-photon process. It should be noted that in Fig. 3, there appears to be a saturation of the STE at higher 157 nm laser fluence. We have recently found that exposure of CaF_2 to 157 nm light results in a dramatic production of single photon absorption centers.[3] The absorption is most evident at higher laser fluences and due to competition for photons results in a decreasing efficiency for two-photon absorption.

The STE luminescence lifetime is a signature verifying STE formation; we measured this lifetime by acquiring a series of spectra as a function of delay after the laser pulse with constant acquisition window (0.5 μs). Figure 4 shows the natural log of the integrated STE luminescence intensity generated with 140 mJ/cm^2 of 193 nm laser light as a function of delay time relative to the laser pulse. The linear plot shows that the luminescence decays exponentially and the slope yields a lifetime of 1.14 ± 0.1 μs, consistent with a previously determined value for STE decay for CaF_2.[4] A similar experiment at 157 nm yielded a similar value for the lifetime of 1.27 ± 0.2 μs. We thus conclude that the luminescence of Fig. 2 is due to radiative decay following two-photon generation of self-trapped excitons.

We now consider the influence of various surface/near surface treatments on the STE spectrum and intensity. It is well known that polishing cleaved surfaces of ionic materials often produces a micron-thick layer of deformed material, which can significantly enhance laser absorption and the resulting luminescence.[12,13] The CaF_2 STE luminescence comparing a cleaved surface and a polished surface is shown in Fig. 5; excitation at 157 nm (87 mJ/cm^2) is seen in Fig. 5a and excitation at 193 nm (80 mJ/cm^2)

is seen in Fig. 5b. The spectrum for cleaved specimens (labeled Cleaved a, Cleaved b) both peak at 280 nm. The curve for Cleaved b shows a slight broadening at ~350 nm which we attribute to cleavage generated defects. Cleavage is known to generate local regions of plastically deformed crystal during cleavage step formation.[14,15] Plastic deformation of ionic crystals frequently generates vacancies.[16,17] The consequences of polishing the surface, mechanically much more disruptive to the near surface lattice, shows a dramatic increase in intensity and very strong shoulders at longer wavelengths (Fig. 5a and 5b). Our explanation of these changes is as follows: the defects produced by deformation provide local distortion of the lattice, which promote STE trapping and simultaneously alter the environment (therefore shifting the spectrum to longer wavelengths). Tsujibayashi observed a similar, defect-induced broadening to the STE luminescence peak in material with residual impurities or defects in the crystal.[10]

The same type of defects can also be generated during indentation of ionic crystals. Indentation results in plastic deformation and compression to the lattice, accompanied by significant dislocation motion and point defect production. Using a steel sphere (radius ~0.8 mm) to apply pressure on a cleaved surface (avoiding entirely any fracture) we were able to influence the intensity of the STE luminescence as seen in Fig. 6. Lightly indenting the surface (the top curve in Fig. 6) increases the luminescence intensity compared to the middle curve, which is the STE luminescence from the cleaved surface. However, higher indentation forces (lower curve in Fig. 6) result in lower luminescence intensities. The virtual absence of features large enough to scattered light suggests that the differences in STE luminescence intensities are due to the density and nature of the defects produced by light and heavy indentation. Unlike the polishing treatment, indentation does not show the addition of the 350 nm luminescence peak. Therefore the polishing-induced shift in Fig. 5 cannot be attributed to simple deformation processes.

Another treatment to create defects in the near surface region is to irradiate the

surface with low-energy electrons. In CaF_2, electron irradiation at room temperature produces defect aggregates, including metallic calcium colloids.[18,19] Numerical estimates indicate that these colloids would absorb significantly at 157 nm.[20]

Electron irradiating (500 mC/cm^2) polished sample leads to increased STE luminescence as seen in Fig. 7. Fluences of 60, 100 and 120 mJ/cm^2 for both polished and polished and electron treated samples are illustrated with the average integrated intensity represented by bar graphs. The gray bars are the results from the polished sample and the black bars are from the polished and electron irradiated sample. In both cases the luminescence intensity increases nonlinearly with fluence. For these three points the least squares fits to a power-law behavior yield an exponent of 1.8, consistent with our previous results for a two-photon excitation.

Defects produced by electron-irradiation also have a significant affect on the STE luminescence intensities. The bars in Fig. 7 reflect the integrated luminescence intensities for polished samples at three fluences of 157 nm laser light. The samples were subsequently electron irradiated (1200 mC/cm^2 dose) and resample for the same range of fluences. Similar electron-irradiation treatments have been shown to produce metallic nanoparticles (calcium colloids) in CaF_2, with radii on the order of 20 nm. In related work, we show that such colloids are expected to absorb significantly at 157 nm.[3] Although this absorption would compete with STE production for 157 nm photons, the net effect of electron irradiation is to increase the STE luminescence intensity.

Annealing treatments typically increase defect mobility and can dramatically alter defect distributions and luminescence intensities. Annealing additively colored (calcium enriched) CaF_2 has shown to increase nanoparticle size with increasing temperatures.[21] Figure 8 compares average luminescence intensities observed immediately after electron irradiation (1200 mC/cm^2 dose), and after subsequent 30 minute anneals at 50 and 180 °C, respectively. Significantly, both annealing treatments increase the STE luminescence intensities; with the high temperature anneal increasing the luminescence intensities still

further. This is inconsistent with naïve expectations that annealing treatments reduce the density of defects that increase the intensity of luminescence.

4. DISCUSSION

STE luminescence in alkali halides is generated by photons being emitted during electron-hole recombination.[22] It is a similar process in fluorite crystals where a self-trapped hole, or V_k center (two adjacent halide ions bound to each other in a X_2^- molecular configuration),[23] can recombine with an electron radiatively. The resulting luminescence has a fairly wide distribution at room temperature with a peak intensity centered near 280 nm.

STE formation in CaF_2 at excimer laser wavelengths has been studied by several research groups.[4,5,24] As expected,[1,2] Görling et al. found that STE formation requires two-photon excitations at both 193 and 157 nm.[4] Interestingly, Görling et al. found that two-photon absorption in CaF_2 as measured by a calorimetric technique was considerably greater at 193 nm than at 157 nm. Görling estimated the amount of energy that was being absorbed by a crystal by measuring how fast its temperature changed during exposure to laser radiation in vacuum. This technique is sensitive only to absorbed energy that is converted to heat. They attributed the low measured two-photon absorption at 157 nm to the generation of photoelectrons at this wavelength; these photoelectrons carry energy away from the crystal and thus reduce the laser-induced heating. This explanation is supported by observations by Huisinga et al.[25] where photoemission from CaF_2 during exposure to 157 nm laser light was observed. In principle, the energy carried away by photoelectrons is also not available to produce STE luminescence. However, the intense STE luminescence produced by 157 nm radiation shown in Fig. 2 suggests that the production of STE luminescence is relatively efficient despite any photoelectron emission.

The presence of appropriate defects influences the probability of STE luminescence significantly. Tsujibayashi et al. showed that residual impurities or defects in the crystal influenced the STE luminescence peak.[10] We find that by simply polishing the sample we can introduce more STE luminescence sites as seen in Fig. 5. Plastic deformation is known to generate point defects (vacancies) in crystalline materials.[16] As long as the point defect density is not too high, they can increase luminescence intensities by increasing the probability that STEs decay radiatively rather than non-radiatively (generating heat). The electric fields in ionic crystals are altered near defects, and these fields can promote radiative exciton decay. In our case, the fraction of excitons decaying to produce light increases. However, if the density of point defects becomes too high, the energy released as the exciton decays is converted to heat (phonons) instead of light. The defect density created by deformation depends strongly on the force applied to the indenter. Low forces generate low defect densities that increase luminescence, but high forces generate high defect densities than quench luminescence (see Fig. 6).

A similar phenomenon is observed in the cathodoluminescence from single crystal in indented MgO vs. indentation force. Indents produced at low forces are surrounded by point defects that increase the luminescence intensities stimulated by electron irradiation (cathodoluminescence).[26,27] At high indentation forces, highly deformed regions (near the center of the indent, where the forces and defect densities are highest) emit very little light. This is attributed to the quenching of excited states (releasing heat instead of light) at high defect densities.[28,29] In CaF_2, the high defect densities produced by high force indentation appear to quench luminescence in much the same fashion.

Electron irradiation of CaF_2 at room temperature is known to produce F and H center pairs. F-centers produced by electron irradiation tend to aggregate, producing regions of low fluorine concentration. If the F-centers donate their electrons to nearby calcium ions, the ions are reduced to calcium metal (Ca° has a 6% larger volume than

Ca^{2+} and exerts pressure on the surrounding lattice). This process produces calcium nanoparticles on the order of twenty nanometers in diameter.[30,31] Although these nanoparticles can in principle absorb energy from the laser and therefore would be expected to reduce the STE luminescence, the net effect of electron irradiation that we observe is to approximately double the STE luminescence from polished surfaces (See Fig. 7).

The kinetic energies of the 2 keV electrons employed here are much higher than the laser photon energies employed above. As these 2 keV electrons penetrate the surface, they interact strongly with the fluorine ions and generate large numbers of electron-hole pairs. Calculations for 1 keV electrons indicate that the probability that a single electron will produce an exciton in the first atomic layer of CaF_2 molecules is about 30%. Thus electron irradiation can produce an enormous number of excitons near the surface. Typical 2 keV electrons are expected to travel ~100 nm into the crystal (about 200 CaF_2 layers).[32] Secondary electrons (electrons produced by collisions with electrons from the electron beam) travel somewhat deeper into the lattice producing defects which we were able to observe by etching with HCl and image by AFM.[33] Clearly, 2 keV electrons produce a tremendous number of defects as they lose energy to the lattice. If the resulting defects are the trapping sites, the related increase in defects enhances the probability of radiative decay for the STEs (see Fig. 7).

Orera et al. have shown that annealing treatments (similar to that of Fig. 8) promote the growth of defect aggregates and nanoparticles in thermochemically reduced calcium fluoride.[34] Annealing treatments allows for increased defect mobility at elevated temperatures, which enhances defect aggregation, instead of defect recombination. This results in larger numbers of nanoparticles, which do reduce the transmission at 157 nm (unpublished work), but also helps to enhance the remaining defects. The thermal treatment after electron irradiation is seen in Fig.8 and shows the enhanced STE luminescence.

Interestingly, Bennewitz et al. estimated from simultaneous measurements of the absorption spectra during electron irradiation that the nanoparticle radius during electron radiation was about a factor of three less than the radius after the electron beam was turned off, apparently due to heating by the electron beam during irradiation.[18] Since larger nanoparticles are produced at higher temperatures,[34] larger nanoparticles are associated with more intense STE luminescence with our increased STE luminescence intensity after annealing (see Fig. 8). Bennewitz' observation suggests that the effect of nanoparticle size (or defect density in the surrounding material) during 157 nm irradiation is not due to changes in absorption at 157 nm alone.

The defects generated by the treatments described are the following: F-centers, dislocations, and nanoparticles. Defects create a stress gradient in the surround lattice to accommodate the change in the perfect lattice. The stress gradients around these defect structures can be another important factor that can add to enhanced exciton. In the perfect lattice self-trapping requires lattice relaxation, having defects creating stress gradients would assist relaxation enhancing STE radiative decay.

5. CONCLUSION

We have shown that defects introduced into CaF_2 via surface treatments such as electron irradiation, polishing, indentation and annealing increases the STE luminescence intensity. High levels of defects can lead to the reduction of the lifetime for optical components in this important spectral range. Measurements on new optical components utilizing STE luminescence generated with 157 nm could in principle be employed to determine if the defect densities produced by mechanical polishing have been reduced to acceptable levels.

ACKNOWLEDGMENTS

This work was supported by the United States Department of Energy under Contract DE-FG02-04ER15618. We thank Wayne Hess, Pacific Northwest National Laboratory, for helpful discussions.

References

[1] R. A. Heaton and C. C. Lin, Physical Review B **22,** 3629-3638 (1980).

[2] R. A. Evarestov, I. V. Murin, and A. V. Petrov, Journal of Physics: Condensed Matter **1,** 6603-6609 (1989).

[3] L. P. Cramer, S. C. Langford, and J. T. Dickinson, to be submitted (2004).

[4] C. Görling, U. Leinhos, and K. Mann, Optics Communications **216,** 369-378 (2003).

[5] T. Tsujibayashi and K. Toyoda, Applied Physics Letters **80,** 2883-2885 (2002).

[6] V. Liberman, T. M. Bloomstein, M. Rothschild, J. H. C. Sedlacek, R. S. Uttaro, A. K. Bates, C. V. Peski, and K. Orvek, J. Vac. Sci. Technol. B **17,** 3273 (1999).

[7] M. Mizuguchi, H. Hosono, and H. Kawazoe, Journal of the Optical Society America B **16,** 1153-1159 (1999).

[8] C. Görling, U. Leinhos, and K. Mann, Applied Physics B **74,** 259-265 (2002).

[9] K. Tanimura, Physical Review B **63,** 184303 1-4 (2001).

[10] T. Tsujibayashi, M. Watanabe, O. Arimoto, M. Itoh, S. Makanishi, H. Itoh, S. Asaka, and M. Kamada, Journal of Luminescence **87-89,** 254-256 (2000).

[11] R. T. Williams, M. N. Kabler, W. Hayes, and J. P. Stott, Phys. Rev. B **14,** 725-740 (1976).

[12] J. T. Dickinson, L. C. Jensen, R. L. Webb, and S. C. Langford, J. Non-Cryst. Solids **177,** 1-8 (1994).

[13] J. T. Dickinson, L. C. Jensen, R. L. Webb, and S. C. Langford, in *Laser Ablation: Mechanisms and Applications II*; *Vol. 288*, edited by J. C. Miller and D. B. Geohegan (American Institute of Physics, New York, 1994), p. 13-25.

[14] S. J. Burns, Philos. Mag. Series 8 **18,** 625-636 (1968).

[15] J. J. Gilman, Trans. Metall. Soc. AIME **212,** 310-315 (1958).

[16] W. T. Read Jr., in *Dislocations in Crystals* (McGraw Hill, New York, 1953), p. 85-88.

[17] G. A. Andreev and B. I. Smirnov, Fiz. Tverd. Tela **10,** 1693-1698 (1968).

[18] R. Bennewitz, C. Günther, M. Reichling, E. Matthias, S. Vijayalakshmi, A. V. Barnes, and N. H. Tolk, Appl. Phys. Lett. **66,** 320-322 (1995).

[19] V. S. Teodorescu, L. C. Nistor, and J. V. Landuyt, in *Defects in Insulating Materials*, edited by G. E. Matthews and R. T. Williams (Trans Tech, Zeurich, Switzerland, 1997), p. 671-674.

[20] L. P. Cramer, B. B. Schubert, P. Petite, S. C. Langford, and J. T. Dickinson, J. Appl. Phys. **(submitted)** (2004).

[21] V. M. Orera and E. Alcalá, Phys. Stat. Sol. **38,** 621-627 (1976).

[22] R. T. Williams and M. N. Kabler, Physical Review B **9,** 1897-1907 (1974).

[23] R. T. Williams, M. N. Kabler, W. Hayes, and J. P. Stott, Physical Review B **14,** 725-740 (1974).

[24] P. B. Sergeev, Quantum Electronics **32,** 344-348 (2002).

[25] M. Huisinga, M. Reichling, and E. Matthias, Physical Review B **55,** 7600-7605 (1997).

[26] M. Y. Khan, L. M. Brown, and M. M. Chaudhri, Journal of Physics D.: Applied Physics **25,** A257-A265 (1992).

[27] M. M. Chaudhri, J. T. Hagan, and J. K. Wells, Journal of Materials Science **15,** 1189-1193 (1980).
[28] S. J. Pennycook and L. M. Brown, J. Lumin. **18/19,** 905-909 (1979).
[29] C. Ballesteros, J. Llopis, and J. Piqueras, J. Appl. Phys. **53,** 3201-3206 (1982).
[30] R. Bennewitz, M. Reichling, R. M. Wilson, R. T. Williams, K. Holldack, M. Grunze, and E. Matthias, Nuclear Instruments and Methods in Physics Research B **91,** 623-627 (1994).
[31] R. Bennewitz, M. Reichling, and E. Matthias, Surface Science **387,** 69-77 (1997).
[32] R. Bennewitz, D. Smith, M. Reichling, E. Matthias, N. Itoh, and R. M. Wilson, Nuclear Instruments and Methods in Physics Research B **101,** 118-121 (1995).
[33] L. P. Cramer, F. Stevens, and J. T. Dickinson, to be submitted (2004).
[34] V. M. Orera and E. Alcalá, Solid State Communications **27,** 1109-1112 (1978).

Figure Captions

Figure 1

Fig. 1 Experimental set-up for STE luminescence measurements.

Figure 2

Fig. 2 Spectra of STE luminescence from cleaved CaF_2 generated by exposure to 157 and 193 nm radiation at 120 mJ/cm^2. Spectra acquisition began immediately after each laser pulse and continued for 5 μs. Data were integrated for 1000 pulses. The spectra have not been corrected for camera and spectrometer response.

Figure 3

Fig. 3 Log-Log plot of STE luminescent intensity versus 157 nm laser fluence. The slope is 1.8 ± 0.3, consistent with two photon absorption.

Figure 2

Fig. 4 The natural log of the STE luminescence intensity vs. delay time, acquired with a 0.5 μs window for a cleaved CaF_2 sample. The slope yields a time constant of 1.27 μs.

Figure 5

Fig. 5 STE luminescence spectra for cleaved and polished CaF_2 irradiated with a) 157 nm at 87 mJ/cm^2 and b) 193 nm at 80 mJ/cm^2. The integrated intensity shows the polished sample is ~2X greater than cleaved samples.

Figure 6

Fig. 6 STE luminescence intensities changes due to indentation with steel ball irradiated with 157 nm at 290 mJ/cm^2. The dashed-line spectrum is the lightest indenting, the solid black is the cleaved surface, and the dot-line spectrum is a heavily indented surface. 0.8 mm steel ball.

Figure 7

Fig. 7 STE luminescence average intensity as a result of 1000 pulses of 157 nm irradiation on polished CaF_2 and electron irradiated polished surface at three fluences.

Figure 8

Fig. 8 STE luminescence averaged intensity from electron-irradiated polished sample that was annealed twice in vacuum and probed with 157 nm (300 mJ/cm^2) at room temperature.

Figure 1

Typical luminescence set-

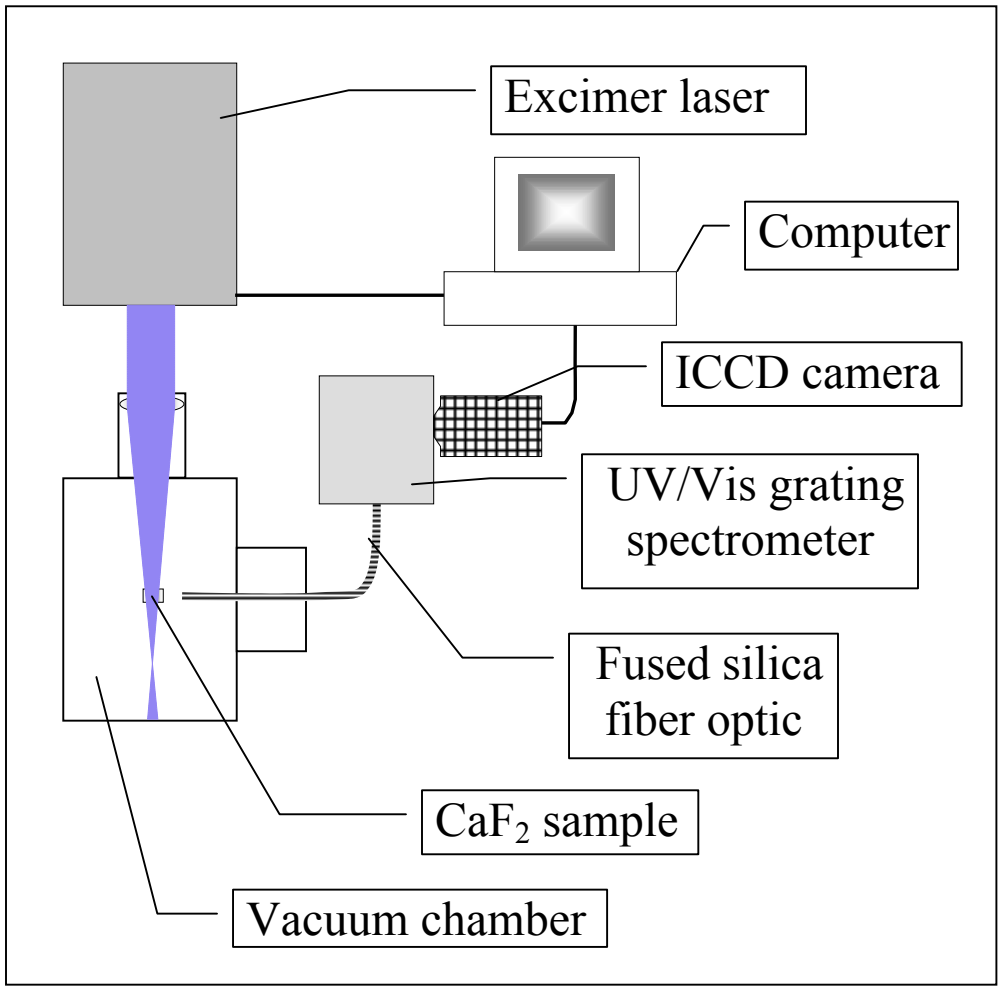

Figure 2

Luminescence spectra for cleaved CaF_2

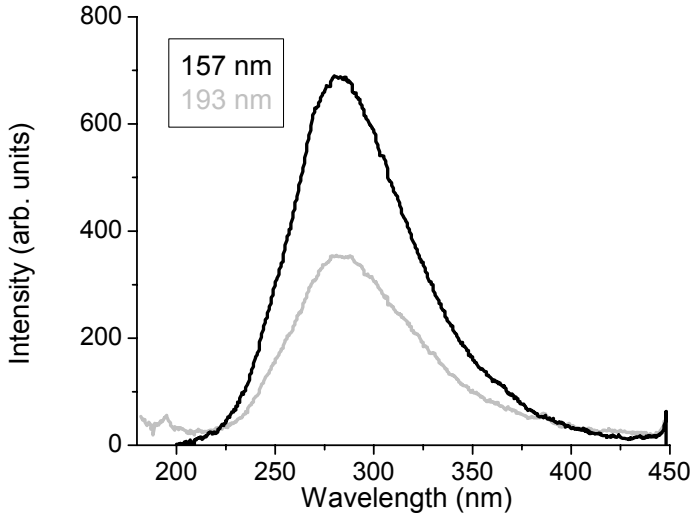

Figure 3

STE luminescence as a function of delay time relative to the laser pulse

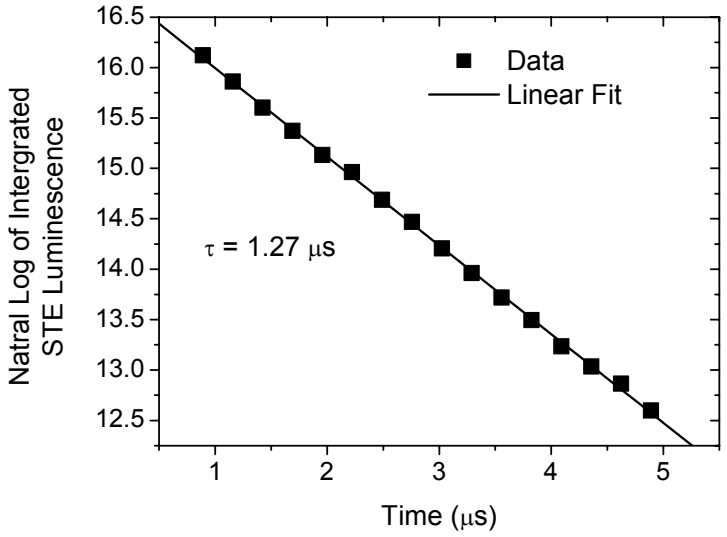

Figure 4

Integrated luminescence
plotted on a log-log scale

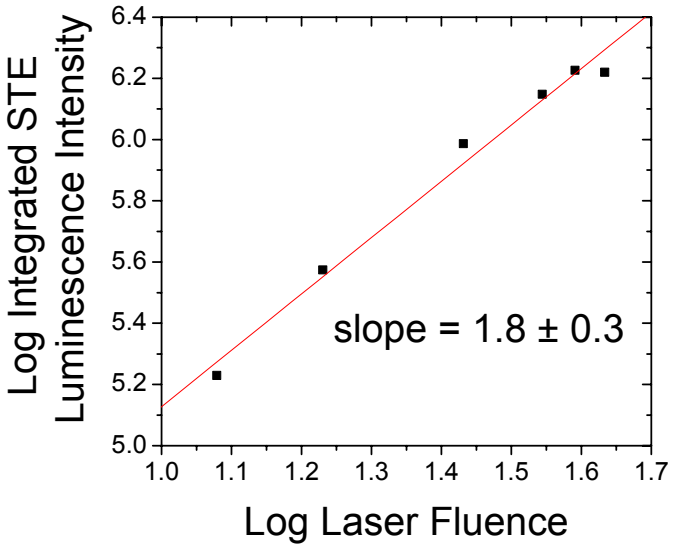

Figure 5(a)

STE luminescence comparing
cleaved and polished at 157 nm

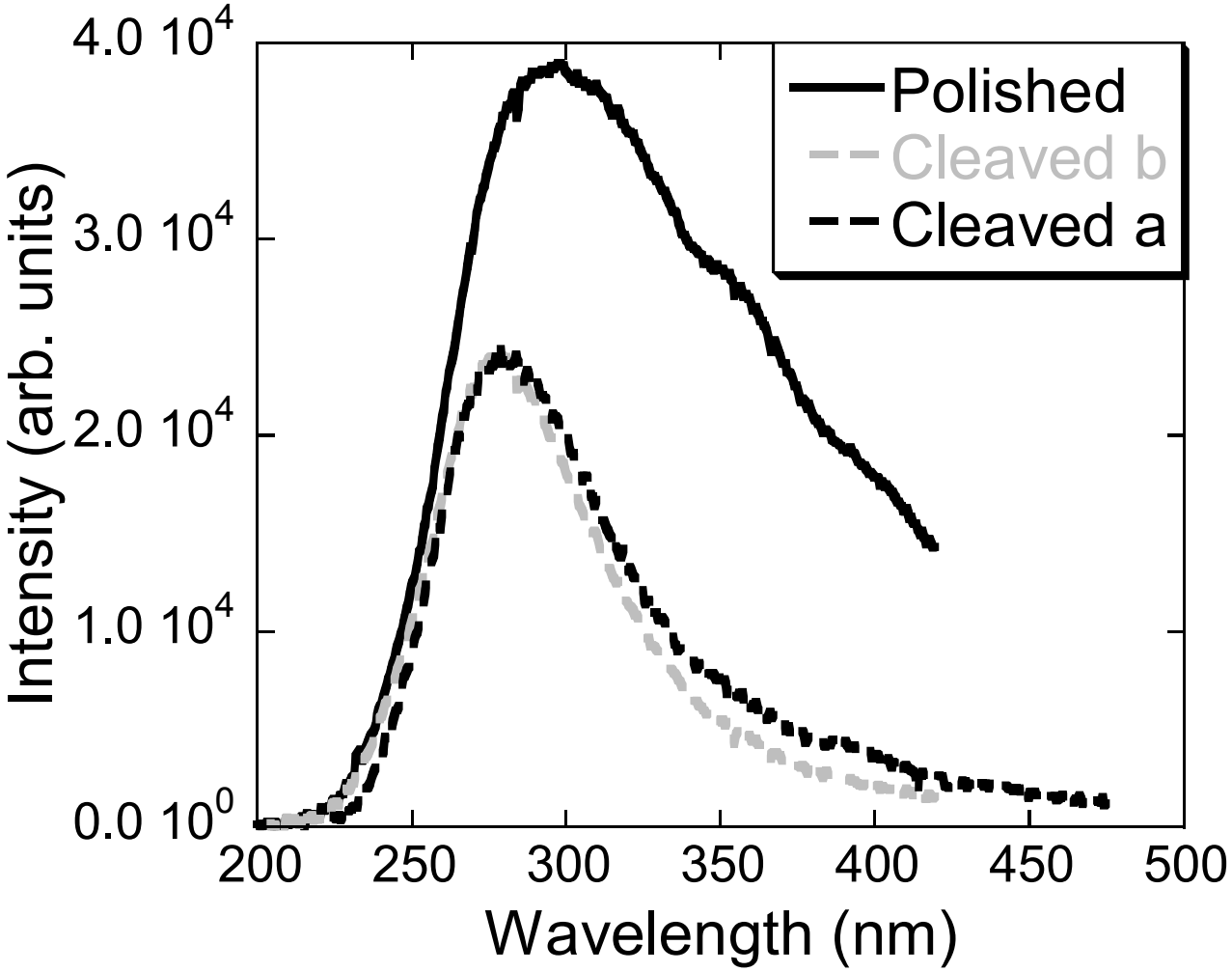

Figure 5(b)

STE luminescence comparing
cleaved and polished at 193 nm

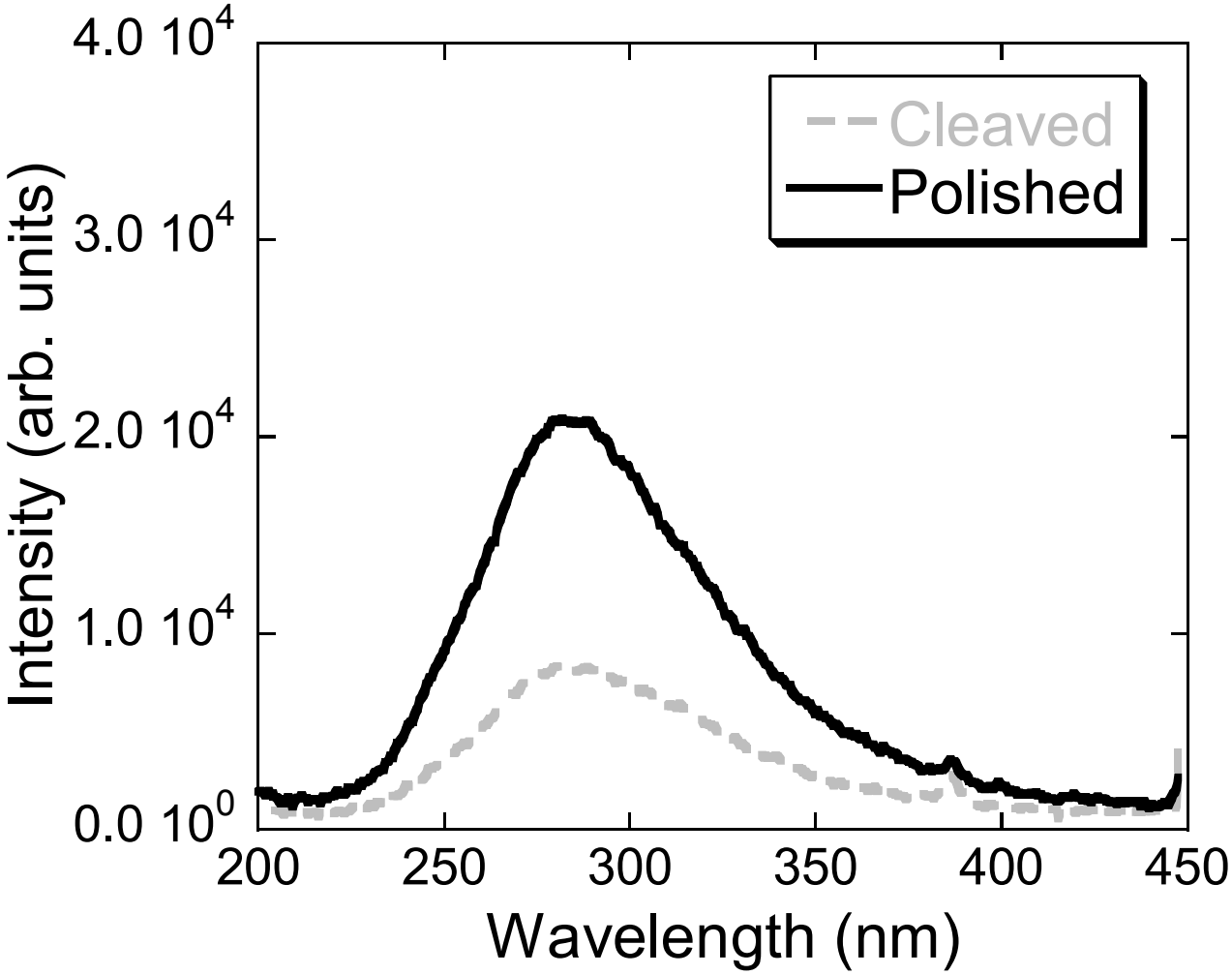

Figure 6

STE luminescence on cleave
surface treated with steel ball

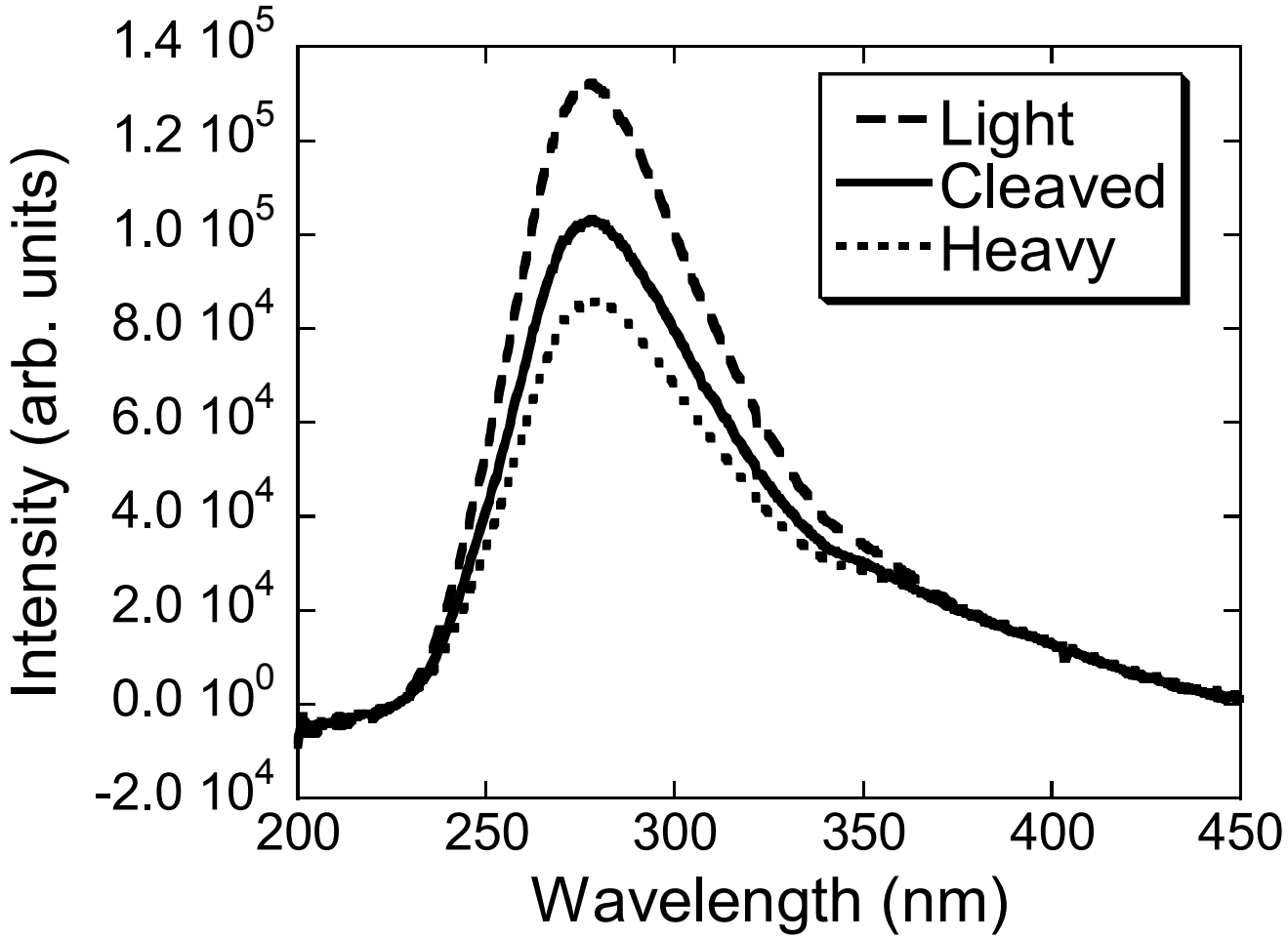

Figure 7

Integrated luminescence intensities for polished and electron irradiated samples

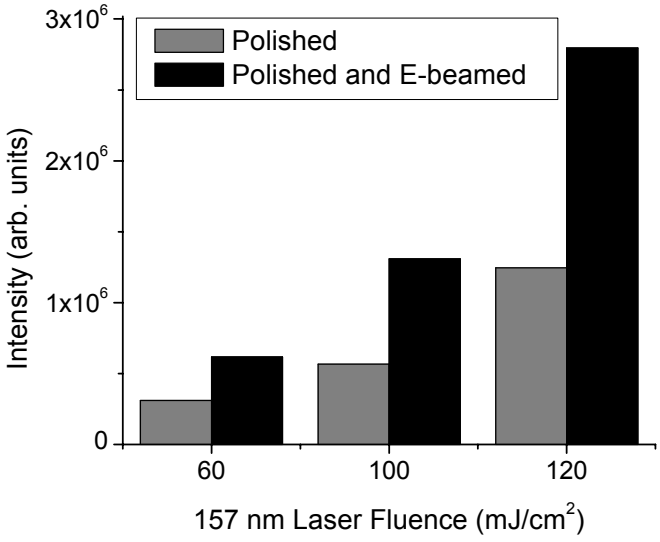

Figure 8

Average luminescence intensities
after various annealing treatments

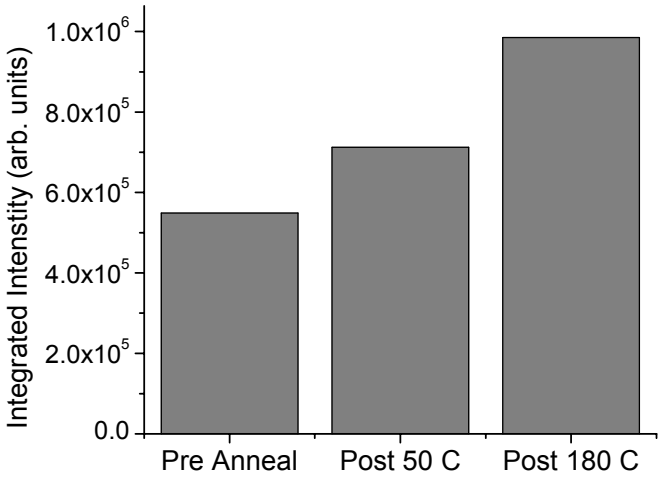

The formation of metallic nanoparticles in single crystal CaF_2 with 157 nm excimer laser irradiation

L. P. Cramer, S. C. Langford and J. T. Dickinson

Materials Science Program and Physics Department, Washington State University, Pullman, WA 99164-2814

Abstract

Single crystal calcium fluoride (CaF_2) is a material currently being used in vacuum ultraviolet optical components. Unfortunately, all metal halides have a tendency to form defects under energetic particle and laser irradiation, and these defects can degrade optical properties. Here we examine the consequences of exposing CaF_2 to 157 nm excimer laser radiation, and show that at fluences of ~1 J/cm^2, several tens of thousands of pulses will cause visible material coloration. Absorption spectra of the laser-irradiated area indicate the formation of metallic nanoparticles and are consistent with nanoparticle formation by other forms of energetic radiation. Metallic nanoparticle formation shows dependence on the temperature and has a maximum rate of formation at temperatures near 50ºC. In addition, a fluence-dependent transient absorption was observed, which competes with the self-trapped exciton luminescence. Metallic nanoparticle formation is not expected to be an important process at significantly lower fluences. Although it does appear evident that defect production is clearly a serious issue for use of CaF_2 at 157 nm, and may limit the lifetime of optical components in practical applications.

Introduction

CaF_2 is an important material for vacuum-ultraviolet (VUV) optical components. It is currently employed as an optical material for 193 nm lithography and is a leading candidate for use at 157 nm. Even though high purity single crystal CaF_2 is transparent at wavelengths as low as 130 nm, moderate laser intensities at 157 nm can generate defects.

The aggregation of point defects produced by energetic radiation ultimately yields metallic nanoparticles, or calcium colloids. For instance, modest electron doses (< 5 mC/cm^2 at 2 keV) form quasi-organized arrays of ~20 nm particles in the near-surface region.[1-4] These particles absorb strongly in the 550 to 600 nm region, with dependence on the particle size. It has been shown that laser-bleaching treatments can significantly alter the size and density of metallic nanoparticles produced by electron irradiation in CaF_2.[4,5]

In previous work, it was found that electron-induced metallic nanoparticles (a.k.a. calcium colloids) in the near surface region can be bleached with 157 nm at relatively low fluences (10 mJ/cm^2).[5] At low fluences there are relatively few two-photon absorption events that happen, but exposure at higher fluences (~1 J/cm^2) results in a greater probability of two-photon absorption occurrence. Two-photon absorption at 157 nm (7.9 eV) in CaF_2 can result in exciton formation, since two 157 nm photons have energy above the ~11 eV bandgap of CaF_2.[6,7] These excitons can then decay, resulting in defects such as F- and H-centers, since in CaF_2 the relaxed self-trapped excitons (STE) atomic positions are close to those of a nearest neighbor F-H pair.[8] F- and H-centers are created when a fluorine atom (leaving a trapped electron at the vacant fluorine site forming the F-center), moves from the fluorine lattice site to an adjacent interstitial site (forming a F_2^- molecule at a fluorine site, an H-center). The fluences utilized in this

study were high enough to assure two-photon events, but below the observed plume threshold at 157 nm, which was determined for our samples to be near 8 J/cm^2.

Absorption at 157 nm should be quite low since CaF_2 is relatively transparent to wavelengths of 130 nm. However, absorption is observed that is transient at relatively high fluences (> 1 J/cm^2), which reduced the number of two-photon events resulting from self-trapped exciton (STE) luminescence. Transient absorption related to STE has been observed in some alkali halides and has been related to hole transitions.[9] However, the reported transient absorption lifetimes are on the order of microseconds where in this study the transient absorptions appear to last for milliseconds.

In this work, it is shown that metallic nanoparticles are produced during irradiation with 157 nm excimer laser light at modest energy densities. The metallic nanoparticles size distributions appear to be limited due to the interaction with the bleaching quality of the 157 nm light. Thermal conditions have a fairly strong effect on the rate of metallic nanoparticle growth during laser irradiation. By investigating the factors that lead to metallic nanoparticle formation with laser irradiation, it may be possible to avoid conditions that result in optical failure.

Experiment

Vacuum-ultraviolet (VUV) grade CaF_2 from Korth Kristalle GmbH was cleaved in air along the (111) plane into 0.2 cm × 1 cm diameter disks. Samples were either used as cleaved or as polished with diamond paste in methanol. Additional samples were cleaved from a VUV grade CaF_2 lens (CVI) for comparison. Experiments were carried out at pressures less than 1×10^{-7} Pa or in dry nitrogen at atmospheric pressure. Radiation at 157 nm was provided by a Lambda Physik LPF 200 F_2 laser (20 ns pulse). Several hours (typically 2-3) of laser exposure of ~1 J/cm^2 at 20 Hz were required to achieve visible coloration.

The extent of metallic nanoparticle production during 157 nm irradiation was determined by monitoring the transmission of a diode laser at 532 nm, as shown in Fig. 1. After various treatments in vacuum, the samples were removed to air and absorption spectra were acquired with a Perkin Elmer Lambda 900 UV/Vis/NIR spectrometer.

A Roper Scientific PI-Max Intensified CCD imaged the signal from a Model 82-479 Thermo Jarrel Ash Spectrometer with a 300 lines/mm grating blazed at 400 nm. The spectrometer was equipped with an optical fiber to bring the light from the sample to the spectrometer. The intensifier had an exposure (gate-window) of 5 μs, which started immediately after the laser pulse. Typical spectra were averaged over 1000 laser pulses acquired at a repetition rate of 20 Hz.

Transmission experiments were conducted in dry nitrogen using a Star Tech Instruments model CF20C energy probe with an RS500 electronic switch for 157 nm in a single beam configuration. Power measurements were obtained before each run to monitor the changes in energy.

Results

The absorption spectra in Fig. 2a show the findings of two treatments resulting in the formation of metallic nanoparticles in CaF_2 (~1 C/cm^2 electron dosed and 2-3 hours 157 nm irradiated). A digital image of a 157 nm excimer laser darkened sample is seen in Fig. 2b. The dark rectangular shaped area in the middle of the image is the beam spot. The laser-treated area visibly shows coloration uniformly throughout the bulk. In both polished and cleaved samples, the distribution appears to be throughout the bulk after several hours of similar treatments. Virtually identical spectra are observed with similar exposure on VUV grade lens material (from CVI) and are not illustrated. The absorption peak at ~550 nm can be attributed to the formation of metallic nanoparticles.[10] The shoulder near 375 nm appears in both spectra and is attributed to isolated F-centers. The

shoulder may also contain the H-centers at 295 nm but is not readily apparent in either spectrum.[8] The width of the absorption peak is related to the distribution of the metallic nanoparticles size, and the combination of the peak position and distribution is related to the mean particle size, assuming a spherical particle.[1] The narrow distribution for the 157 nm induced metallic nanoparticles indicates that there is a limited size distribution. Compared to those induced by low-energy electrons, the peak position for the 157 nm spectra is consistent with smaller metallic nanoparticles .

Metallic nanoparticle formation in CaF_2 depends strongly on temperature, and at temperatures above room temperature (25°C) the defect mobility increases.[11,12] This assists in the formation of larger metallic nanoparticles.[13] Since the metallic nanoparticles scatter light (Mie scattering) over the range of 500 to 650 nm (the observed absorption band), it was possible to use a diode laser at 532 nm in transmission (see Fig. 1) in the 157 nm irradiation area to monitor the growth *in situ*. Figure 3 shows that there is a change with respect to time in transmission at 532 nm for all three studied temperatures. The overall change is slowest at 25ºC, most rapid at 50ºC, and slows again at 70ºC. If the assumption is that the laser was simply thermally assisting growth, the metallic nanoparticle formation should increase with increasing temperature.[13] However, this was not observed, indicating something else was affecting the metallic nanoparticle formation.

The rate at which the metallic nanoparticles form is dependent on temperature and the change in optical transmission may be fit by an exponential decay function such as:

$$T = T_0 - \Delta T(1 - e^{(-t/\tau)}) \qquad (1)$$

where T_0 is the initial transmission, ΔT is the change in transmission, t is the time in minutes and τ is the time constant for decay. Samples heated to 25°C and 70°C show a

time constant for decay of 31 and 26 minutes respectively. However, samples heated to 50°C resulted in a much faster time constant of 12 minutes.

Absorption spectra taken for the samples in Fig. 3, after laser irradiation at the given temperature, are shown in Fig. 4. A polished blank is shown for comparison. As expected from previous results (Fig. 3), the sample irradiated at 50ºC shows significantly greater absorption than the samples irradiated at 25°C and 70°C. The observed baseline shift is possibly related to disruption in the lattice due to the numbers of metallic nanoparticles.

Figure 5 shows the single beam transmission experimental set up for results presented in Figs. 6 and 7. The dry nitrogen is used to eliminate atmospheric oxygen and water which strongly absorb 157 nm light.

Figure 6 shows the change in transmission at 157 nm with fluence in a single beam configuration. Each point is an average of 100 pulses (laser running at 20 Hz) of 157 nm taken immediately following the previous point. The fluence is increasing in the data labeled up. The end point (next to the small downward arrow) in the data shows that by staying at the same fluence, the 157 nm transmission decreases with the increased number of pulses. The reduction of fluence (down) shows a slow recovery to near initial transmission. For this sample the damage threshold was determined to be ~ 9 J/cm^2 on a nearby region of the surface, therefore the cutoff is set below that value to avoid visible surface damage.

Figure 7 is the change in STE luminescence observed simutanously with the transmission results presented in Fig. 6. The decreased in transmission coincides with the decreasing STE luminescence production. It appears that the number of photons available for radiatively decaying excitons resulting in STE luminescence is reduced.

Discussion

Two-photon absorption events create self-trapped excitons in CaF_2 by promoting electrons from the valence band to the conduction band, which is an ~11 eV transition in CaF_2.[6,7] It has been discussed in literature that forming STEs with 157 nm (7.9 eV) would require a two-photon process.[14] In single crystal CaF_2, the relaxed STE atomic positions are close to those of a nearest neighbor F-H pair.[8] F- and H-centers are created when a fluorine atom moves from the fluorine lattice site to an adjacent interstitial site.

Metallic nanoparticle formation due to electron irradiation has been well defined in other works.[1,3] The metallic nanoparticles are confined to the near-surface region due to the short penetration depth of keV electrons. The electrons form STEs, some of which decay non-radiatively into F-H pair, resulting in a large number of point defects. The defects can move about due to thermal diffusion, which can result in defect aggregations leading to metallic nanoparticles formations.[8,11-13] The penetration depth for electrons is limited by particle interaction with the crystal lattice and has been determined theoretically to be ~50 nm and experimentally to be ~60 nm with some question as to secondary electron penetration depth.[15] Single crystal CaF_2 is relatively transparent (~85% transmission at 157 nm), which allows for sufficient photon densities in the bulk, and results in a uniform two-photon absorption. The steps to metallic nanoparticle formation in CaF_2 is thought to start with a two-photon absorption, which results in a STE. The STE can decay non-radiatively into F- and H- centers, and with sufficient thermal energy the F-centers are able to aggregate, leading to metallic nanoparticles. It appears that metallic nanoparticles formed in CaF_2 by 157 nm laser exposure are very similar to the metallic nanoparticles formed by electron irradiation.

The temperature dependence found with the coloration experiments presented here aligns nicely with other published works with regard to the thermal energy needed to

allow for mobile F- and H-centers in CaF_2.[12] The creation of metallic nanoparticles depends on the aggregation of F-centers to form neutral calcium metal. Annealing additively colored (calcium enriched) CaF_2 has shown to increase metallic nanoparticle size with increasing temperatures.[13] By simply heating the sample, the defects will aggregate, forming larger and larger metallic nanoparticles with time and temperature.[13] In previous work it has been shown that 157 nm irradiation can bleach electron induced metallic nanoparticles formations, but there is a size dependence on the wavelengths used for bleaching.[5] It can be inferred from these findings that adding excessive thermal energy (greater than 50ºC) results in larger particles, which are more efficiently bleached at 157 nm, thus reducing the metallic nanoparticle growth.

Transient absorption has been observed that decreases the transmitted energy, thereby reducing the production of STE luminescence (see Fig. 7). The results seen in Fig. 6 show how the transmission decreases with increasing fluence, and recovers with decreasing fluence. The highest fluence achieved in Fig. 6 (next to the small downward arrow) shows that by staying at the same fluence for an additional 100 pulses there is an observed reduction in transmission. At the related points in Fig. 7, there is a corresponding decrease in STE luminescence (next to the small downward arrow). This indicates that there is an additional absorption event beyond the two-photon absorption, producing the STE luminescence.[16] The absorption seems to be transient as the transmission and the STE luminescence both recover with decreasing fluences. The transient absorption at increasing fluences reduces the incident fluence, which in turn reduces the potential for STE luminescence (see Fig. 7).

Defect formation leads to a relaxation of the perfect lattice in materials such as KI, KCl, KBr and RbCl, which have all shown an associated absorption band related to the F-centers.[17] In alkali halides there is an observed absorption band (β band) near the edge of the fundamental absorption band in additively colored crystals containing primarily F-centers, that is not observed in uncolored crystals. The β band scales

proportionally with the F-centers. In addition to the β band, there is an additional absorption band (α band) observed which is related to the halogen-ion vacancy. CaF_2 could have a similar absorption band related to the halogen-ion vacancy.

As the F-centers aggregate, the calcium ions reduce to become metallic calcium. The trapped electron originally at an F-center is captured by the calcium ion and leaves a vacant halogen site. There would be a period of induced stress to the lattice as the calcium starts forming its own lattice and leaves an absorbing site in the band gap.

Defects, such as F- and H-centers, create a stress gradient in the surrounding lattice to accommodate the change in the perfect lattice. This can lead to a stress gradient in the lattice allowing for additional absorption sites (a probable origin for the α and β bands). Additionally, the calcium metal volume is 6% larger than that of the calcium ions in CaF_2. The metallic nanoparticles are therefore in compression and the surrounding lattice in tension, which can also result in changes in absorption.

At the high fluences employed in this work, the lifetime of CaF_2 optics at 157 nm is severely limited by metallic nanoparticle formation. This would likely rule out the commercial use of CaF_2 in micromachining applications requiring fluences on the order of 1 J/cm^2. At the much lower fluences employed in lithography, defect production by two-photon absorption will be reduced. Furthermore, the formation of metallic nanoparticles will be severely reduced. As noted above, fluences on the order of 10 mJ/cm^2 can be employed to bleach previously colored material. At such low fluences, the defect density after long exposures may reflect a balance between two-photon defect production and one-photon bleaching processes. Given the high optical quality required for lithographic applications, attention to defect production processes during prolonged irradiation will be critical.

Conclusion

It has been shown that CaF_2 irradiated with moderate levels of 157 nm laser light forms what appear to be metallic nanoparticles. Irradiation with 157 nm laser light by a two-photon process results in F- and H-centers with defect aggregations leading to metallic nanoparticle formation. Heating affects the F- and H-centers mobility, which enhances metallic nanoparticle growth. The bleaching of larger particles with 157 nm laser light reduces the potential thermally assisted growth, and results in a fairly uniform metallic nanoparticle distribution throughout the bulk.

Long-term exposure to high intensity 157 nm laser light that induces metallic nanoparticle formation in CaF_2 is a concern for industrial applications such as lithography systems. Even at low fluences, there is still the probability of two-photon absorption, which under prolonged exposure could result in metallic nanoparticle formation. Hopefully, by considering the results presented here, the lifetime of CaF_2 as an optical component can be enhanced, and systems will be designed to avoid the thermal and fluence settings that lead to reduced transmission.

Acknowledgements

Funding partially provided by the United States Department of Energy under contract DE-FG03-98ER14864.

References

[1] R. Bennewitz, C. Günther, M. Reichling, E. Matthias, S. Vijayalakshmi, A. V. Barnes, and N. H. Tolk, Appl. Phys. Lett. **66,** 320-322 (1995).

[2] V. S. Teodorescu, L. C. Nistor, and J. V. Landuyt, in *Defects in Insulating Materials*, edited by G. E. Matthews and R. T. Williams (Trans Tech, Zeurich, Switzerland, 1997), p. 671-674.

[3] M. Huisinga, N. Bouchaala, R. Bennewitz, E. A. Kotomin, M. Reichling, V. N. Kuzovkov, and W. v. Niessen, Nuclear Instruments and Methods in Physics Research B **141,** 79-84 (1998).

[4] J. B. LeBret, L. P. Cramer, M. G. Norton, and J. T. Dickinson, Submitted to Journal of Applied Physics (2004).

[5] L. P. Cramer, B. Schubert, P. Petite, S. C. Langford, and J. T. Dickinson, Submitted to Journal of Applied Physics (2004).

[6] R. A. Heaton and C. C. Lin, Physical Review B **22,** 3629-3638 (1980).

[7] R. A. Evarestov, I. V. Murin, and A. V. Petrov, Journal of Physics: Condensed Matter **1,** 6603-6609 (1989).

[8] K. S. Song and R. T. Williams, *Self-Trapped Excitons Second Edition*, Vol. 105 (Springer, Berlin, 1996).

[9] K. Edamatsu, M. Sumita, S. Hirota, and M. Hirai, Physical Review B **47,** 6747-6750 (1993).

[10] E. Stenzel, N. Bouchaala, S. Gogoll, T. Kotzbucher, M. Reichling, and E. Matthias, Mater. Sci. Forum **239-241,** 591-594 (1997).

[11] L. W. Hobbs, Journal De Physique **37,** 3-25 (1976).

[12] M. L. Sanjuan, P. B. Oliete, and V. M. Orera, Journal of Physics: Condensed Matter **6,** 9647-9657 (1994).

[13] V. M. Orera and E. Alcalá, Phys. Stat. Sol. **38,** 621-627 (1976).

[14] C. Görling, U. Leinhos, and K. Mann, Optics Communications **216,** 369-378 (2003).

[15] L. P. Cramer, F. Stevens, and J. T. Dickinson, to be submitted (2004).

[16] L. P. Cramer, T. D. Cumby, J. A. Leraas, S. C. Langford, and J. T. Dickinson, To be submitted (2004).

[17] F. Seitz, Rev. Mod. Phys. **26,** 7-94 (1954).

Figure Captions

Figure 1

Fig. 1 Apparatus for monitoring 532 nm transmission changes during 157 nm laser irradiation.

Figure 2

Fig. 2 a) Absorption spectra of electron irradiated (top) and 157 nm irradiated (bottom) CaF_2. The peaks at 550 nm are due to absorption by metallic nanoparticles. Isolated F-centers are responsible for the shoulders near 375 nm. b) Digital image of a cleaved CaF_2 sample that has been 157 nm laser irradiated at ~1 J/cm^2 for 2-3 hours at 20 Hz.

Figure 3

Fig. 3 Transmission at 532 nm versus time during 157 nm irradiation at three sample temperatures. Twenty 1 J/cm^2 pulses were incident on the sample per second.

Figure 4

Fig. 4 Absorption spectra of CaF_2 disks after 157 nm exposure at three temperatures taken in air at room temperature after samples have been removed from the vacuum system. (These samples are the same as in Fig. 3).

Figure 5

Fig. 5 Experimental set up for single beam transmission at 157 nm. Sample was moved in and out of the beam without opening the tube to atmosphere.

Figure 6

Fig. 6 Change in transmission of CaF_2 with increasing fluence followed by deceasing fluence. Each point is an average of 100 pulses of 157 nm laser light divided by the average laser energy recorded before and after the experiment.

Figure 7

Fig. 7 The average integrated STE luminescence corresponding to the data reported in Fig. 5.

Figure 1

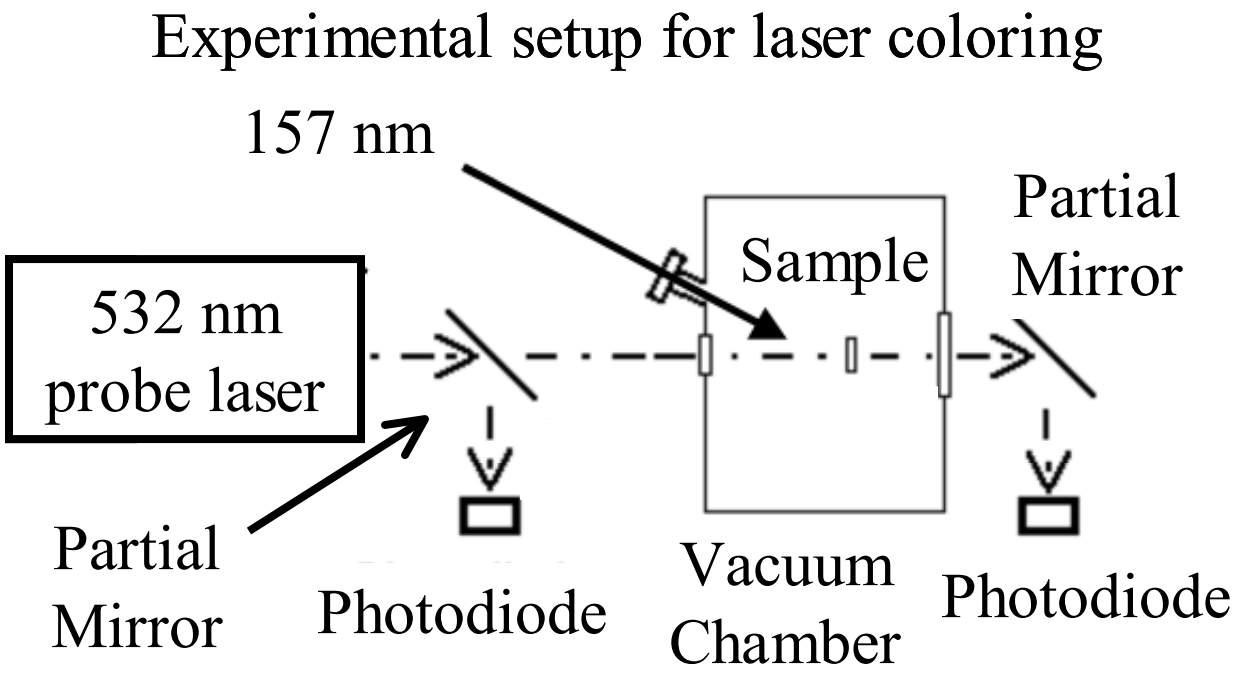
Experimental setup for laser coloring
157 nm
Partial
Mirror
Sample
532 nm
probe laser
Partial
Mirror
Photodiode
Vacuum
Chamber
Photodiode

Figure 2(a)

Metallic nanoparticles grown by different excitations

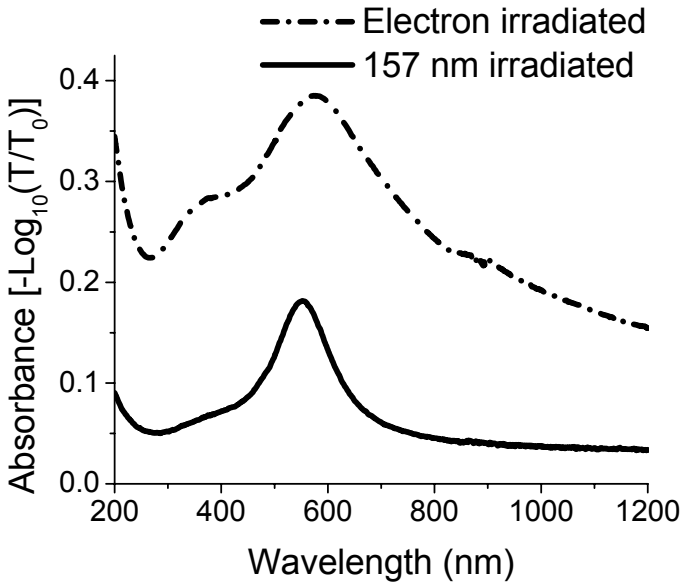

Figure 2(b)

Digital image of 157 nm
laser darkened region

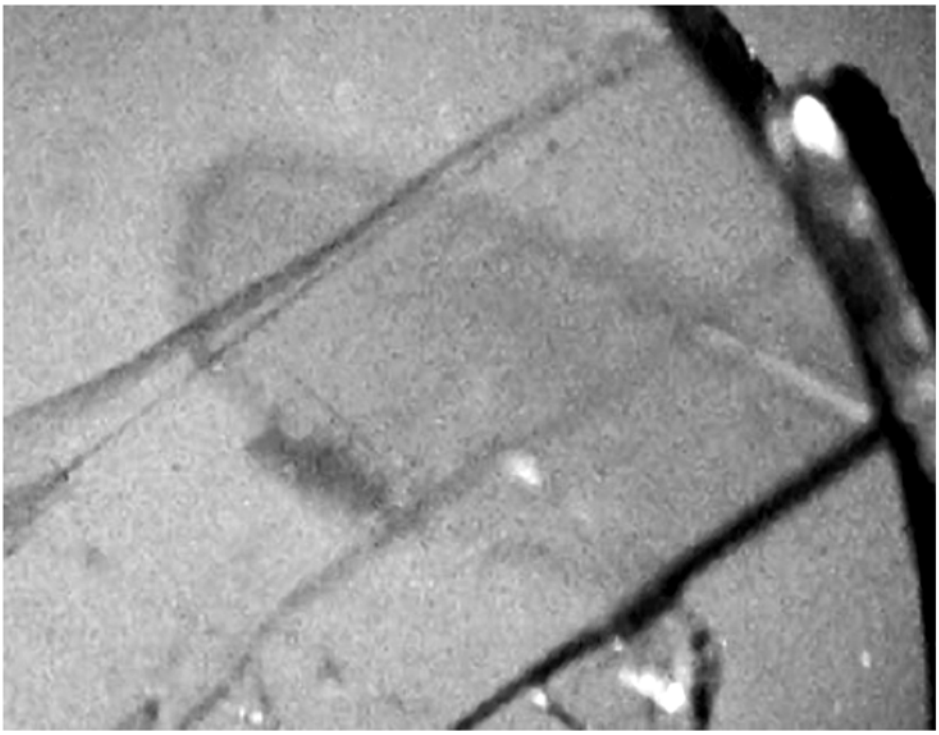

Figure 3

Temperature dependence on nanoparticle formation

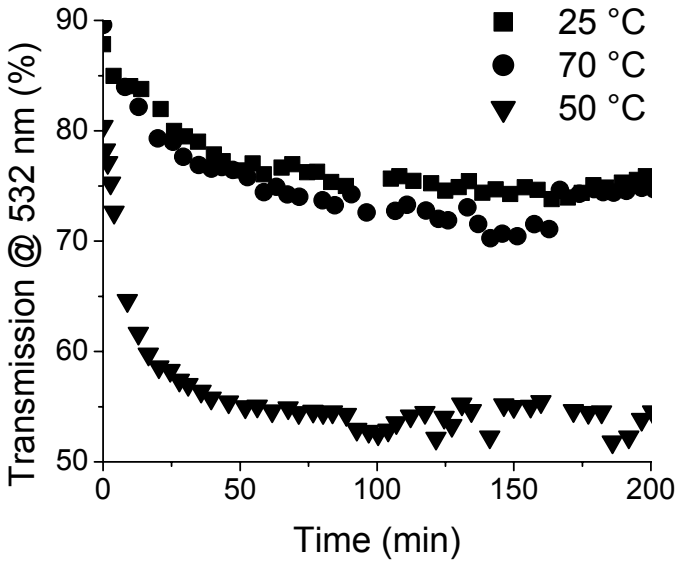

Figure 4

Absorption spectrum for nanoparticle growth at different temperatures

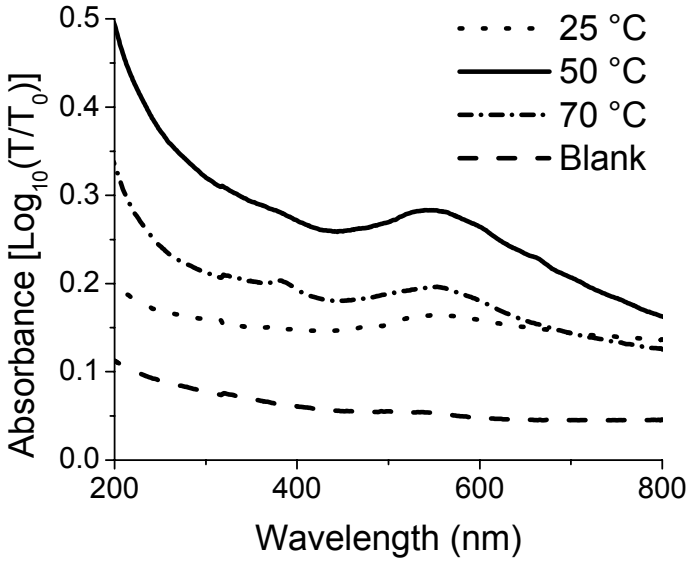

Figure 5

Single beam experimental setup

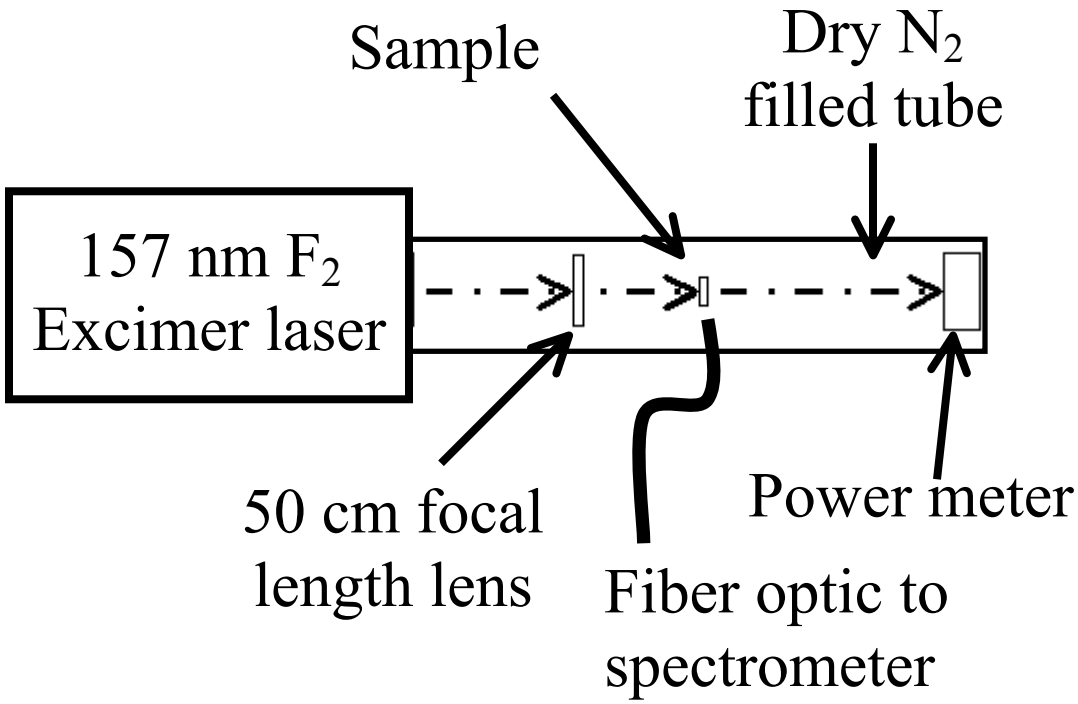

Figure 6

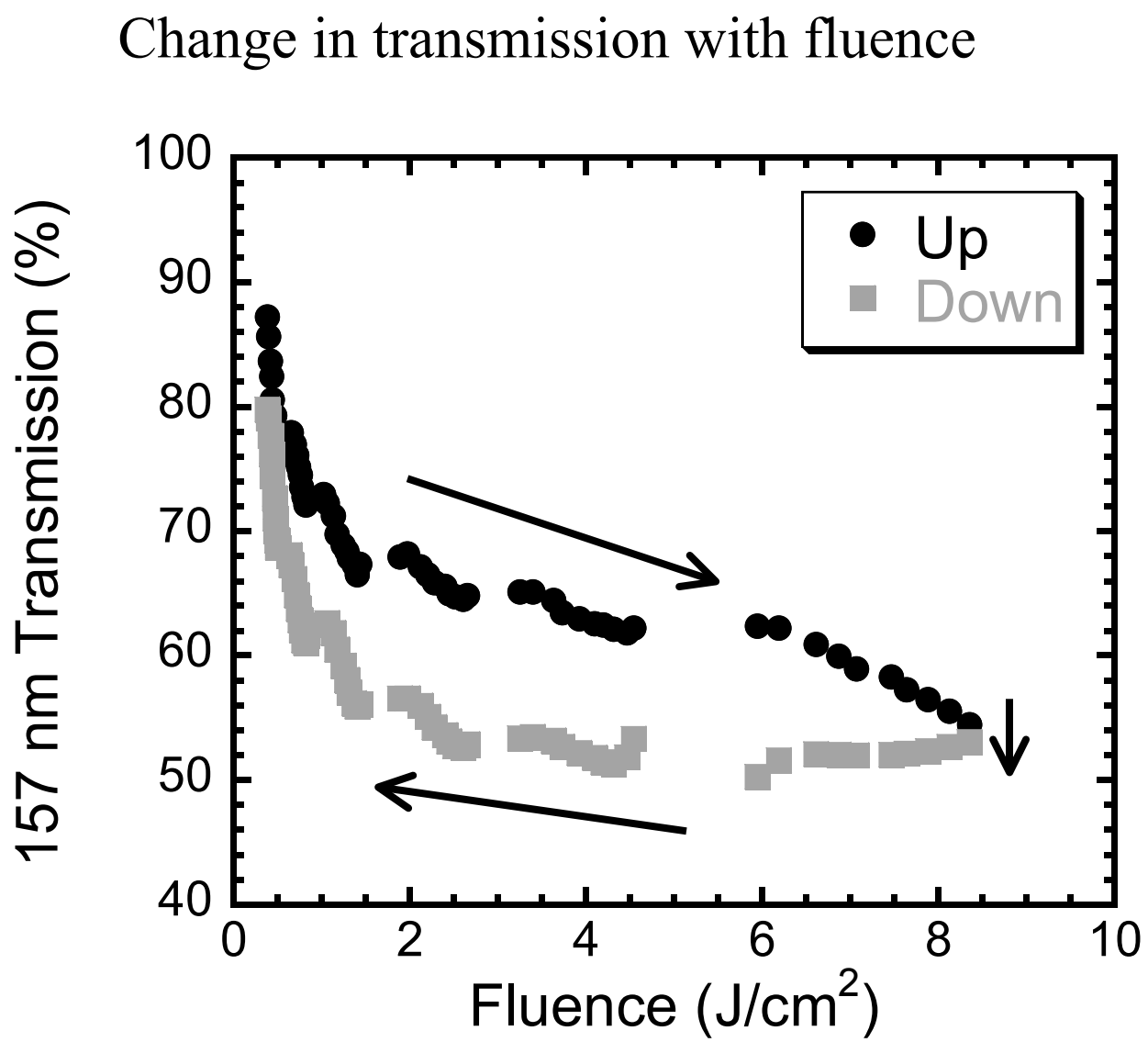
Change in transmission with fluence
157 nm Transmission (%)
100
90
80
70
60
50
40
0
2
4
6
8
10
Fluence (J/cm2)
Up
Down

Figure 7

Change in luminescence intensity with fluence

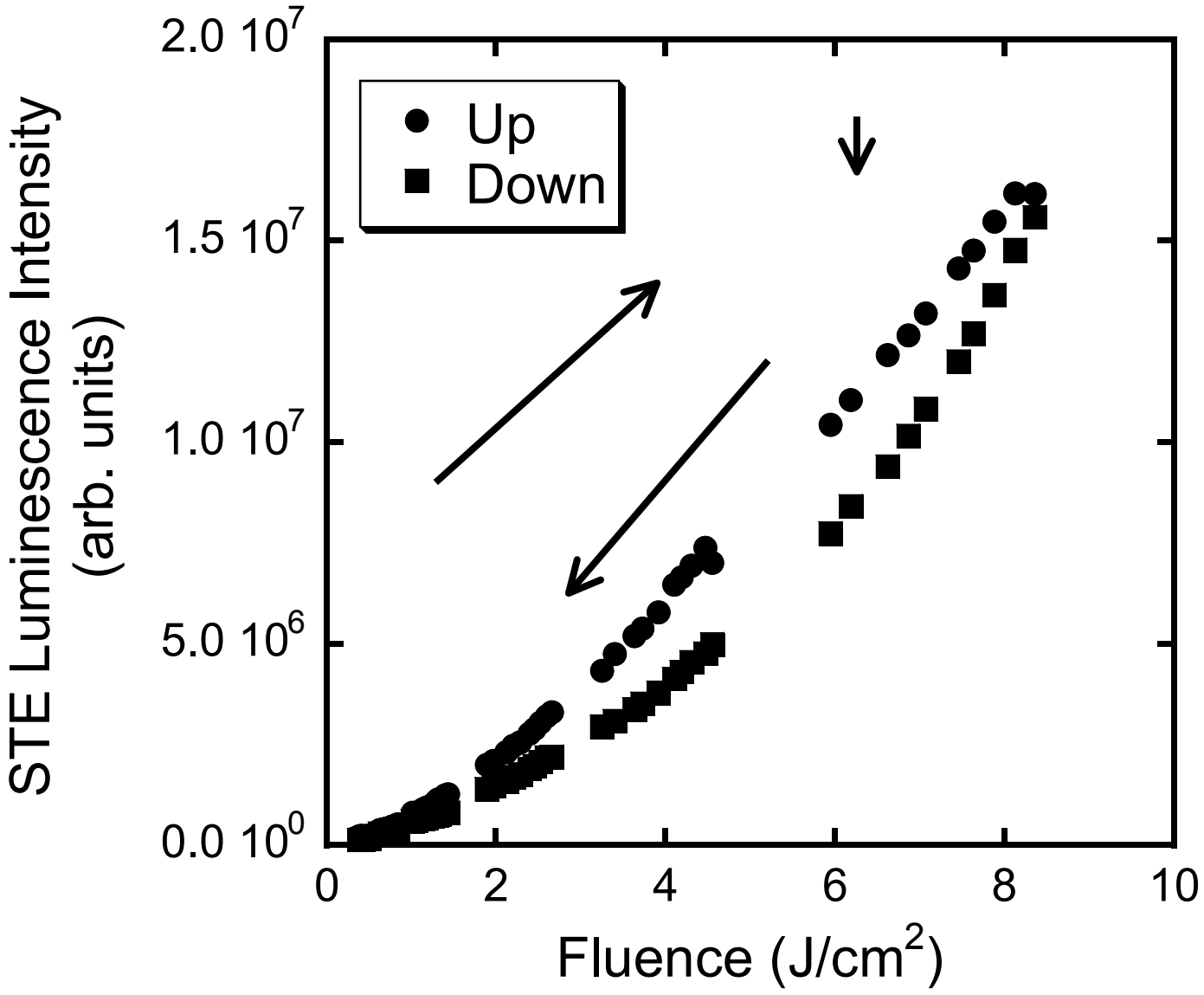

Chemical etching of defects induced by 2 keV electrons and 157 nm photons in single crystal CaF_2

L. P. Cramer, F. Stevens and J. T. Dickinson

Materials Science Program and Physics Department, Washington State University, Pullman, WA 99164-2814

Single crystal calcium fluoride (CaF_2) is an insulating material with good ultraviolet transmission. Epitaxial grown CaF_2 is being considered as a mask or dielectric in layered semiconductor devices. Here we examine the consequences of exposing single crystal CaF_2 to 2 keV electrons and 157 nm excimer laser light. By masking areas on the surface of CaF_2 during irradiation, acid etching can be used to remove exposed defect-rich areas, while leaving the desired structure. Monitoring the etching process with atomic force microscopy allows for the estimation of relative defect density and defect depth. It was found that 2 keV electrons caused disruption to the crystal lattice as deep as 600 nm and also appeared to cause defect aggregations that crossed the (111) plane. 157 nm laser irradiation caused significant crystal damage only to a depth of about 100 nm, and linear defect aggregations were not observed.

Introduction

Calcium fluoride (CaF_2) can be grown epitaxially on silicon and has a high dielectric constant. This makes it an attractive material, both as a lithographic mask, and as a dielectric for wafer fabrication.[1] CaF_2 is a robust material, but by selectively introducing defects, the surface can be made to preferentially etch and form controlled surface structures. CaF_2 transmits ultraviolet light down to 130 nm, making it an attractive optical material for short-wavelength optical lithography.[2] The ability to shape the material into controlled patterns could lead to a variety of new applications.

Prior studies have successfully used electrons to expose epitaxially grown CaF_2 layers for lithography.[1,3-5] The electrons introduce defects into the crystal structure by forming F- and H-centers. F-centers are fluorine vacancies that trap an electron, and H-centers are F_2^- molecules at a fluorine site (the additional fluorine is positioned in an adjacent interstitial site).[6] As the F-centers aggregate, the calcium ions are reduced to calcium metal forming metallic nanoparticles.[7,8] The exposed surface area is loaded with defects (nanoparticles and point defects), which can be removed by dissolution in water or dilute acid.

In single crystal CaF_2, defects created by exposing the material to either electrons or prolonged vacuum ultraviolet (VUV) light cause the normally transparent crystalline material to develop a purplish hue, which is caused by light scattering from formations of metallic nanoparticles (calcium colloids).[9,10] It has been found that VUV laser (157 nm) light induces metallic nanoparticles that have similar optical properties to metallic nanoparticles created with electron irradiation.[11]

While lithographic pattering of CaF_2 has been demonstrated in thin films (<100 nm), the distributions of the induced defects have not been examined. Imaging the surface as defect-rich regions are chemically removed will allow for a greater understanding in how single crystal CaF_2 can form defects. This will aid in avoiding

defect formation in CaF_2 optics and in promoting controlled defects in CaF_2 layers to improve lithographic contrast.

Experiment

Vacuum-ultraviolet (VUV) grade single crystal CaF_2 was purchased from Korth Kristalle GmbH and was cleaved in air along the (111) plane into 0.2 cm × 1 cm diameter disks. Some samples were also polished using diamond paste (0.25 μm) with methanol in air. Experiments were also performed on samples cleaved from a VUV grade CaF_2 lens (CVI) for comparison. Samples were introduced into vacuum with a base pressure of ~1×10^{-7} Pa. An Auger electron gun was used to produce an electron beam of 2 keV (~100 μA with an area of ~0.3×0.4 cm^2). Electron exposure times were typically 1 to 120 min, resulting in electron doses of 0.05 to 6 C/cm^2. Surface patterning with electron irradiation was accomplished by covering samples with a 2000-mesh nickel screen, creating an array of 6 μm squares, which was detectable by optical microscopy and by AFM (atomic force microscopy).

A Lambda Physik 200LPF F_2 laser was used to produce 157 nm light (~20 ns pulse, ~1 J/cm^2). Laser exposure times of 2-3 hours at 20 Hz were required to produce visible coloration without surface damage.

Samples were etched by first exposing the samples to deionized water followed by hydrochloric acid (1M, 3.5%). The water dissolved oxides and hydroxides from the surface in under one minute (longer exposure to water had no additional effect). The HCl etching was done in two-minute intervals, and the sample was rinsed with deionized water, dried, and imaged with AFM after each etch interval.

AFM imaging was performed on a Digital Instruments Nanoscope III. On this instrument, the sample is mounted on the top of the piezoelectric scanner, which scans the sample under the cantilever. This geometry allows the cantilever and laser to be

removed to access the sample. As long as the sample is not moved when the cantilever and laser are replaced, the same area of the sample can be imaged again with an accuracy of a few microns. The tips used are square pyramids of CVD silicon nitride with a tip angle of 70°, nominal tip radius of curvature of 20-50 nm, and nominal force constant of 0.58 Nm^{-1}. All tips used were from the same wafer.

Volume changes were measured by using a Mathematica® program, which first flattened the background around the feature of interest (typically the 6 x 6 μm^2 areas resulting from the 2000-mesh nickel screen), and then identified the pixels in the selected area whose elevation above or below the surrounding plane was greater than the cutoff limit. The heights of the selected pixels were summed and multiplied by the area per pixel to obtain the total volume change.

Scanning electron microscope (SEM) images were taken at Environmental Molecular Sciences Laboratory User Facilities (Pacific Northwest National Laboratory) using the LEO 982 FESEM. This instrument has resolution of 1 nm at accelerating voltage of 30 kV and 4 nm at 1.0 kV. Samples were prepared with various treatments in our lab and transported in air before being coated with osmium for high resolution imaging.

Results

A CaF_2 surface after electron exposure though a 2000-mesh nickel screen is shown in Fig. 1a (6 C/cm^2 dose). The surface exposed to the electrons shows increased roughness, and an increase in volume. Once removed from the vacuum chamber, the calcium nanoparticles on the surface react with the ambient atmosphere to form CaO, $Ca(OH)_2$ and $CaCO_3$.[5,12] AFM images of individual 6 × 6 μm^2 irradiated areas were obtained, and the volume increase above the surrounding surface was measured from

images for various dosages and reported in Fig.2. The volume increase rose with electron exposure, and did not show any sign of saturation out to the highest dose examined.

Figure 1b shows the same area as 1a after treatment with deionized water (2 minute rinse), which removed the raised area resulting from electron irradiation. The same area after HCl etching is seen in Fig. 1c (2 minute HCl etch). Hydrochloric acid etches crystalline CaF_2 slowly, but etching is accelerated when defects are present.[13-15] Using HCl concentration of 1M (~3.5%) at room temperature resulted in a steady etching of areas exposed to the electrons, while unexposed areas etched much more slowly. The etching rate of unexposed CaF_2 was measured using gold, sputtered onto a cleaved surface, through the 2000-mesh nickel screen before HCl etching. The etch rate of the CaF_2 surface relative to the gold islands was too small to measure accurately, but was less than 1 nm/min.

CaF_2 irradiated with electrons forms a purplish coloration, which is caused by light scattering off the metallic nanoparticles.[16,17] Deionized water was found to remove the oxidized nanoparticles at the surface (seen in Fig. 1b). Electron-dosed CaF_2 placed in water lost the purplish color gradually, but still retained some color after four weeks. However, electron-dosed CaF_2 placed in 1M HCl quickly became colorless after only about ten minutes.

A series of samples were exposed to electrons through the 2000-mesh nickel screen for varying dosages, and etch rates were measured by atomic force microscopy with the results shown in Fig. 3. A higher electron dosage was found to increase etch rate and total etching depth. The image of the electron-irradiated area after etching, as seen in Fig. 4, shows overlapping equilateral triangles consistent with the symmetry of the CaF_2 (111) surface.

Samples etched with HCl showed a steady loss of material from electron-beam exposed areas. Samples exposed to lower doses of electrons (0.1-0.8 C/cm^2) showed linear etching at a constant rate of ~7 nm/min until about 200 nm had etched; after this

point the etch rate began to decrease. Samples exposed to longer electron doses (>1.2 C/cm^2) showed higher initial etch rates (~20-30 nm/min) that decreased exponentially with time. Although the maximum etch depth increased steadily, overall material removal proceeded in two stages. The beginning of the initial etching can be seen in Fig. 5 (0.1 C/cm^2 dose and etched for 6 minutes), which shows a few initial etch pits in the surface that will widen and merge to cover the entire area exposed to electrons. This area rapidly etched down to 50 to 70 nm, at which point general etching slowed. Once this first layer had etched, a second etch process was observed with small etch pits appearing in the exposed bottom of the initial etch pits, as can be seen in Fig. 6 (0.1 C/cm^2 dose and HCl etched for 20 minutes). Total etch depths of up to 600 nm were measured. Etch rates could not be followed indefinitely, because the pits grew laterally as well as down. They eventually merged, which destroyed the original surface from which depths were measured.

The formation of small pits on the surface (as seen in Fig. 5) could only be observed on samples with the low electron doses (< ~0.8 C/cm^2). On samples exposed to higher doses of electrons (> ~1.2 C/cm^2), the initial ~60 nm etching and the next generation of etch pits both proceeded rapidly, making the transition between the two stages of pit development less distinct. Etch depths could not be measured on samples exposed without the 2000-mesh nickel screen, due to the lack of a reference surface. However, samples exposed to electrons directly, showed qualitatively similar etching patterns, which suggests the presence of the screen does not alter the way the electrons interact with the material.

The surface of a later etching state was also imaged with SEM, and resulted in the image seen in Fig.7 (0.3 C/cm^2 dose and HCl etched for 2 minutes). Although the SEM image cannot be used to measure the depths of the etching pits, it does illustrate the surfaces preferentially etching in the electron irradiated areas (the same 6 □m^2 squares as seen with AFM).

Patterned laser irradiation with the 2000-mesh nickel screen could not be done, because the screen did not survive the high laser power necessary to achieve material coloration in a reasonable period of time. Samples were exposed to 157 nm laser irradiation by masking the edge of the beam, and the edge of the laser-exposed area was observed during etching. Imaging the surface after 157 nm laser irradiation (20 Hz, 2 hours at ~1 J/cm^2) did not conclusively show where the sample was irradiated (no topographical features were observed at below plume threshold, ~5 J/cm^2 on cleaved surfaces), but the surface changed after HCl etching (24 minutes) as can be seen in Fig. 8. The 157 nm laser-irradiated area etched with 1M HCl to a depth of ~100 nm, and showed the same pattern of overlapping triangles as was observed on electron-irradiated samples (Fig. 4). However, the small, deep etch pits seen on electron-irradiated samples were not observed on 157 nm laser-irradiated samples.

Discussion

Exposure to electrons is known to form F-H pairs in the CaF_2 lattice, which can allow F- center aggregation, and result in regions that form metallic nanoparticles.[18] CaF_2 irradiated with 157 nm laser of sufficient intensity (~1 J/cm^2) will also form defects (see Fig. 8).[11] On removal from vacuum, any calcium nanoparticles at or near the surface will rapidly react with the atmosphere to form oxides and hydroxides. The material seen in AFM images that rises above the CaF_2 surface appears to be largely calcium oxide and hydroxide.[5,12] This is demonstrated by its rapid removal by water (see Fig. 1), as both CaO and $Ca(OH)_2$ are much more water soluble than is CaF_2. XPS analyses of CaF_2 surfaces (not shown), after exposure to electron irradiation, were consistent with oxide and hydroxide. The underlying material has a high defect density, as shown by its rapid etching with HCl, but remains primarily CaF_2.[19] Identification of the underlying exposed material as CaF_2 is supported both by its lack of reaction with

water, and by the fact that HCl etching produces the equilateral triangle etch pits which are consistent with the symmetry of the CaF_2 (111) surface (Fig. 4).

Electron irradiation results in more than just point defects in CaF_2. Point defects should cause a steady decrease in etch rate, as defect density should decrease with depth. Observations (Fig. 3) match these predictions fairly well for samples exposed to larger doses of electrons (> ~1.2 C/cm^2). However, for samples exposed to lower doses, a different pattern is observed. Low-dose samples show an initial linear etch rate, which is insensitive to both electron irradiation exposure time and to etch depth. The etch rate slows at longer etch times and slows more rapidly on samples with lower electron doses.

Low-dose samples are initially well fit by a linear function:

$$Depth = At + B \quad (1)$$

where t is the acid etch time in minutes. At longer etch times, the low-dose samples are not linear, but show a steadily decreasing etch rate.

Samples exposed to larger doses of electrons show an initial rapid etch rate that decreases steadily with depth. The depth vs. etch time plots for these samples are well fit by the logarithmic function:

$$Depth = Cln(t) + D \quad (2)$$

We attempted to fit all curves by a combined log-linear function, where the linear function initially dominated, but gave way smoothly to the log function. The contribution of each function was determined by the factor e^{-Et} (decreasing) or $(1-e^{-Et})$ (increasing). The combined fitting function was:

$$Depth = [At + B] \times e^{-Et} + [Cln(t) + D] \times (1 - e^{-Et}) \quad (3)$$

Which reduces to:

$$Depth = Cln(t) + D + [At + B - Cln(t) - D]e^{-Et} \quad (4)$$

All the measured depth-time curves, from both low-exposure and high-exposure samples, were well fit ($R^2 \sim 0.98$) by this combined log-linear function (Eq. 4).

The combined linear and log functions are consistent with etching due to a combination of point defects, and by linear aggregations of defects induced by electron irradiation. At low electron doses, when the concentration of point defects is small, etching proceeds mainly at linear aggregations of defects. The etch rate does not depend on dose, and is constant for the depth of the linear aggregations. It then drops to a lower value once the linear aggregations are consumed. However, as the electron dose increases, more and more point defects accumulate in the crystal. At first, the point defects simply cause the material between linear aggregations to etch more rapidly. However, as the concentration of point defects accumulates, the etching due to point defects exceeds the etching due to linear aggregations of defects. Once this occurs, the etching follows the pattern expected for point defects; increasing with dose and decreasing steadily with etch depth. The observation that etching begins at a few places and proceeds downward and outward from these locations is also consistent with the presence of linear aggregations of defects. If only point defects were present, etching would be expected to be uniform.

Under our conditions of electron irradiation, point defects accumulate most rapidly in the top ~60 nm of CaF_2, which etches rapidly and completely even at lower electron doses. According to published theoretical results, the penetration depth for 2 keV electrons in CaF_2 is ~50 nm.[20] This is consistent with the thickness of the initial layer, which we observed to etch most rapidly, and which was most affected by increasing electron dose. The additional defects created deeper than ~50 nm are likely due to secondary electrons, which are lower in energy and can travel much farther through the crystal lattice before forming defects.[21] The energy required to create an F-H pair in CaF_2 is predicted to be 2.7 eV, [22] therefore a 2 keV electron can lose most of its energy and still be able to created defects. The linear aggregations observed are similar to those produced by high-energy ions. However, ion energies in the tens of MeV are

required to produce etchable line defects in CaF_2 and lithium fluoride, so it is not clear how such defects could be created by 2 keV electrons.[23,24]

The loss of coloration during HCl etching (usually after 5 to 10 minutes of etching) indicates that most of the metallic nanoparticles are in the upper regions of the crystal. Since the samples retained color in water for weeks, the loss of color is not due to water exposure alone, but is caused by the removal of colloid-enriched material by etching. Long electron irradiation exposure caused metallic nanoparticles to form deeper into the crystal, and a plot of electron irradiation time vs. nanoparticle depth (measured by etch depth which caused loss of coloration) produced a linear plot with slope of 2.3 nm/min and intercept of 70 nm. This indicates an initial metallic nanoparticle depth of 70 nm, which corresponds reasonably well to the theoretically predicted primary electron penetration depth of ~50 nm.

It is interesting to note that while metallic nanoparticles are limited to the upper 50 to 70 nm (or somewhat deeper for highest doses) of the crystal, other etchable defects extend much deeper (Fig. 3). For samples exposed to electrons for larger doses (1 C/cm^2) the metallic nanoparticle depth matches the depth of initial rapid etching (for low-dosed samples, the coloration was faint, making the loss of coloration difficult to measure accurately). The observation that etching of the first ~60 nm of CaF_2 was fairly rapid and complete suggests that electron lithography will be most successful for CaF_2 layers of 60 nm or less. Thicker layers will require larger doses and/or longer etching.

CaF_2 exposed to 157 nm laser light showed some differences from exposure to electrons. Laser exposure took much longer (typically 2-3 hours at 20 Hz at ~1 J/cm^2) to produce visible coloration. The coloration produced by laser irradiation also extended into the bulk of the crystal, rather than being localized at the surface, as is the case for electron-irradiated CaF_2. The surface of laser-irradiated CaF_2 samples showed great variability in AFM images, from no effect, to increasing amounts of surface roughening, to excavation of the surface due to plume formation.

Areas that were exposed to 157 nm laser light did etch in HCl, but only to a depth of about 100 nm. Electrons are absorbed near the surface of the material, while photons penetrate the entire sample. So it is perhaps surprising that the etch depth for 157 nm photon-irradiated CaF_2 is only ~100 nm, while electron beam-irradiated material etched to ~ 600 nm. In fact, it is possible that the etching of photon-irradiated CaF_2 is due to photon absorption at existing defects on the surface (which tended to roughened during laser irradiation), and that the overall bulk defect density due to laser exposure is simply too small to cause preferential etching.

Conclusion

Chemical etching, coupled with atomic force microscopy is an effective method of measuring the spatial distribution of defects introduced into a material. In CaF_2, controlled defect creation can be achieved with either low-energy electrons or VUV photons, which result in preferential etching of exposed areas. 2 keV electrons produced point defects in calcium fluoride as deep as 600 nm inside the crystal, and also produced linear aggregations of defects as imaged with AFM. At low electron doses, etching was primarily due to linear aggregations of defects. The depth of disruption to the crystal lattice was found to be much deeper than the predicted primary electron penetration.

The etching on 157 nm laser-irradiated surface did not appear to include the linear aggregations seen in the electron-irradiated samples. The etching of the 157 nm laser-irradiated surface showed that only the first 100 nm had enough defects to significantly increase dissolution rate. This suggests that laser-induced surface damage might be corrected by a bulk treatment to remove the damage before surface roughing appears.

Acknowledgements

Funding provided by the United States Department of Energy under contract DE-FG03-98ER14864, the National Science Foundation under Grants CMS-98-00230 and CMS-01-16196, and a subcontract with the University of Florida as part of a KDI-NSF Collaboration, Grant DMR-99-80015

References

[1] Y. Hirose, S. Horng, A. Kahn, C. Wrenn, and R. Pfeffer, J. Vac. Sci. Technol. A **10,** 960-964 (1992).

[2] R. S. Retherford, R. Sabia, and V. P. Sokira, Applied Surface Science **183,** 264-269 (2001).

[3] H. Hongo, T. Hattori, Y. Miyamoto, K. Furuya, T. Matsunuma, M. Watanabe, and M. Asada, Jpn. J. Appl. Phys. 1 **35,** 6342-6343 (1996).

[4] M. A. McCord and R. F. W. Pease, J. Vac. Sci. Technol. B **5,** 430-433 (1987).

[5] P. M. Mankiewich, H. G. Craighead, T. R. Harrison, and A. H. Dayem, Appl. Phys. Lett. **44,** 468-469 (1984).

[6] K. S. Song and R. T. Williams, *Self-Trapped Excitons Second Edition*, Vol. 105 (Springer, Berlin, 1996).

[7] C. L. Strecker, W. E. Moddeman, and J. T. Grant, Journal of Applied Physics **52,** 6921-6927 (1981).

[8] M. Reichling and R. Bennewitz, in *Defects in Insulating Materials—ICDIM96*, edited by G. E. Matthews and R. T. Williams (Trans Tech Publications, Zurich, 1997), p. 657.

[9] M. Huisinga, V. E. Puchin, and M. Reichling, Nuclear Instruments and Methods in Physics Research B **141,** 528-532 (1998).

[10] R. Bennewitz, C. Günther, M. Reichling, E. Matthias, S. Vijayalakshmi, A. V. Barnes, and N. H. Tolk, Appl. Phys. Lett. **66,** 320-322 (1995).

[11] L. P. Cramer, S. C. Langford, and J. T. Dickinson, to be submitted (2004).

[12] S. Baunack and A. Zehe, Surface Science **225,** 292-300 (1990).

[13] C. Maerky, J. L. Henshall, R. M. Hooper, and M.-O. Guillou, Journal of the European Ceramic Society **17,** 61-70 (1997).

[14] G. C. Jain, R. Krishnamoorthy, and T. S. Murty, Indian Journal of Pure and Applied Physics **19,** 1012-1014 (1981).

[15] A. R. Patel and C. C. Desai, Zeitschrift für Kristallographie **121,** 55-66 (1965).

[16] M. Reichling, Nuclear Instruments and Methods in Physics Research B **101,** 108-114 (1995).

[17] F. Beuneu and P. Vajda, Journal of Applied Physics **78,** 6989-6993 (1995).

[18] R. Bennewitz, D. Smith, and M. Reichling, Phys. Rev. B **59,** 8237-8246 (1999).

[19] J. B. LeBret, L. P. Cramer, M. G. Norton, and J. T. Dickinson, Submitted to Journal of Applied Physics (2004).

[20] R. Bennewitz, D. Smith, M. Reichling, E. Matthias, N. Itoh, and R. M. Wilson, Nuclear Instruments and Methods in Physics Research B **101,** 118-121 (1995).

[21] J. Cazaux, Journal of Electron Spectroscopy and Related Phenomena **105,** 155-185 (1999).

[22] N. Itoh and A. M. Stoneham, *Materials Modifications by Electronic Excitation* (Cambridge University Press, New York, 2001).

[23] M. Boccanfuso, A. Benyagoub, K. Schwartz, C. Trautmann, and M. Toulemonde, Nuclear Instruments and Methods in Physics Research B **191,** 301-305 (2002).

[24] C. Trautmann, K. Schwartz, and O. Geiss, Journal of Applied Physics **83,** 3560-3564 (1998).

Figure Captions

Figure 1

Fig. 1 AFM images of cleaved CaF_2 surfaces after electron irradiation (6 C/cm^2 dose) through 2000-mesh nickel screen. Each image is 50 × 50 μm, and all images have the same vertical scale. a) Sample after electron irradiation, showing raised areas where metallic nanoparticles have reacted to form oxide and hydroxide. b) Same sample after 2 minutes in water, calcium oxides and hydroxides have dissolved, e-beamed areas are now about the same height as surrounding surface, although rougher. c) Same sample after 2 minutes in 1M HCl, e-beam exposed areas have etched due to defects caused by irradiation.

Figure 2

Fig. 2 Volume of raised squares formed after electron irradiation though 2000-mesh nickel screen. Raised squares were about 6 × 6 μm^2.

Figure 3

Fig. 3 CaF_2 samples were electron-irradiated though 2000-mesh nickel screen and periodically measured by AFM while etching. Quantity measured is not "average depth" but rather "average maximum depth." On each sample, a number of local minima were measured, and the results averaged.

Figure 4

Fig. 4 CaF_2 after electron irradiation and HCl etching. The surface has etched into equilateral triangles consistent with the symmetry of the CaF_2 (111) cleavage surface. Image is 2 × 2 μm.

Figure 5

Fig. 5 CaF_2 irradiated with an 0.1 C/cm^2 electron dose through 2000-mesh nickel screen, and then etched in 1M HCl for 6 minutes. Image is 12 × 12 μm. Small pits can be seen in the area irradiated by electrons.

Figure 6

Fig. 6 CaF_2 irradiated with an 0.1 C/cm^2 electron dose through 2000-mesh nickel screen, and then etched in 1M HCl for 20 minutes in 2 minute intervals. Image is 17 × 17 μm. The irradiated area has etched evenly down to a depth of ~50 nm, and a second generation of pits has nucleated in the bottom of the etched area.

Figure 7

Fig. 7 SEM image showing CaF_2 irradiated with a 0.3 C/cm^2 electron dose through 2000-mesh nickel screen, followed by HCl etch for 2 min.

Figure 8

Fig. 8 CaF_2 irradiated with 157 nm laser on right side (2 hours), left side unexposed. Sample etched with 1M HCl for 24 minutes.

Figure 1

CaF_2 after electron irradiation, rinse and etch

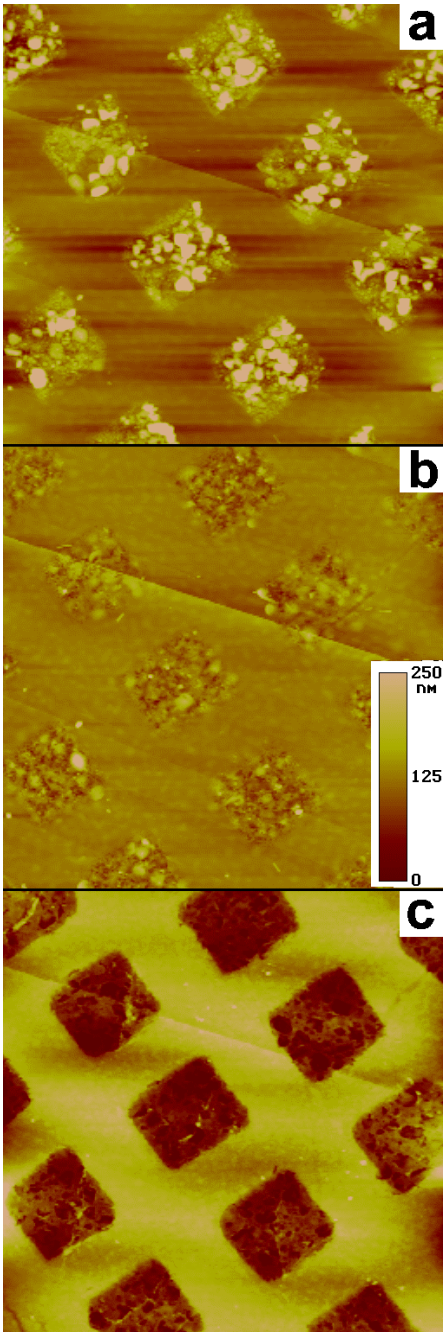

Figure 2

Raised volume due to electron exposure

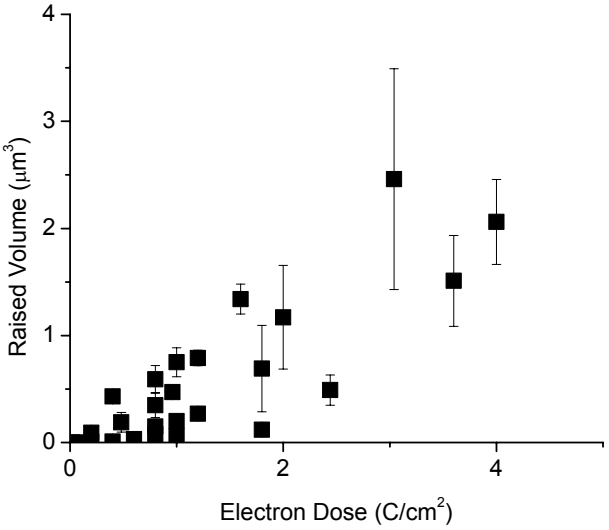

Figure 3

Etching with 1M HCl.

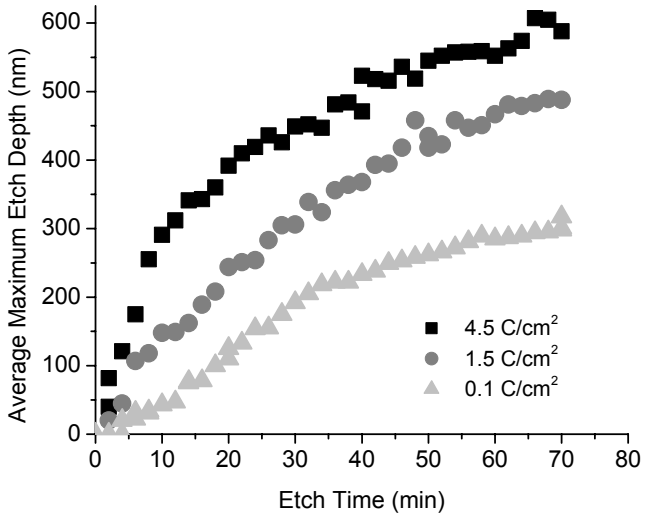

Figure 4

CaF_2 etched surface

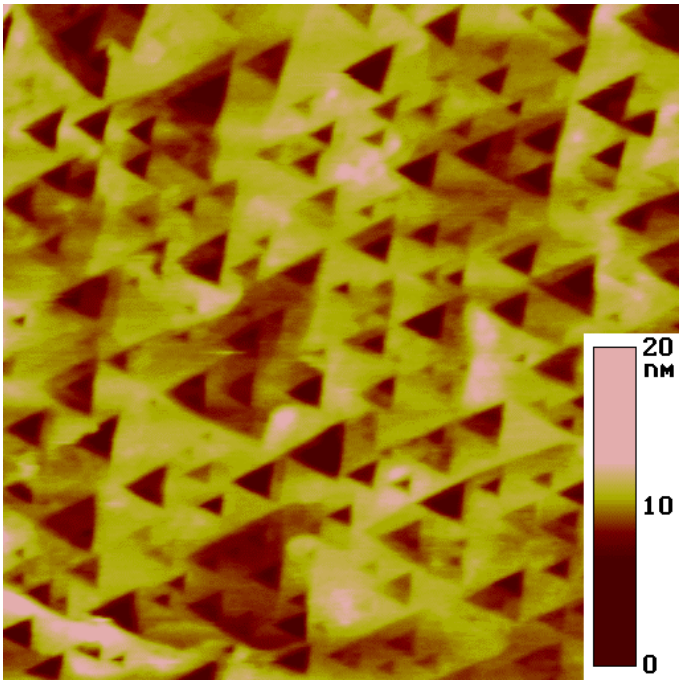

Figure 5

CaF_2 first generation pits

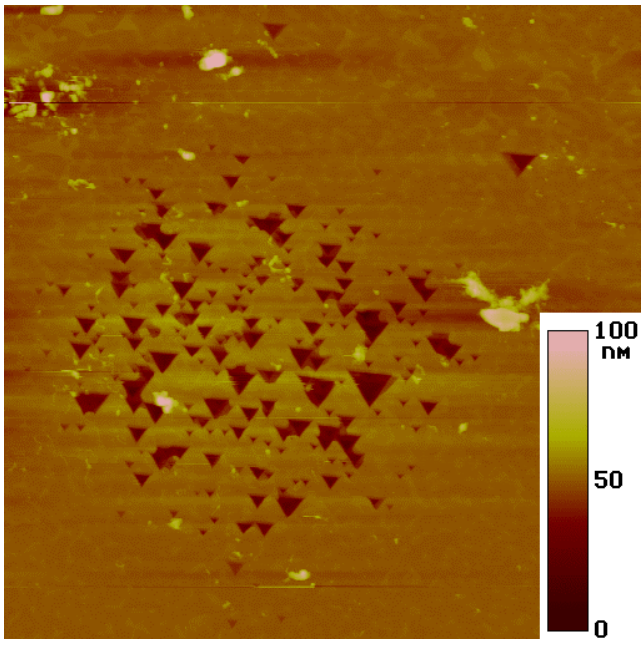

Figure 6

CaF_2 second generation pits

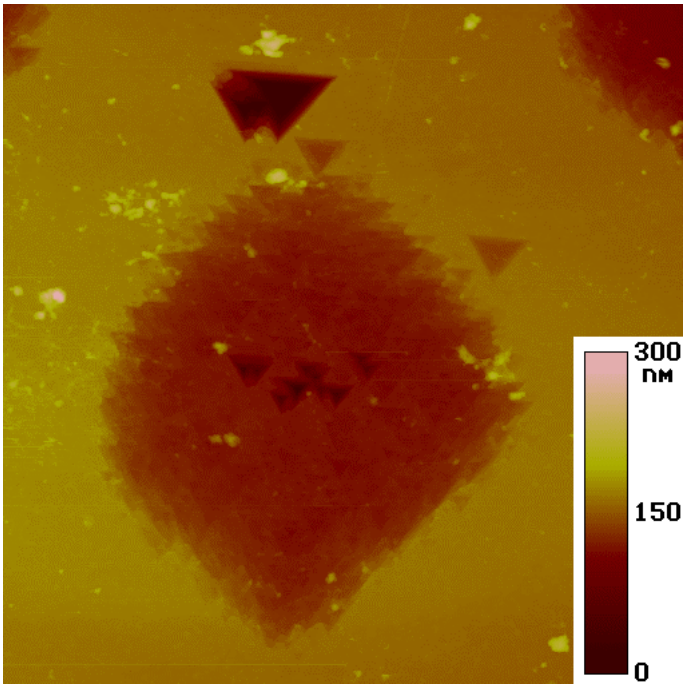

Figure 7

CaF_2 electron irradiated through nickel grid and etched in HCl

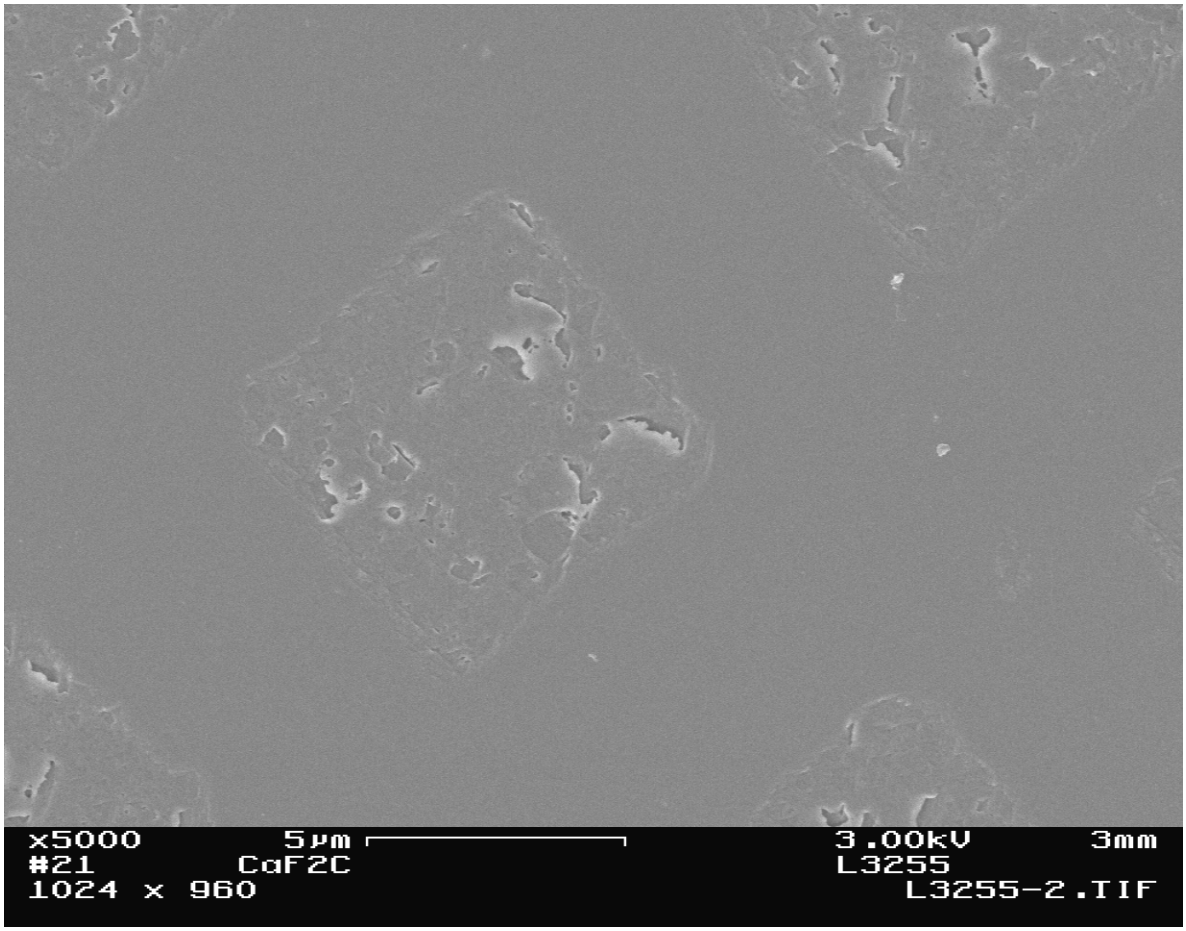

Figure 8

Etching at edge of 157 nm irradiated area

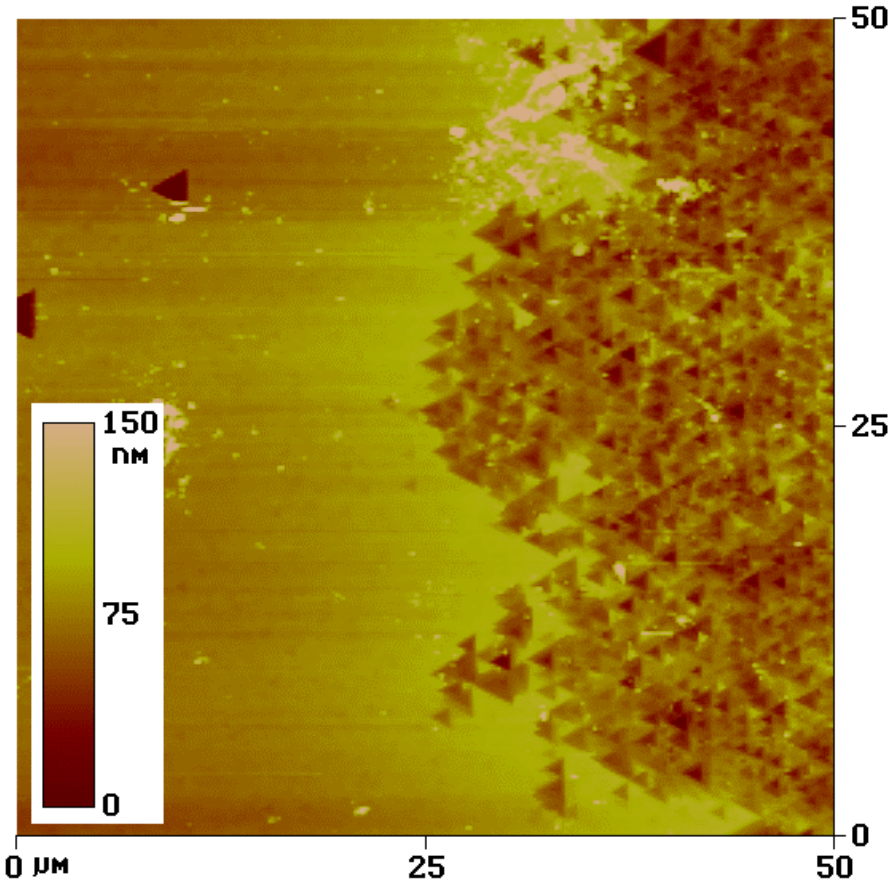

Attribution

Contributing authors:

Forrest Steven – All AFM images were done under his supervision

Ty Cumby – STE luminescence studies were done collaboratively

Brian Schubert – Worked with the Nd:YAG with supervision

Pasha Petite – Contributed to bleaching studies

John Leraas – Contributed to STE luminescence studies

Stephen Langford – Contributed valuable editing and thought process

J. Thomas Dickinson – Advisor

Colloid formation and laser-induced bleaching in fluorite

Joel B. LeBret[a], Loren P. Cramer[b], M. Grant Norton[a,b,*], and J. Thomas Dickinson[b,c]
Washington State University, Pullman WA 99164

Colloid formation and subsequent laser-induced bleaching in fluorite has been studied by transmission electron microscopy and electron diffraction. At high incident electron beam energies, Ca colloids with diameter ~10 nm form a simple cubic superlattice with lattice parameter a ~ 18 nm. The colloids themselves are topotactic with the fluorite matrix forming low energy interfaces close to a Σ=21 special grain boundary in cubic materials. Laser irradiation using λ = 532 nm has been shown to effectively bleach the e-beam irradiated samples returning the fluorite to its monocrystalline state. The bleached samples appear more resistant to further colloid formation.

[a] School of Mechanical and Materials Engineering
[b] Materials Science Program
[c] Department of Physics
[*] Corresponding author norton@mme.wsu.edu

Calcium fluoride (CaF_2) is an important optical material for use in the vacuum ultra-violet (UV). A major problem associated with this material, and other optical materials used at high laser intensities in the UV part of the electromagnetic spectrum, is defect formation. Defects, in the form of metal colloids, are produced in a number of materials by energetic radiation. In the case of single-crystal CaF_2 (fluorite), calcium colloids can be formed by exposure to even relatively low energy electrons (2 keV) at modest doses (<5 mC/cm^2).[1] Several groups have studied the *in situ* formation of colloids in fluorite using the transmission electron microscope (TEM).[2-5] In such studies electron energies in the range 100-200 keV are typical. At these energies colloid formation was found to be very rapid resulting, at least in samples thicker than 100nm, an ordered superlattice structure.

Recent studies have shown that colloids formed in CaF_2 by e-beam irradiation can be effectively bleached by subsequent laser irradiation at wavelengths ranging from the near IR to the deep UV.[6] The most effective bleaching is obtained at 532 nm and results in significant reduction in colloid absorption near 560 nm. Bleaching can be seen also by visible changes in the crystal as it goes from a purple coloration to nearly colorless.[6]

In this present study, the TEM has been used to examine colloid formation both *in situ* and *ex situ* and also to examine colloid formation in laser-bleached fluorite. Three specific observations are presented: the effect of low energy electron irradiation on electron-transparent fluorite samples; the effect of bleaching of low-energy e-beam irradiated samples by 532 nm laser radiation; the *in situ* development of a colloid superlattice in bleached fluorite and the topotactic relationship between colloid and matrix. Using electron diffraction patterns obtained during colloid evolution possible mechanisms for colloid formation and the bleaching process are presented.

Vacuum UV grade, single crystal CaF_2 was obtained from Korth Kristalle GmbH in the form of cylindrical rods, 1 cm in diameter. Slices, 2 mm thick, were cleaved from

the rods exposing {111} surfaces. Electron transparent samples for TEM examination were made by chemical thinning using HCl for ~1 h. The thinned samples were mounted on Cu grids before being placed in vacuum (<1x10^{-7} Pa) for electron irradiation at 2 keV with a dose of 400 mC/cm^2. Several of the e-beam irradiated TEM samples were bleached with ~100 pulses at 50 mJ/cm^2 of 532 nm radiation using the frequency doubled output of a Continuum Surelite II Nd:YAG laser (pulse duration 10 ns). All the samples were examined using a Philips CM200 TEM operated at 200 kV. Charging of the samples in the microscope was a problem and those samples not used for subsequent bleaching studies were coated with a thin layer of evaporated carbon.

Figure 1a shows a bright field (BF) image of a sample that had been e-beam irradiated prior to insertion into the TEM. The contrast is consistent with a dense array of fine damage. Electron diffraction patterns (DPs) recorded from this sample, insert in Fig. 1a, show a set of discrete reflections with spacing consistent with the fluorite lattice and a set of rings that can be indexed as arising from metallic calcium. From the DP it is clear that the calcium is randomly arranged in the monocrystalline fluorite matrix. A dark field (DF) image recorded using parts of the diffraction rings is shown in Fig. 1b. The calcium colloids can be seen to be roughly circular in cross section with a diameter between 5-10 nm and randomly distributed. Diffraction patterns recorded from some of the regions in these samples did show additional reflections that were consistent with CaO and also moiré fringes in BF images. CaO is formed by the surface oxidation of Ca that occurs in the interval between e-beam irradiation and subsequent examination in the TEM. Even at very low oxygen partial pressures Ca colloids have been shown to be very sensitive to oxidation.[7] It is unlikely that oxidation extends to colloids below the surface because of the evident reversibility of colloid formation as described below.

Figure 2 shows a sequence of three BF images obtained from a sample that had been irradiated initially outside the TEM using 2 keV electrons and then subsequently during examination in the microscope using 200 keV electrons. The development of an

ordered array of colloids is evident. The time between each image is approximately 5 s. In agreement with results reported by other groups the colloid superlattice is simple cubic with a lattice parameter of ~20 nm.[4] DPs recorded from fluorite crystals with a well-developed colloid superlattice show that in addition to a set of reflections arising from the matrix there is a second set that are due to Ca (insert in Fig. 2c). Despite the small mismatch in lattice parameters [a_{Ca} = 0.556 nm; a_{CaF2} = 0.545 nm] and the same Bravais lattice the orientation between the matrix and colloids is not the expected cube-on-cube; rather the topotatic relationship is $[1\bar{2}3]_f \parallel [0\bar{1}1]_c$ and $(\bar{1}11)_f \parallel (\bar{1}11)_c$, where the subscripts f and c refer to the fluorite and colloid, respectively. This orientation is close to the Σ = 21 special grain boundary in cubic crystals with rotation about <111>[8] and adopted, rather than cube-on-cube, to lower the overall phase boundary energy. Thus, there is both local orientation between each colloid and the fluorite matrix and orientation on a larger scale between the colloid array. The structure of the superlattice presumably being determined by energy requirements and diffusion distances for the fluoride ions during e-beam irradiation. During colloid formation it is not only the fluoride ions that diffuse but the calcium ions must also diffuse to the lower energy positions to achieve the observed orientation relationship.

Figure 3 shows a sequence of three DPs obtained from a laser-bleached TEM sample. From Fig. 3(a) it can be seen that the bleaching has completely returned the material to its monocrystalline state: the only reflections are from fluorite. This observation is consistent with a reduction in the colloid UV-VIS absorption peak as well as visible bleaching of the crystal seen in bulk fluorite.[6] Constant irradiation using 200 keV electrons for 15 minutes in the TEM leads to formation of additional reflections in the DP due to the formation of Ca colloids. At this stage all the colloids are topotactic with the fluorite. After constant irradiation for 110 minutes in the TEM (Fig. 3c) the reflections from the colloids are more intense and there is clear evidence of rings indicating that at least a significant number of the colloids are now randomly oriented in

the fluorite matrix.

Taken together these observations shed light on the process of colloid formation and bleaching. The colloids are clearly metallic calcium and form via reaction 1:

$$CaF_2 = Ca + F_2 \qquad (1)$$

The fluorine must be trapped in the fluorite lattice because the reaction is reversible upon laser irradiation. The formation of metallic calcium is accompanied by the formation of fluorine-rich point defects, which may include H- and I-centers. (The H-center is equivalent to an F_2^- ion occupying a fluorine lattice site, while the I-center is an F_2^- ion at an interstitial site.) Some fluorine may occupy interstitial sites as neutral atoms or molecules.[8] Although the exact nature of fluorine incorporation into fluorite is not at present known and all three possibilities are likely given the large size of the interstitial sites in fluorite it is clear that little fluorine is lost from the lattice and is available for recombination with metallic calcium upon bleaching. This agrees with the observation that very little fluorine containing emissions are observed leaving the sample during the 2 keV electron beam irradiation.

The colloids formed in samples irradiated using a low energy e-beam were neither topotactic nor ordered unlike those formed at high beam energies. Extended irradiation at high energies results in some randomization of the colloids within the fluorite but the superlattice structure remains. Upon bleaching there is in-diffusion of the fluorine (either in the form of ions or molecules) that shifts reaction 1 from right to left. Even though the matrix and colloids are not oriented cube-on-cube the colloids can easily realign to allow formation of the monocrystalline fluorite lattice—topotactic regrowth.

Of particular interest is the observation that colloid nucleation appears to be slowed in laser bleached samples. Even after almost 2 h of continued irradiation in the electron microscope DPs recorded bleached samples did not show very intense spots and well-defined polycrystalline rings were not found. Although the observation is based on limited evidence the effect is certainly worthy of further study. It is possible that laser

irradiation introduces defects during bleaching that limit fluorine diffusion. Point defects that do not produce visible coloration of the crystal are likely candidates. In a separate mass spectroscopy study we have found that during both laser and electron beam irradiation there is only a small amount of fluorine released from the sample (seen as a slow increase in the background F_2 i.e., the mass 38 signal); no direct emission from the surface of F or F_2 is observed. Thus, fluorine appears to have limited mobility in irradiated CaF_2.

This study has shown that laser conditioning can restore the monocrystallinity of CaF_2 optics. The degree of recovered transparency may not be suitable for lithographic applications where a very high uniformity is required. However, in less demanding applications, including UV windows in high radiation environments (e.g., inertial fusion systems), may benefit from treatments to remediate radiation-induced defects.

This work was supported the United States Department of Energy under Contract DE-FG03-98ER14864.

[1] R. Bennewitz, C. Günther, M. Reichling, E. Matthias, S. Vijayalakshmi, A. V. Barnes, and N. H. Tolk, Appl. Phys. Lett., **66**, 320 (1995)
[2] T. Evans, Phil. Mag. **8**, 1235 (1963)
[3] L.T. Chadderton, E. Johnson, and T. Wohlenberg, Physica Scripta **13**, 127 (1976)
[4] L.W. Hobbs, J. de Phys. **37**, C7-3 (1976)
[5] V.S. Teodorescu, L.C. Nistor, and J. Van Landuyt, Mater. Sci. Forum **239-241**, 671 (1997)
[6] L. P. Cramer, B. Schubert, P. Petite, S. C. Langford, and J. T. Dickinson, J. Appl. Phys. (submitted for publication)
[7] C.L. Strecker, W.E. Moddeeman, and J.T. Grant, J. Appl. Phys. **52**, 6921 (1981)
[8] H. Mykura in: Grain-Boundary Structure and Kinetics, papers presented at the ASM Materials Science Seminar, Milwaukee, Wisconsin, published by ASM, Metals Park, Ohio (1979) p. 445
[9] R. Bennewitz, M. Reichling, and E. Matthias, Surface Science, **387**, 69 (1997)

Figure Captions

Figure 1(a) BF image of *ex-situ* e-beam irradiated fluorite. The inset shows the DP obtained from this region of the sample (b). DF image obtained using part of the diffraction rings. The approximate position of the diffraction aperture is shown in the DP.

Figure 2. Sequence of BF images showing development of a colloid superlattice. The DP in (b) shows the topotactic arrangement of the two lattices.

Figure 3. Sequence of DPs showing the development of colloids in bleached fluorite. (a) Bleached sample; (b) After 15 minutes irradiation; (c) After 110 minutes irradiation.

Figure 1

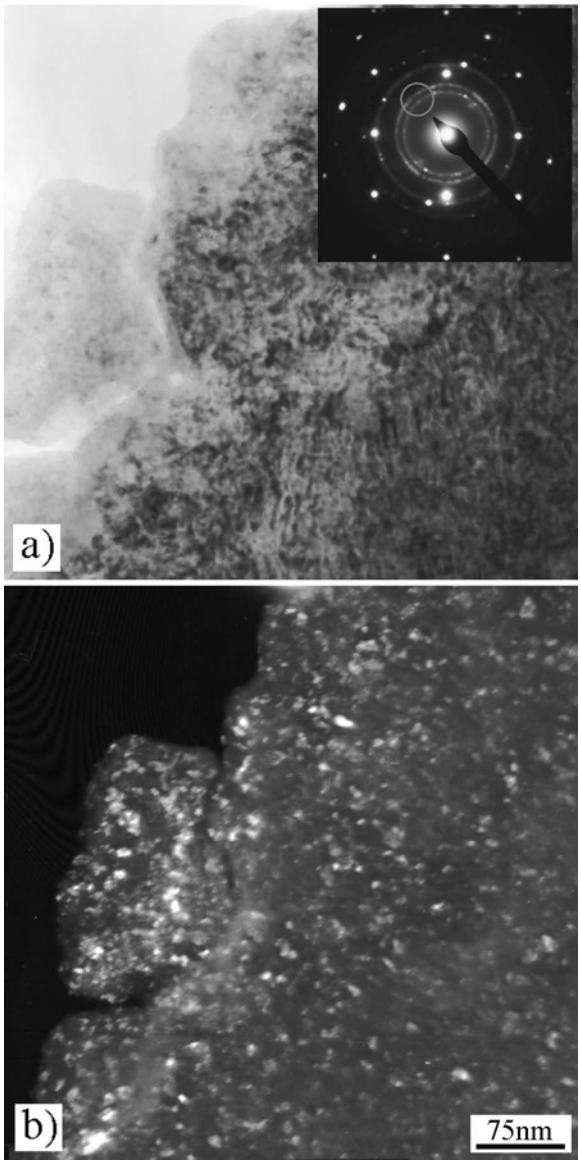

Figure 2

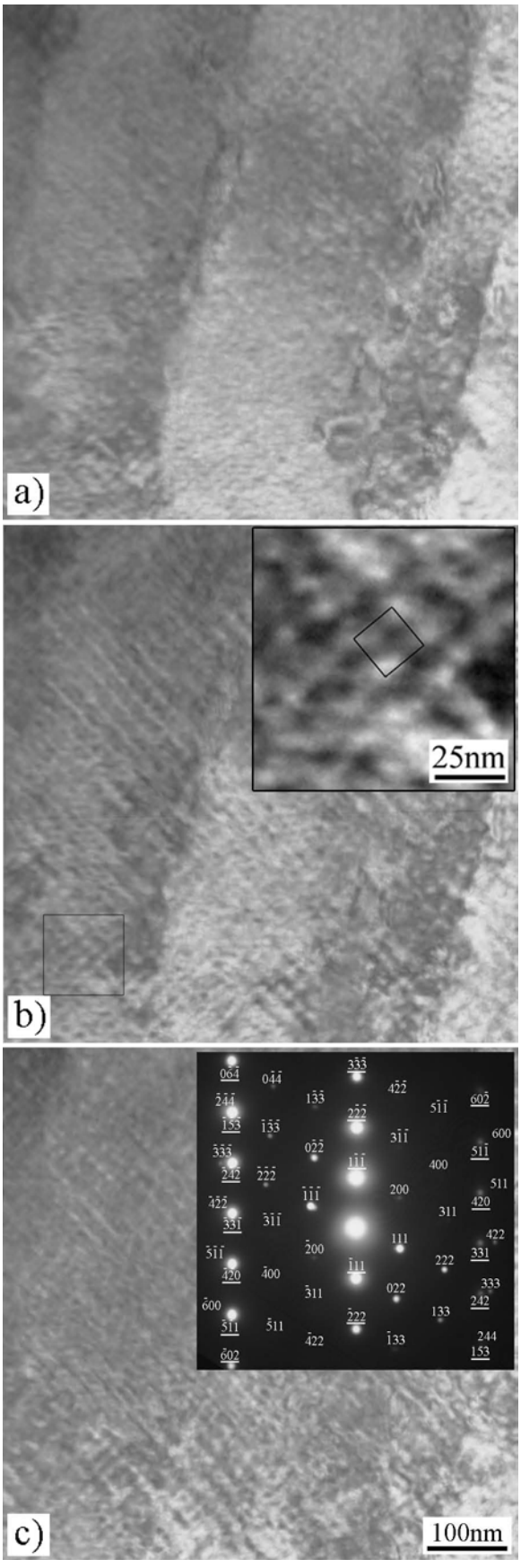

Figure 3

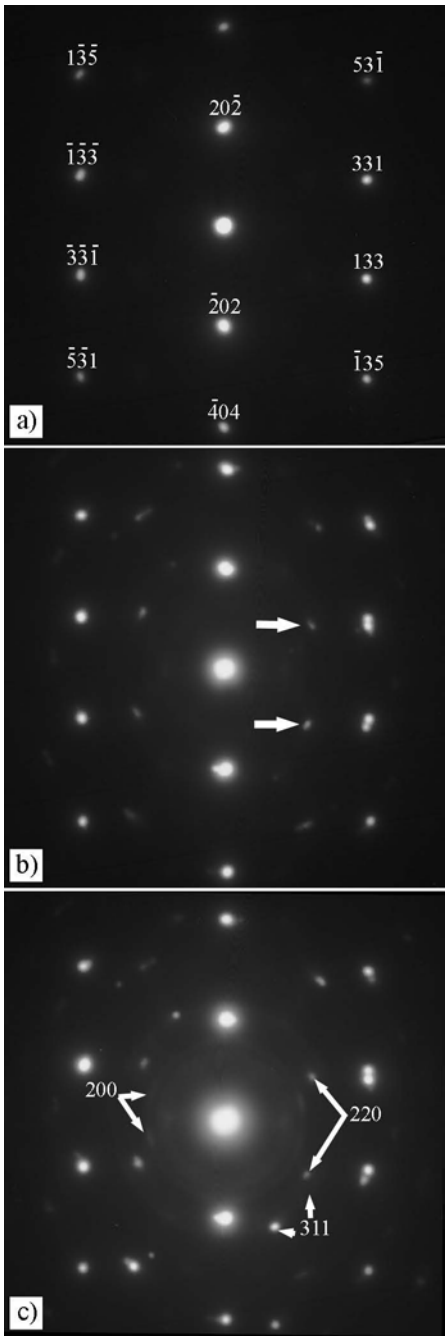
$1\bar{3}\bar{5}$
$53\bar{1}$
$20\bar{2}$
$\bar{1}\bar{3}\bar{3}$
331
$\bar{3}\bar{3}\bar{1}$
133
$\bar{2}02$
$\bar{5}\bar{3}1$
$\bar{1}35$
$\bar{4}04$
a)
b)
200
220
311
c)

ELSEVIER

Applied Surface Science 197–198 (2002) 100–106

applied surface science

www.elsevier.com/locate/apsusc

On the white light luminescence induced by irradiation of sodium nitrate single crystals by 1064 nm laser light

Bandis[1], L. Cramer, T.E. Holt, S.C. Langford, J.T. Dickinson[*]

Department of Physics, Washington State University, Pullman, WA 99164-2814, USA

Abstract

A number of wide bandgap inorganic materials can be prepared so that stimulation with nanosecond pulses of near infra-red (1064 nm—Nd:YAG fundamental) generates intense, transient white light. This light can span from 300 to 900 nm. Here, we characterize this emission from single crystal $NaNO_3$ and show that it is due to optical breakdown in the bulk. We contrast the behavior and character of time resolved spectra of this bulk breakdown with surface breakdown and provide evidence of defect mediated processes being responsible for the observed avalanche. We also conclude that confinement of the avalanche is essential for the production of this broad banded luminescence.

PACS: Laser materials, 42.70.H; Laser produced plasma, 52.50.J; Surface irradiation effects, 61.80.B; Defects Crystal, 61.72; Emission spectra-plasma, 52.25

Keywords: Luminescence; Sodium nitrate; Single crystals; Ionic crystal

1. Introduction

Transparent materials, such as ionic crystals, normally are expected to have weak interaction when exposed to relatively long wavelength laser light. However, defects can have a strong influence on laser materials interactions, particularly if occupied defect states couple to the radiation. In examining the interaction of nanosecond pulses of 1064 nm (Nd:YAG) radiation with the surfaces of materials such as $NaNO_3$, MgO, NaCl, and SiO_2 (all highly transparent at 1064 nm) we found that under relatively mild focusing into the bulk of the material led to intense white light emission. In this paper, we describe this emission and show that it is due to confined optical breakdown.

Here, we focus our attention on single crystal sodium nitrate ($NaNO_3$). $NaNO_3$ is a major component of high level nuclear wastes in underground storage tanks associated with US plutonium production during the cold war. Analyzing such wastes safely and accurately requires methods that do not involve direct contact, leading to techniques that utilize laser ablation and/or desorption, which are currently under development.

Sodium nitrate is a molecular-ionic crystal with a hexagonal unit cell and cleavage plane along the $10\bar{1}4$ direction, which intersects the c-axis at an angle of 43° 49′ [1,2]. The absorption spectra of $NaNO_3$ show broad bands due to $\pi^* \leftarrow \pi$ transitions which peak at ~6.4 eV, and at ~10.5 eV as well as ~12.1 eV due

[*] Corresponding author. Tel.: +1-509-335-4914; fax: 1-509-335-7816.
E-mail addresses: bandis@eim.org.gr (Bandis), jtd@wsu.edu (J.T. Dickinson).
[1] Present Address: Hellenic Institute of Metrology, Industrial Area of Thessaloniki, Block 45, Sindos, Thessaloniki 57022, Greece.

0169-4332/02/$ – see front matter
PII: S0169-4332(02)00311-2

to transfer of charge into the sodium cationic states [1]. A much weaker band at ~4.2 eV due to $\pi^* \leftarrow n$ also has been observed; although it has 1000 times weaker oscillator strength, it can be of importance in experiments with high power lasers.

Although $NaNO_3$ has intrinsic absorption bands neither at 248 nm nor at 1064 nm [1,2], it has been shown that exposing $NaNO_3$ surfaces to either 248 nm (5 eV) KrF excimer laser or 1064 nm (1.16 eV) Nd:YAG laser radiation results in the emission of neutral atoms and molecules, positive ions, and electrons [3–7]. The observation of intense, highly localized, laser-induced visible radiation from dielectrics is associated with the presence of hot plasma, and often is used as a criterion for the occurrence of optical breakdown and the initiation of irreversible damage. Efforts to improve the chemical analysis and characterization techniques that utilize laser ablation and/or desorption, as well as the search for and development of optical components with as high as possible damage thresholds requires detailed understanding of the mechanisms involved when materials are exposed to near-threshold laser radiation. While making several laser induced particle emission measurements on single crystal sodium nitrate ($NaNO_3$) we noticed at higher frequencies flashes of "white light" coming from inside the sample when irradiated with 1064 nm Nd:YAG laser light. Since this light spanned well above the photon energy of the laser light (1.16 eV) we were initially surprised to see it. Here, we explore the character of this broadband emission, compare its properties and behavior with light emitted from surface breakdown, and show that confinement of the breakdown is a major factor in generating this broadband emission.

2. Experiment

Our experiments were performed on cleaved melt grown $NaNO_3$ single crystals. The crystals were grown in our laboratory after heating to 315 °C in air 99.0% pure $NaNO_3$ powder (melting point: 306.8 °C) and then slowly, over a period of several days, cooling it back down to room temperature. A Continuum Sure-Light II Nd:YAG laser with a pulse width of ~8 ns (FWHM) at 1064 nm was used for sample irradiation. The spectra of the emitted radiation were obtained using a TVC Jarrell-Ash MonoSpec 18 spectrograph with a 150-g/mm grating, blazed at 450 nm and a Princeton Instruments intensified CCD (ITEA/CCD-576G/RBE). The intensity versus time of the visible part (300–800 nm) of the radiation was obtained using a 1 ns silicon photodiode behind a KG-5 Schott glass filter. A second photodiode behind a long pass RG-850 Schott glass filter (cutoff at 850 nm) was also used to monitor the time evolution of the laser intensity. The experiments were performed both in air and in a vacuum chamber with base pressure $< 1 \times 10^{-7}$ Pa.

The confinement of the surface was accomplished by bonding freshly cleaved $NaNO_3$ to a soda lime glass slide using epoxy adhesives. Two types of epoxy were used: UV curable and 5 min Epoxy. Epoxies, etc. manufactured the UV curable Type 60-7012 UV Curable Resin. These samples were exposed to a mercury vapor lamp for 6 h and left overnight. ITW Devon manufactured the 5 min epoxy; these samples were allowed to cure overnight in air. Both samples gave similar emissions from the confined interface.

3. Results and discussion

In Fig. 1(a) we show the image of the visible radiation emitted from the $NaNO_3$ due to 1064 nm laser radiation (1.9 J/cm^2). The image of the 2.5 mm laser spot obtained with the same magnification is also shown for comparison in Fig. 1(b). The emitted radiation appears to the naked eye as white light highly localized to sub-mm spots within the laser path, indicating that it originates from specific, defect rich sites. Similar experiments with much thicker crystals demonstrate that the emission sites can be at the surface as well as in the bulk of the crystal. The intensity of the visible radiation rapidly depletes with increasing number of pulses; it takes less than 10 laser pulses even at fluences well above the single pulse damage threshold for the visible radiation to completely disappear. The white light is accompanied by permanent material damage. Such damaged spots are easy to detect when high laser fluences are involved, but with difficulty when near-threshold fluences are used. Damage at emission sites along confined surfaces is readily visible in SEM images. The presence of high defect densities is not required for the confined surface experiments since we increased the fluence to insure surface damage at the interface.

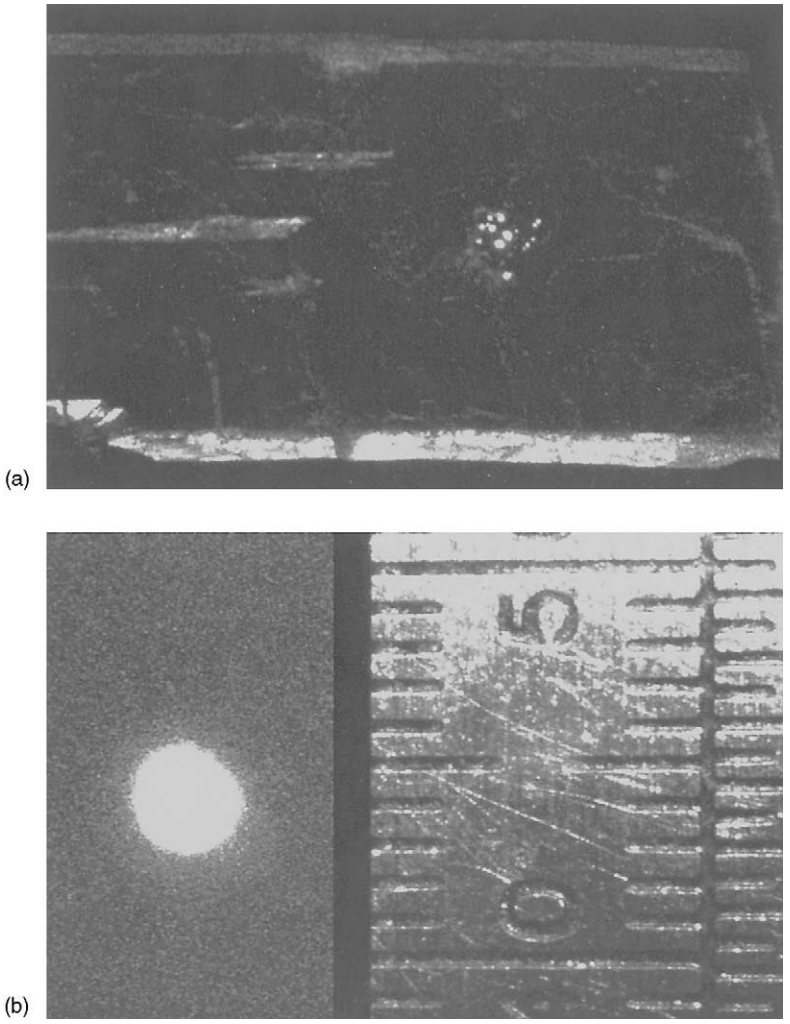

Fig. 1. Image of the highly localized visible radiation emitted from the $NaNO_3$ due to 1064 nm laser radiation (a). The image of the 2.5 mm laser spot obtained with the same magnification is also shown for comparison (b).

We are not always able to correlate visible flaws in the bulk to white light emission.

The spectrum of the emitted visible radiation from bulk emission sites is shown in Fig. 2 (laser fluence ~ 2 J/cm^2). Our experiments find that, when the emission site is in the bulk of the crystal, the observed spectra are broad without any sharp atomic lines. In Fig. 2, we also see that there is a short wavelength cutoff at about 320 nm. Comparison of the emission spectra with the transmittance spectrum demonstrates that the cutoff is due to $NaNO_3$ bulk absorption from the $\pi^* \leftarrow n$ absorption band at $\sim$4.2 eV [8].

Sharp atomic lines are present when the emission sites are near/at the surface and a plume is observed (Fig. 3) in vacuum. At short time delays (top curve), the broadband emission is also seen and the short wavelength cutoff of this emission indicates that the broad visible radiation still originates from sites near but below the surface. When the onset of spectra acquisition is delayed more than about 200 ns after the laser pulse, the broad visible band is not observed. Only the sharp atomic lines (Na D lines) remain. Thus, the broad visible band decays relatively fast, while the atomic lines can easily last several microseconds even in vacuum, the latter due to electron collisions with

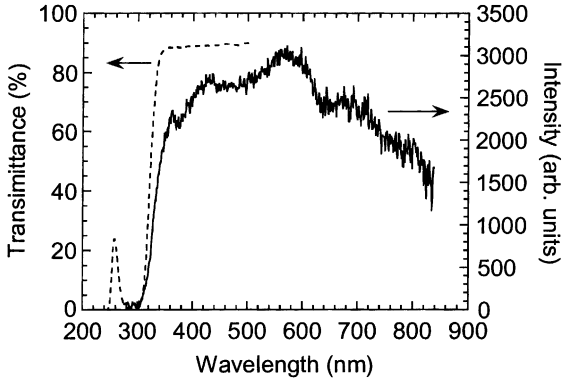

Fig. 2. Spectrum of the visible radiation emitted from a $NaNO_3$ bulk emission sites upon exposure to 1064 nm laser radiation with fluence near the single pulse damage threshold. The absence of emission at wavelengths lower than 350 nm is consistent with absorption from the crystal surrounding the emission sites. Also note the absence of any sharp peaks due to atomic emission.

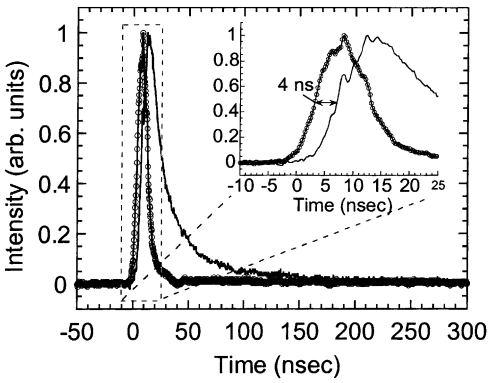

Fig. 4. Time evolution of the broad visible band from bulk emission sites (solid line). The emission intensity rises with a delay of a few nanoseconds with respect to the laser pulse (see inset) and typically decays in less than 200 ns. These data were acquired at a fluence of 10 J/cm^2 using a short focal length lens focused well below the sample surface.

neutrals creating excited atoms [9,10]. Furthermore, this bulk-like, confined breakdown appears to be the only source of continuum white light; i.e. the plume itself is *not* the source of the continuum (which may help interpret a number of previously reported LIBS spectra from irradiated insulators).

The intensity of the broad visible band from bulk emission sites as measured with a 1 ns silicon photodiode is plotted in Fig. 4 (solid line), and is compared with that of the laser pulse. The emission intensity rises with a delay of a few nanoseconds (∼4 ns) with respect to the laser pulse (see inset in Fig. 4) and typically decays in less than 200 ns due to rapid cooling of the confined plasma. Pulses with higher emission intensity exhibit typically shorter delays (≤2 ns) indicating that the observed delay depends on the absorbed energy, and therefore on the laser fluence as well as the defect density at the emission sites. At lower fluences we typically observe longer delays (∼5 ns), which demonstrate that the initial electron density necessary for the plasma formation, is *not* due to a multiphoton absorption mechanism. In contrast, the observed delays are better explained assuming that electrons are raised from defect energy levels to the conduction band via successive single-photon absorption events. In such a sequence, electrons from the deep laying defect energy levels are raised to higher empty ones and from there to the conduction band [7,9,10]. As soon as the necessary electron density is available, the laser radiation is more efficiently absorbed resulting in the avalanche production of the plasma that emits the observed visible radiation.

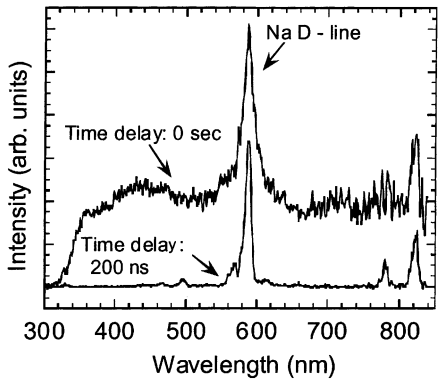

Fig. 3. Spectra of the visible radiation emitted from near surface emission sites of a $NaNO_3$ single crystal upon exposure to 1064 nm laser radiation in vacuum. In addition to the broadband visible radiation, emission from atomic lines (Na ID) is also observed indicating the presence of plume. The emission due to Na, consistent with plume formation and in contrast with the broad band, decays much slower, in a time scale, which in vacuum, can be of the order of several microseconds.

The spectra shown in Figs. 2, 3 and 5, is plasma radiation emitted from bulk emission sites and exhibits broad features without any sharp atomic emission lines. This is due to the relatively high pressures and temperatures present in confined plasmas [11],

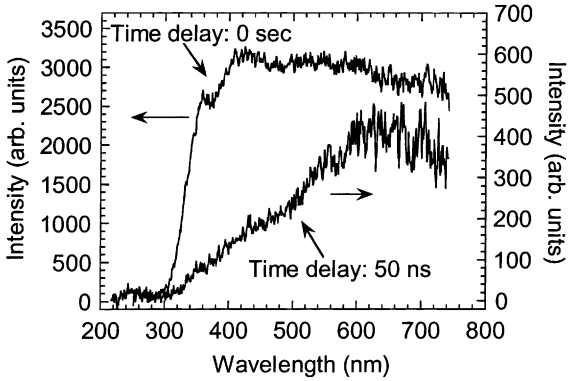

Fig. 5. Emission spectra from sites in the bulk of $NaNO_3$ for two different time delays with respect to laser pulse.

that result in strong broadening and/or complete quenching of the atomic line emission due to collisional de-excitation (non-radiative decay). Furthermore, in Fig. 5 we plot and compare the spectra obtained with zero and 50 ns delay with respect to laser pulse; again consistent with plasma emission, we observe that the high-energy side (low wavelength) of the spectra decays faster than the low energy side (''cooling'' of the plasma).

Optical breakdown in $NaNO_3$ resulting in plasma emission from sites in the bulk will occasionally exhibit an absorption band at wavelengths consistent with absorption from atomic sodium. This indicates the presence of cooler neutral sodium atoms surrounding the hot plasma core. In Fig. 6, we show the spectra of such emission for 0, 50, and 100 ns delays with respect to the laser pulse. Similar to the spectra shown in Fig. 5, we observe that with increasing delays the high-energy emission site of the spectrum strongly decays faster indicating fast cooling of the plasma.

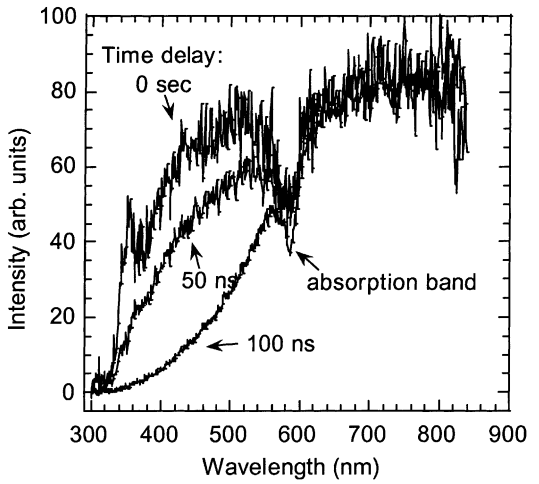

Fig. 6. Spectra from bulk emission sites that exhibit absorption due to neutral Na atoms. For comparison, we include the spectrum due to surface plume where a Na emission line is present (lower curve).

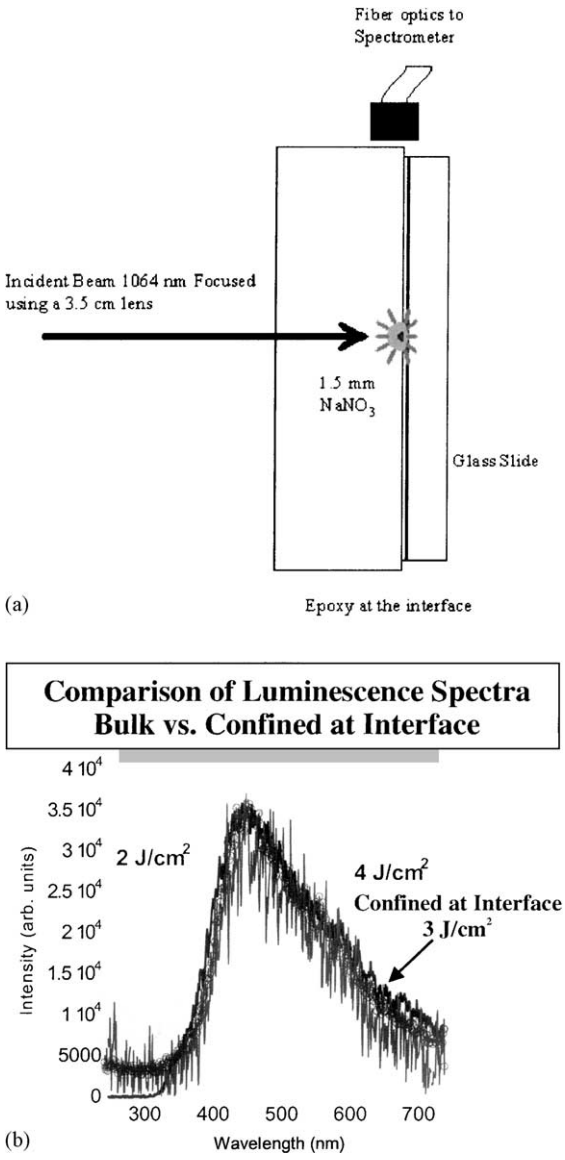

Fig. 7. (a) Arrangement for confining the free surface and observing the luminescence. (b) Comparison of uncorrected 'white light' spectra generated in the bulk of $NaNO_3$ (at 2 and 4 J/cm^2) with that generated at a confined interface (the $NaNO_3$ surface and an epoxy cover). All three spectra are indistinguishable.

If the confinement of the plasma is essential for generating the white light spectrum, then configuring artificial confinement at a surface of the single crystal $NaNO_3$ should generate white light. We found that simply clamping surfaces such as fused silica against the crystal did not provide sufficient confinement—Na rich plumes resulted when stimulated at 1064 nm. However, using a layer of a strong polymeric adhesive, such as an epoxy, generated the white light. Fig. 7(b) shows the uncorrected spectra of the broadband emission from the bulk (at two fluences) and the crystal-epoxy interface. As can be seen, there is no difference in the spectra. We attribute these similarities to the relatively high pressures and temperatures present in the confined case [11], which result in extremely strong broadening and/or complete quenching of the atomic line emission due to collisional de-excitation (non-radiative decay). It should be noted that at higher fluence, Na D line on top of the white light could be generated at such an interface.

By carefully cleaving off the epoxy from the crystal, the irradiated regions of the interface can be examined. The SEM micrographs of such a confined surface are shown in Fig. 8(a) and (b) showing the damage caused by focusing the 1064 nm pulse at the crystal-epoxy interface. These damage sites were accompanied with white light only (no Na D line discernible). They show that the kernal or nucleus of the damage was at the surface of the crystal of $NaNO_3$. By simply providing the confinement of the adhesive, the formation of line spectra was totally inhibited.

(a)

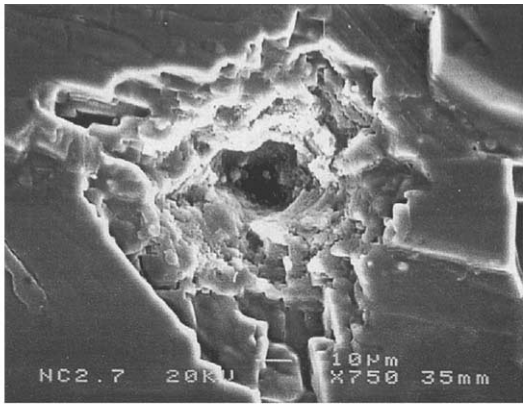

(b)

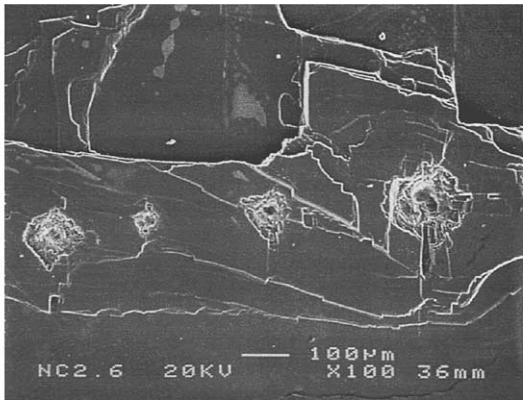

Fig. 8. (a) Single pulsed damage at confined interface as imaged with SEM. (b) SEM micrographs of single pulse damage of the confined interface at fluences below the threshold for the formation of Na D line emission.

4. Conclusion

Exposure of single crystal $NaNO_3$ to nanosecond pulses of 1064 nm radiation can lead to a broad band continuum that we have shown is due to highly localized, bulk, confined breakdown. The observed short wavelength cutoff in the emission spectra is due to bulk absorption of the material surrounding the emission sites. Study of the time evolution of the emitted radiation from bulk emission sites shows that, compared to plume radiation (emission from surface sites) that can last for microseconds, the broad visible band decays relatively fast in less than 200 ns due to rapid cooling of the confined plasma. The rise time of such radiation can exhibit delays up to several nanoseconds relative to the laser pulse, which demonstrates that the initial electron density, necessary for the plasma formation, is not due to multiphoton absorption. The observed delays can be understood assuming that initial excitation occurs via successive single-photon absorption events within clusters of defects which raise the electrons from deep laying defect energy levels to higher ones and from there to the conduction band [6,7]. Artificially confined substrates (using epoxy) generated the same spectra when breakdown occurred at the interface. Finally, surface breakdown was shown to yield continuum white light due to breakdown within the near surface bulk plus the usual atomic lines from the expanding plume due to electron collisions to create excited atoms.

Acknowledgements

This work was supported by the Department of Energy under Contract DE-FG03-99ER14864 and an Equipment Grant from the National Science Foundation, DMR-9503304.

References

[1] H. Yamashita, R. Kato, J. Phys. Soc. Jpn. 29 (1970) 1557.
[2] H. Yamashita, J. Phys. Soc. Jpn. 33 (1972) 1407.
[3] R.L. Webb, S.C. Langford, J.T. Dickinson, Nucl. Instrum. Meth. Phys. Res. B 103 (1995) 297.
[4] J.J. Shin, M.-W. Kim, J.T. Dickinson, J. Appl. Phys. 80 (1996) 7065.
[5] D.R. Ermer, J.-J. Shin, S.C. Langford, K.W. Hipps, J.T. Dickinson, J. Appl. Phys. 80 (1996) 6452.
[6] C. Bandis, S.C. Langford, J.T. Dickinson, Appl. Phys. Lett. 76 (2000) 421.
[7] C. Bandis, S.C. Langford, J.T. Dickinson, D.R. Ermer, N. Itoh, J. Appl. Phys. 87 (2000) 1522.
[8] M. Kamada, R. Kato, J. Phys. Soc. Jpn. 35 (1973) 1561.
[9] D.R. Ermer, S.C. Langford, J.T. Dickinson, J. Appl. Phys. 81 (1997) 1495.
[10] J.J. Shin, D.R. Ermer, S.C. Langford, J.T. Dickinson, Appl. Phys. A 64 (1997) 7.
[11] D. Devaux, R. Fabbro, L. Tollier, E. Bartnicki, J. Appl. Phys. 74 (1993) 2268.

ELSEVIER

Applied Surface Science 197–198 (2002) 35–40

applied surface science

www.elsevier.com/locate/apsusc

Wavelength dependence of UV-laser induced emission of neutral and ionic species from single crystal $NaNO_3$

L.P. Cramer[a,*], S.C. Langford[a], W.P. Hess[b], J.T. Dickinson[a]

[a]*Department of Physics and Materials Science, Washington State University, Pullman, WA 99164-2814, USA*
[b]*Pacific Northwest National Laboratory, P.O. Box 999, Richland, WA 99352, USA*

Abstract

We report time-resolved, quadrupole mass-selected measurements of neutral and ion emission from single crystal sodium nitrate exposed to ns pulse excimer laser radiation at 157 nm (F_2 excimer, 7.9 eV photons), 193 nm (ArF excimer, 6.4 eV photons) and 248 nm (KrF excimer, 5.0 eV photons). Neutral emissions, including NO, O_2, N_2, and Na are observed at all three wavelengths. At 193 nm, intense atomic N and O emissions are also observed, possibly due to a $1 + 1$ excitation involving the $\pi^* \leftarrow \pi$ transition in the nitrate ion (centered at 6 eV) followed by excitation to a higher excited state. This transition is not efficiently excited at the other two wavelengths. At 248 nm, much of the emission is attributed to thermally assisted, dissociative electron/hole attachment. Although 157 nm photons do not excite the $\pi^* \leftarrow \pi$ transition efficiently, the resulting NO emission is found to be quite intense: on a per unit energy (or per photon) basis, 157 nm photons are much more efficient in decomposing nitrate anions than 193 nm photons. Intense ion emission (principally Na^+ and NO^+) is observed at 193 and 157 nm, with weaker Na^+ emission at 248 nm. The ion intensities show high-order fluence dependence, consistent with photoelectronic emission involving sequential photon absorption as described earlier for 248 nm irradiation [J. Appl. Phys. (80) (1996) 6452].

Keywords: Sodium nitrate; Laser desorption; Ion emission; Photolysis

1. Introduction

Laser-induced particle emission from solid surfaces depends strongly on the laser wavelength and the details of bulk and defect absorption. Laser interactions in transparent, ionic solids are often much stronger in the ultraviolet, even at wavelengths well below the bandgap, usually due to absorption at defects. When the photon energy lies within a strong absorption band, emission mechanisms should be markedly altered. The question of how interaction strengths and emission mechanisms change as the laser wavelength is probed across a strong absorption band is largely unexplored in solid materials.

Although the bandgap of sodium nitrate exceeds 10 eV, it displays a strong absorption centered at 6 eV due to a $\pi^* \leftarrow \pi$ transition in the NO_3^- anion. Irradiation at 213 and 193 nm (5.8 and 6.4 eV photons) at low laser fluences (energy per unit area) produce significant NO and atomic O emissions with thermal and hyperthermal components [2–5]. The neutral yields depend linearly on fluence, consistent with photoelectronic emission due to single photon absorption. In contrast, irradiation at 248 nm (5.0 eV photons—on the low energy edge of the $\pi^* \leftarrow \pi$ band) at higher fluences produces principally defect-related NO emission and negligible O emission; NO emission again

* Corresponding author. Tel.: +1-509-335-1698.
E-mail address: lpcramer@wsu.edu (L.P. Cramer).

0169-4332/02/$ – see front matter
PII: S0169-4332(02)00299-4

depends linearly on fluence at fluences below 100 mJ/cm^2, also consistent with a photoelectronic emission mechanism [1,6–8]. The velocity distribution of the neutral fragments displays both fast and slow emission components. This emission is well accounted for on the basis of dissociative charge attachment at surface anion groups [1,6–10], where mobile electrons and/or holes are released from defect sites by single photon processes [1]. This is strongly supported by the observation that at 248 nm induction (incubation) is seen in the increasing NO emission intensity with number of laser pulses from $NaNO_3$ due to defect production [6] and the dramatic increase in NO (and O_2) emission intensity with exposure of the surface to electron beams (also generating defects).

Here, we explore emissions at 157 nm (F_2 excimer, 7.9 eV photons), at photon energies well above the peak of the $\pi^* \leftarrow \pi$ band, where the absorption cross-section is over an order of magnitude smaller than at 248 and 193 nm [11,12]. We find that neutral and ion emissions at 157 nm are quite intense despite the weak absorption (relative to 193 nm). The rate of anion decomposition at 157 nm is at least double the rate at 193 nm on per unit energy basis over the entire range of fluences employed. Nevertheless, intense atomic N and O emissions are observed at 193 nm that are absent at 157 nm, indicating that the emission (and probably absorption) mechanism changes as the wavelength is decreased from 193 to 157 nm.

2. Experiment

$NaNO_3$ single crystals were grown in our laboratory by slowly cooling $NaNO_3$ (99.0% pure, Alfa Aesar) from the melt. The resulting crystals were cleaved into 0.2 cm × 1 cm × 1 cm plates and mounted in vacuum on a 3D translation stage mounted directly in front of and normal to the axis of a UTI 100C quadrupole mass filter.

All experiments were performed in a vacuum chamber with base pressure $< 1 \times 10^{-9}$ Torr. Sample irradiation at 157 nm was performed with a Lambda Physik LPF 200 excimer laser (F_2) with a pulse width of 20 ns; the region between the laser and the vacuum system was flushed with dry N_2 to minimize transmission losses due to atmospheric water and O_2. Irradiation at 248 and 193 nm was performed with a Lambda Physik LPX 205I excimer laser (KrF, ArF), with a pulse width of about 30 ns.

3. Results and discussion

3.1. Neutral time-of-flight signals

Depending on wavelength, the neutral products observed are NO, O_2 (not shown), Na (not shown), atomic N, and atomic O. Typical NO time-of-flight signals for each wavelength at a fluence of 85 mJ/cm^2 appear in Fig. 1. At this fluence, 157 nm irradiation yields by far the most intense NO signal, followed by 248 nm (17% of 157 nm) and 193 nm (6% of 157 nm).

The NO time-of-flight at 193 nm is noticeably faster than at the NO time-of-flight at the other wavelengths. A two-component thermal emission model provides a reasonable fit to the signal, with one component having a temperature near 1500 K and the other near room temperature. Knutsen and Orlando [4] interpreted a similar high temperature component under 193 nm excimer laser irradiation ($\leq$1 mJ/cm^2) in terms of direct photoelectronic emission from the surface. In contrast, Bradley et al. found no high temperature component in similar measurements on a single rotational/vibrational state under 213 nm irradiation (5.8 eV photons, 5 ns pulses, <1 mJ/cm^2). A study of

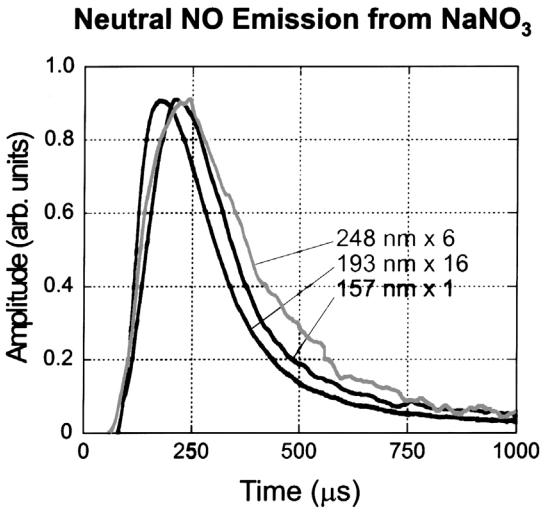

Fig. 1. NO time-of-flight signals at 248, 193, and 157 nm at fluences of approximately 85 mJ/cm^2.

electron-stimulated desorption (ESD) of NO from $NaNO_3$ by Petrik et al. [13] indicate that the intensity and effective translational temperature depend strongly on rotational state, with some rotational states showing no hyperthermal component. In our work, the NO signals at 193 nm are consistent with NO production by single photon, photoelectronic decomposition of the anion; some molecules are emitted in a concerted fashion, yielding NO with a hyperthermal velocity distribution, while other molecules are desorbed after reaching thermal equilibrium with the surface.

The NO signals at 157 and 248 nm are slower. Nevertheless, the emission at 157 nm is still consistent with a two component model, with one fast component (equivalent temperature near 1500 K) and a slower component (temperature somewhat above room temperature). The fast component at 157 nm makes up a much smaller fraction of the total emission than the fast component at 193 nm.

The TOF signal at 248 nm is more complex, with a long tail on the low energy side of the peak. In previous work, we have shown that NO and O_2 emission at 248 nm persists for some hundreds of microseconds after the laser pulse. Delayed emission is also observed during pulsed electron irradiation [13,14]. As previously mentioned, emission of neutral anion fragments at 248 nm has been attributed to dissociative charge attachment (hole or electron attachment) [10,15]. Charge liberated during the laser pulse can remain mobile for some time after the laser pulse, resulting in dissociation events long after the laser pulse. This charge originates from defect states, which accounts for the linear fluence dependence (noted below) despite the low photon energy. The long emission tail at 248 nm appears to be unique among the three laser wavelengths employed in this work. Thus, delayed emission due to charge attachment appears to be far more important at 248 nm than at 193 or 157 nm. One possibility we are considering is that at the higher photon energies, electrons are more readily emitted into vacuum where they do not participate in anion decomposition. We plan to experimentally check the relative electron yields from $NaNO_3$ at these three wavelengths.

3.2. Neutral emission fluence dependence

The fluence dependence of the neutral NO, N, and O intensities at all three wavelengths appear in Fig. 2.

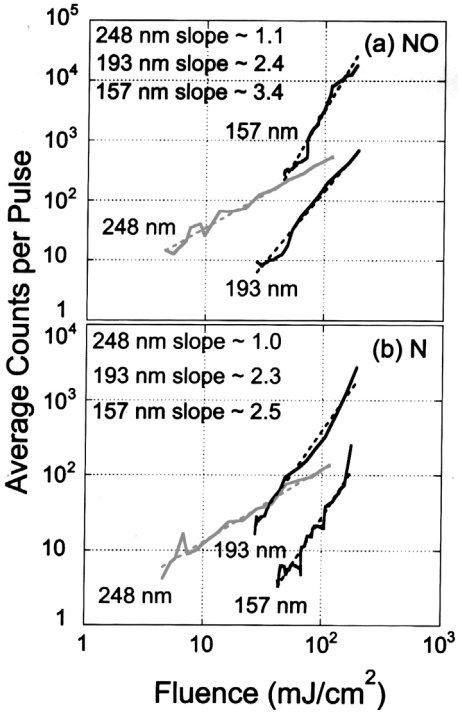

Fig. 2. Fluence dependence of (a) neutral NO and (b) neutral atomic N at 248, 193 and 157 nm.

Consistent with previous work [6], the NO intensity at 248 nm is an approximately linear function of fluence over this fluence range. In contrast, the fluence dependence of NO at 193 and 157 nm (6.4 and 7.9 eV) is non-linear (second to fourth order, at much lower fluences (<1 mJ/cm^2), Knutsen and Orlando [5] found a linear fluence dependence at 193 nm). The non-linear fluence dependence observed at the fluences employed here is not likely the result of non-resonant multiphoton absorption. More feasible is a *multiple* photon process involving sequential single photon absorption, similar to the mechanisms we have suggested for positive ion emission [16]. These multiple photon processes are normally dependent on the presence of defects. Defect driven processes are typically associated with the phenomenon of induction or incubation, where the intensity of a product measured at constant fluence increases under prolonged irradiation. We have observed such induction in the neutral NO signal from $NaNO_3$ at 248 nm, but have not yet performed the necessary experiments at 193 nm and 157 nm. The participating defects could be lattice

defects, such as vacancies, or electronic defects, such as excitons. For instance, exciton–exciton interactions can yield especially high energy (and thus possibly dissociative) excitations. Similarly, dissociative 1 + 1 excitations involving long-lived intermediate states would depend non-linearly on fluence.

Fig. 2(b) shows the fluence dependence of the signal due to atomic N at the three wavelengths employed in this study. At 248 and 157 nm, this signal is quite weak and can be entirely attributed to fragmentation of NO and N_2 in the quadrupole ionizer; thus, at our level of sensitivity, we detect no atomic N from the sample at 248 and 157 nm. In contrast, the N signal at 193 nm is many times greater than the detected NO and N_2 signals, and thus accounts for the great majority of the total nitrogen (in all forms) emitted from the sample. Similarly strong atomic O signals (not shown) are also observed. At 193 nm, anion radiolysis is far more complete, yielding more atomic species, than radiolysis at 248 and 157 nm. We propose that this atomic emission is due to a 1 + 1 excitation through the π^* state that produces an extremely unstable anion. The absence of significant atomic N emission at 157 nm is consistent with the expected absence of the $\pi^* \leftarrow \pi$ resonance at this wavelength.

We currently have no reasonable explanation for the higher yield of NO at 157 nm. The lack of likely resonance states suggests that the roughly third order fluence dependence observed for NO emission at 157 nm is not due to multi- or multiple photon absorption. We are exploring the role of defects in this emission as a possible explanation. We note that at the high end of the fluence range employed, 157 nm photons dissociate more than twice as many anions per unit incident energy (and nearly three times on a 'per photon' basis) than 193 nm photons. Given that laser absorption at 193 nm is at least an order of magnitude greater than at 157 nm, this is surprising and begs for an explanation.

3.3. Ion time-of-flight

Na^+ and NO^+ are observed at all three wavelengths, although significantly higher fluences are required to produce measurable NO^+ at 248 nm. Typical TOF signals for Na^+ and NO^+ are shown in Fig. 3 for all three wavelengths. At low fluences (<95 mJ/cm^2 at 193 and 248 nm and <70 mJ/cm^2 at 157 nm), the Na^+ signals are adequately described by a single component, Gaussian energy distribution. The kinetic energy of this emission varies with wavelength and increases as the fluence is raised. At higher fluences, the Na^+ signal at each wavelength develops an additional peak at lower kinetic energies, which is well described by an additional Gaussian energy distribution. This slower peak displays kinetic energy distributions consistently in the 2–4 eV range. In previous work, we have observed both high and low energy Na^+ under 248 nm irradiation at fluences above 150 mJ/cm^2 [17]. Electrostatic arguments indicate that the photoionization of singly charged surface defects (e.g. surface vacancies with one trapped electron) would repel Na^+ adsorbed atop these sites with enough force to give them 2–4 eV of kinetic energy. The high energy ions (kinetic energies 7–10 eV) are attributed to emission from atop doubly charged defects, such as might be expected on modified surfaces with oxide-related surface defects [1,18,19].

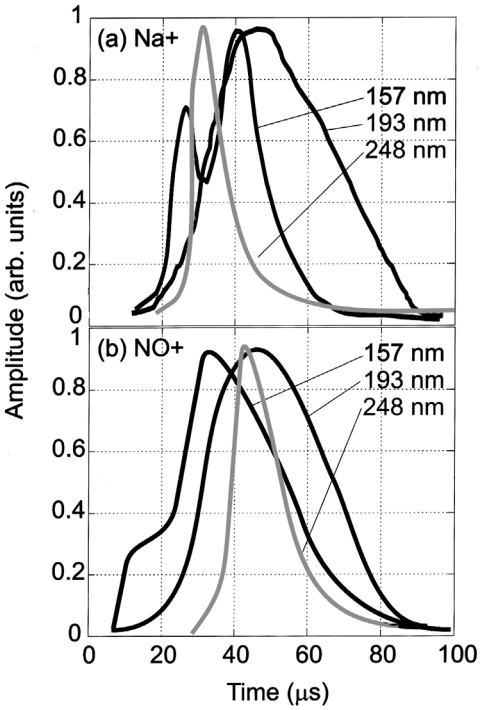

Fig. 3. Na^+ and NO^+ time-of-flight signals at 248, 193 and 157 nm, at fluences near 90 mJ/cm^2.

In contrast, the NO^+ TOF signals cannot generally be described in terms of one or two well-behaved,

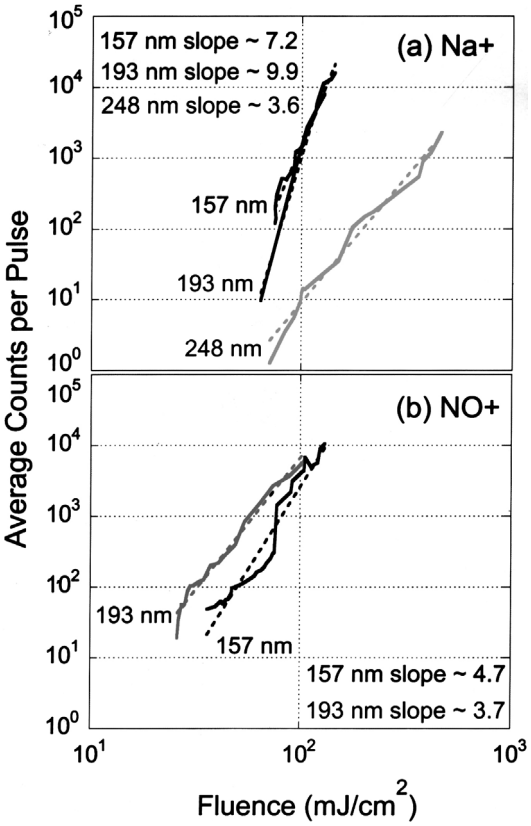

Fig. 4. Fluence dependence of: (a) Na^+ and (b) NO^+ emissions at 248, 193 and 157 nm.

Gaussian energy distributions. Both the TOF and energy distributions are quite broad and presumably represent emission from a wide variety of defect sites.

3.4. Ion fluence dependence

The Na^+ and NO^+ fluence dependence at 248, 193 and 157 nm are compared in Fig. 4. Na^+ emission in particular is strongly non-linear at 193 and 157 nm wavelengths (seventh to tenth order). It is highly unlikely that the photoionization of defect states would involve so many photons, even in a sequence of single-photon steps. As noted above, thermally activated processes can often mimic power-law multiple photon processes. The combination of ionization at several defects plus thermal activation would lead to this apparent high-order fluence dependence.

NO^+ emission at 193 nm is typically two orders of magnitude more intense than at 157 nm, suggesting that resonance absorption in the anion plays an important role in the emission process. This is true despite the fact that neutral NO emission is much more intense at 157 nm. In the absence of resonant ionization of gas phase neutral NO at both 193 and 157 nm (requires 9.24 eV), emission at one of these wavelengths (and probably both) must involve adsorbed NO^+ defects formed during anion decomposition or by hole trapping. Due to their initial association with the anion sublattice, these defects may experience a wide range of electrostatic environments, which would account for the wide range of observed kinetic energies.

4. Conclusions

Significant ion and neutral emissions are observed at each of the three excimer wavelengths employed in this study (248, 193, and 157 nm). Among the neutral species, NO and O_2 are emitted at all three wavelengths, while 193 nm radiation also yields intense atomic N and O emissions. We attribute the atomic N and O emissions to especially energetic dissociation events resulting from resonant (possibly sequential) two-photon excitation involving the $\pi^* \leftarrow \pi$ absorption centered at 6 eV. In contrast, N and O emissions at 157 nm are not detected, presumably due to the weakness of the $\pi^* \leftarrow \pi$ absorption at this wavelength. Despite this weak absorption into the π^* state, 157 nm photons decompose roughly twice as many NO_3^- anions per unit energy as 193 nm photons at the fluences employed in this work. This is a puzzling result that demands more study.

Significant Na^+ and NO^+ emissions are observed at 193 and 157 nm, with less intense emissions at 248 nm. The well-defined Na^+ kinetic energies argue for emission from equally well-defined defect states; the low kinetic energies are consistent with emission from sites atop singly charged anion vacancy defects. Most importantly, sample absorption at the laser wavelength does not completely control the strength of the laser interaction. An understanding of these effects will allow us to intelligently exploit the range of photon energies that are currently available in using lasers for processing,

surface modification, and chemical analysis of wide bandgap materials.

Acknowledgements

This work was supported by the United States Department of Energy under Contract DE-FG03-98ER14864.

References

[1] D.R. Ermer, J.-J. Shin, S.C. Langford, K.W. Hipps, J.T. Dickinson, J. Appl. Phys. 80 (1996) 6452.
[2] R.A. Bradley, E. Lanzendorf, M.I. McCarthy, T.M. Orlando, W.P. Hess, J. Phys. Chem. 99 (1995) 11715.
[3] W.P. Hess, K.A.H. German, R.A. Bradley, M.I. McCarthy, Appl. Surf. Sci. 96-98 (1996) 321.
[4] K. Knutsen, T.M. Orlando, Phys. Rev. B 55 (1997) 13246.
[5] K. Knutsen, T.M. Orlando, Appl. Surf. Sci. 127-129 (1998) 1.
[6] R.L. Webb, S.C. Langford, J.T. Dickinson, Nucl. Instrum. Meth. Phys. Res. B 103 (1995) 297.
[7] J.T. Dickinson, J.-J. Shin, S.C. Langford, Appl. Surf. Sci. 96-98 (1996) 326.
[8] J.-J. Shin, M.-W. Kim, J.T. Dickinson, J. Appl. Phys. 80 (1996) 7065.
[9] J. Cunningham, J. Phys. Chem. 65 (1961) 628.
[10] J. Cunningham, in: E.T. Kaiser, L. Kevan (Eds.), Radical Ions, Interscience, New York, 1968, p. 475.
[11] H. Yamashita, R. Kato, J. Phys. Soc. Jpn. 29 (1970) 1557.
[12] H. Yamashita, J. Phys. Soc. Jpn. 33 (1972) 1407.
[13] N.G. Petrik, K. Knutsen, T.M. Orlando, J. Phys. Chem. B 104 (2000) 1563.
[14] J.-J. Shin, S.C. Langford, J.T. Dickinson, Y. Wu, Nucl. Instrum. Meth. Phys. Res. B 103 (1995) 284.
[15] J. Cunningham, J. Phys. Chem. 70 (1966) 30.
[16] J.T. Dickinson, in: J.C. Miller, R.F. Haglund (Eds.), Experimental Methods in Physical Sciences, Vol. 30, Academic Press, New York, 1998, p. 139.
[17] J.-J. Shin, D.R. Ermer, S.C. Langford, J.T. Dickinson, Appl. Phys. A 64 (1997) 7.
[18] J.T. Dickinson, S.C. Langford, J.J. Shin, D.L. Doering, Phys. Rev. Lett. 73 (1994) 2630.
[19] J.T. Dickinson, J.J. Shin, S.C. Langford, Appl. Surf. Sci. 96–98 (1996) 316.